CLIMATE DYNAMICS OF THE SOUTH PACIFIC CONVERGENCE ZONE AND SIMILARITIES WITH OTHER SUBTROPICAL CONVERGENCE ZONES IN THE SOUTHERN HEMISPHERE

A Thesis
Presented to
The Academic Faculty

by

Matthew J. Widlansky

In Partial Fulfillment
of the Requirements for the Degree
Doctor of Philosophy in the
School of Earth and Atmospheric Sciences

Georgia Institute of Technology
December 2010

CLIMATE DYNAMICS OF THE SOUTH PACIFIC CONVERGENCE ZONE AND SIMILARITIES WITH OTHER SUBTROPICAL CONVERGENCE ZONES IN THE SOUTHERN HEMISPHERE

Approved by:

Peter J. Webster, Advisor
School of Earth and Atmospheric Sciences
Georgia Institute of Technology

Yi Deng
School of Earth and Atmospheric Sciences
Georgia Institute of Technology

Robert X. Black
School of Earth and Atmospheric Sciences
Georgia Institute of Technology

Rosana Nieto-Ferreira
Department of Geography
East Carolina University

Judith A. Curry
School of Earth and Atmospheric Sciences
Georgia Institute of Technology

Date Approved: 12 October 2010

I was struck by the precise similarity of the clouds, sky, peculiarities of wind, and weather, to what we had been accustomed to meet with off the coast of Patagonia: and I may here remark that, throughout the southern hemisphere, the weather, and the turn or succession of winds, as well as their nature and prognostications, are remarkably uniform.

Captain Fitz-Roy,
Narrative of the surveying voyages of His Majesty's Ships Adventure and Beagle between the years 1826 and 1836

ACKNOWLEDGEMENTS

I am grateful to my advisor, Peter Webster, for his enthusiastic guidance and for providing an inspiring challenge to learn the dynamics of the SPCZ. I also owe thanks to my thesis committee members, Robert Black, Judith Curry, Yi Deng, and Rosana Nieto-Ferreira for granting their expertise reviewing details of this work. I additionally would like to recognize a few of my earlier professors, Emanuele Di Lorenzo, Robert Dickinson, and Rong Fu, whose knowledge of ocean-atmosphere interactions, numerical modeling, and convective processes encouraged greater understanding of the climate system. Carlos Hoyos deserves recognition for many theoretical contributions to this project and it has been an honor to collaborate with him. Fred Kucharski provided expertise specific to the ICTP model and greatly assisted setting up the numerical experiments.

Advice from research group members Hai-Ru Chang, Hyemi Kim, and Violeta Toma has been a great help along the way. Also deserving of my thanks are those I have shared an office with: Jason Furtado, Mark Jelinek, Asuka Suzuki-Parker, Sara Viera, and Wenxian Zhang and I have enjoyed working with many other colleagues including James Belanger, Fernando Hirata, and Manual Zuluaga.

Finally, I thank those outside of my academics who supported me in countless ways. I was fortunate to have great friendship in my GT Sailing teammates and I will look back with fondness at having what felt like a second home racing sailboats. As for my first home, I could not have begun a challenge such as this without the support of my parents and my sister, Sarah. They encouraged pursuit of my lifelong passion in weather since my youth in South Florida. Deserving special thanks is Benton Whitesides– for being on this journey with me. She has been a sounding board for technical discussion, kindly offered editorial advice, and provided endless positive moral. Thank you for all you have done!

TABLE OF CONTENTS

LIST OF TABLES

LIST OF FIGURES

LIST OF SYMBOLS AND ABBREVIATIONS

a	Earth's radius.
β	equatorial $\beta-$plane.
C_{gd}	local Doppler-shifted group speed.
C_{gx}	longitudinal group speed.
C_p	specific heat at constant pressure.
D	resultant deformation magnitude.
D_1	total stretching deformation.
D_2	total shearing deformation.
ϵ	wave action density.
f	frequency or Coriolis parameter.
$\frac{\partial \Phi}{\partial y}$	atmospheric thickness gradient.
Φ	geopotential height.
g	gravitational acceleration.
h	equivalent depth.
H	scale height.
J	diabatic heating rate.
k	longitudinal or zonal wave number.
m	vertical wave number.
n	latitudinal nodal number.
N	buoyancy frequency.
$-\omega$	vertical pressure velocity.
ω_r	intrinsic frequency.
p	atmospheric pressure.
$\mathbf{Q}$	**Q** vector.
R	gas constant for dry air.

ρ	density.
$\frac{dSST_{basin}}{dx}$	zonal SST gradient of the basin.
T	atmospheric temperature.
θ_d	axis of dilation.
$\overline{u}^*$	deviation of mean eastward component of wind from its zonal mean.
$\overline{U}$	zonal wind climatology.
$\partial\overline{U}/\partial x$	zonal stretching deformation climatology.
$\partial\overline{U}/\partial y$	meridional shear of the zonal flow climatology.
$\partial\overline{U}/\partial z$	vertical zonal wind shear climatology.
u'	zonal wind deviation from climatology.
$\overline{U_g}$	geostrophic zonal wind climatology.
$\overline{U}_x$	derivative of zonal wind climatology with respect to longitude (i.e., zonal stretching deformation).
$[v]$	zonal average of meridional mean wind.
$\overline{V}$	meridional wind climatology.
$\partial\overline{V}/\partial x$	zonal shear of the meridional wind climatology.
$\partial\overline{V}/\partial y$	derivative of meridional wind climatology with respect to latitude (i.e., meridional divergence).
v'	meridional wind deviation from climatology.
φ	latitude range.
ξ	wave energy density.
ψ_M	meridional mass stream function.
ψ_Z	zonal mass stream function.
AGCM	atmospheric general circulation model.
CDC	Climate Diagnostics Center.
CGCM	coupled general circulation model.
CLIVAR	World Climate Research Programme (WCRP) project that addresses climate variability and predictability.

CMIP3	WCRP Coupled Model Intercomparison Project phase 3.
CPAC	central Pacific.
CPC	Climate Prediction Center.
DJF	December, January, February.
ECMWF	European Centre for Medium-Range Weather Forecasts.
ENSO	El Niño-Southern Oscillation.
EPAC	eastern Pacific.
ERA15	ECMWF reanalysis.
GFDL CM2.1	Geophysical Fluid Dynamics Laboratory coupled general circulation model, version 2.1.
GPCP	Global Precipitation Climatology Project.
ICTP AGCM	International Centre for Theoretical Physics atmospheric general circulation model.
IPCC	Intergovernmental Panel on Climate Change.
ITCZ	Intertropical Convergence Zone.
JJA	June, July, August.
MAM	March, April, May.
MIXED	"mixed" eastern and central Pacific.
MJO	Madden-Julian oscillation.
NCAR	National Center for Atmospheric Research.
NCEP	National Center for Environmental Prediction.
NDJFM	November-March.
NOAA	National Oceanic and Atmospheric Administration.
OI	optimum interpolation.
OLR	outgoing longwave radiation.
ONI	Oceanic Niño Index.
PCCSP	Pacific Climate Change Science Program.
PKE	eddy perturbation kinetic energy.

SACZ	South Atlantic Convergence Zone.
SICZ	South Indian Convergence Zone.
SLP	sea-level pressure.
SON	September, October, November.
SPCZ	South Pacific Convergence Zone.
SPICE	Southwest Pacific Ocean Circulation and Climate Experiment.
SPREP	Secretariat of the Pacific Regional Environment Programme.
SST	sea surface temperature.

SUMMARY

Three semi-permanent cloud bands exist in the Southern Hemisphere extending southeastward from the equator, through the tropics, and into the subtropics. The most prominent of these features occurs in the South Pacific and is referred to as the South Pacific Convergence Zone (SPCZ). Similar convergence zones, with less intensity, exist in the South Atlantic and South Indian oceans. Convection in each basin is most pronounced during the austral summer season, especially in the SPCZ, which is the focus here. During this period, storminess veers away from equatorial convection over the warm pool and often appears to connect with the baroclinic zone of the extratropical South Pacific. Numerous studies have examined these diagonal cloud bands and occasionally described the convergence zones as regions where cold fronts become quasi-stationary, yet a dynamical explanation of these features is lacking. We propose a general hypothesis, based on the kinematic behavior of synoptic waves, which explains why convection veers southward into the higher latitudes of each basin.

We examine in detail the South Pacific climate using a combination of satellite observations and reanalysis data, prior to analyzing simulations of the South Pacific climate in two atmospheric general circulation models (GCMs). One model is coupled and the other one is uncoupled with the ocean. In the equatorial region of the SPCZ, convection slowly varies on intraseasonal timescales, while higher frequency variability is observed poleward of 20°S where synoptic disturbances provide most of the convective variance. The subtropical jet stream transects the South Pacific, but upper tropospheric (200 hPa) zonal winds decelerate around 150°W in a region just southwest of the maximum zonal sea surface temperature (SST) gradient. Decelerating zonal winds are collocated with the

deepest convection at that latitude (20°S-35°S).

Many global climate models are unable to simulate the poleward veering of convection in the SPCZ for a variety of reasons; however, the two atmospheric models examined here both depict the salient properties of the South Pacific climate, although subtle biases exist. In the coupled ocean-atmosphere GCM, a spurious horizontal band of convection extends east from the tropical SPCZ towards the equatorial East Pacific where the meridional SST gradient is too large. The uncoupled GCM is forced by fixed monthly varying SSTs and convection biases are much smaller in the East Pacific; however, the simulated SPCZ appears weaker and more zonally oriented than observed. In spite of these biases, each model simulates convection extending poleward in a diagonal band collocated with decelerating 200 hPa westerly winds. We further utilize the uncoupled GCM, due to its inherent simplicity, in a series of controlled numerical experiments which examine the long wave circulation response to altered boundary conditions, such as a prescribed SST gradient.

Based on the long wave circulation patterns identified in observations and simulations, we explain the physical mechanisms that promote the diagonal orientation of the SPCZ and the processes that determine the timescales of its variability. Previous studies have argued that slowly varying SST patterns produce upper tropospheric wind fields that vary substantially in longitude. In regions where 200 hPa zonal winds decrease with longitude (i.e., negative zonal stretching deformation, or $\partial\overline{U}\big/\partial x < 0$), the group speed and scale of eastward propagating synoptic (3-6 day period) Rossby waves is reduced and the wave energy density locally increases. We find that such a region of wave accumulation occurs in the vicinity of the SPCZ where the subtropical jet decelerates, thus providing a physical basis for the diagonal orientation and earlier observations that the zone acts as a "graveyard" of propagating synoptic disturbances. In essence, $\partial\overline{U}\big/\partial x = 0$ demarks the boundary of the graveyard while regions where $\partial\overline{U}\big/\partial x < 0$ denote the graveyard itself.

We use a series of idealized numerical experiments to determine factors that control

the Southern Hemisphere circulation patterns which produce negative zonal stretching deformation in the SPCZ region and then use statistical analyses of observations to provide evidence that wave energy accumulation occurs there. The experiments confirm that the Pacific zonal SST gradient forces a region of $\partial\overline{U}\big/\partial x < 0$ that is collocated with the deepest convection in the subtropics. Observations of the large-scale circulation response during El Niño, when the zonal SST gradient is typically small, support the modeling results. Composites of the life cycles of synoptic disturbances confirm the hypothesis that wave propagation slows and storms become more energetic in the $\partial\overline{U}\big/\partial x < 0$ region. The vertical structure of these disturbances also becomes enhanced as wave energy accumulates, further explaining why convection increases in the SPCZ.

From the wave energy accumulation results and graveyard hypothesis comes a more general theory accounting for the SPCZ's spatial orientation and its longer term variability influenced by the El Niño-Southern Oscillation (ENSO), or alternatively, the changing background SST associated with different phases of ENSO. The South Atlantic basin shares many climate features with the South Pacific and wave energy accumulation appears to also occur in the South Atlantic Convergence Zone (SACZ), although zonal SST gradients are smaller and land surface heating more directly forces the basic state circulation near South America. Fewer similarities are evident in the Indian Ocean. Remaining questions concern how the SPCZ may feedback onto the underlying SST pattern and planetary wave structure. Interaction between convection and the long wave circulation also suggests teleconnection avenues between each of the Southern Hemisphere convergence zones.

CHAPTER I

INTRODUCTION

An infrared view of Earth (Figure 1.1) reveals a number of persistent climate features. Subtropical oceans coincide with outgoing longwave radiation (OLR) maxima, indicating emission to space from the ocean surface with little attenuation. Minima in OLR, usually a proxy for deep convection and precipitation (Figure 1.2), are associated with equatorial continental regions (including the Indonesian archipelago), the tropical warm pools of the Pacific and Indian oceans, and baroclinic disturbances in the mid-latitudes. In the tropics, deep convection is collocated with the warmest sea surface temperatures (SSTs) except in regions of strong cross-equatorial pressure gradients in the lower troposphere where convection lies equatorward of the maximum SST (Toma and Webster 2009). During austral summer (DJF), there are also a number of equally prominent regions where deep convection (minimum OLR) appears to connect equatorial convective regions with baroclinic zones of the extratropical Southern Hemisphere. The most prominent of these bands is the South Pacific Convergence Zone (SPCZ), stretching between the warm pool convection and the South Pacific. Somewhat weaker are the South Atlantic Convergence Zone (SACZ) and the South Indian Convergence Zone (SICZ). There is little evidence of similar bands in the Northern Hemisphere, except during boreal summer (JJA) when convection associated with the Southeast Asian monsoon and Baiu frontal zone (e.g., Kodama 1992) extends northeast from the equatorial Indian Ocean.

Existence of persistent and organized convective regions in the Southern Hemisphere became apparent at the beginning of the satellite era. Using pictures from the Tiros I meteorological satellite, Hubert (1961) identified "*a convergence line, a shear line, or even a stationary front*" in the Southwest Pacific. A number of subsequent studies (Kornfield

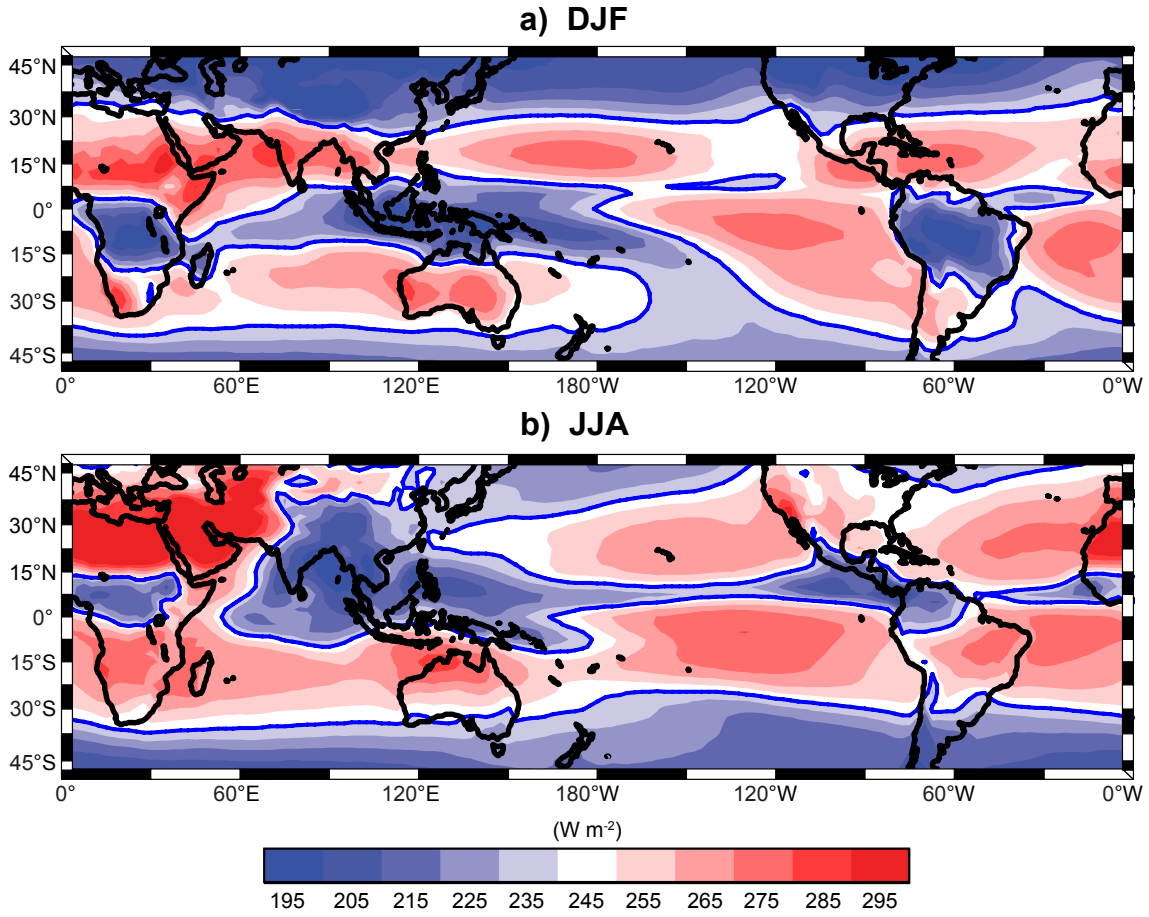

Figure 1.1: Global climatology (1982-2008) of OLR (W m^{-2}) for (a) DJF and (b) JJA. 240 W m^{-2} OLR contour outlined by blue lines in each panel.

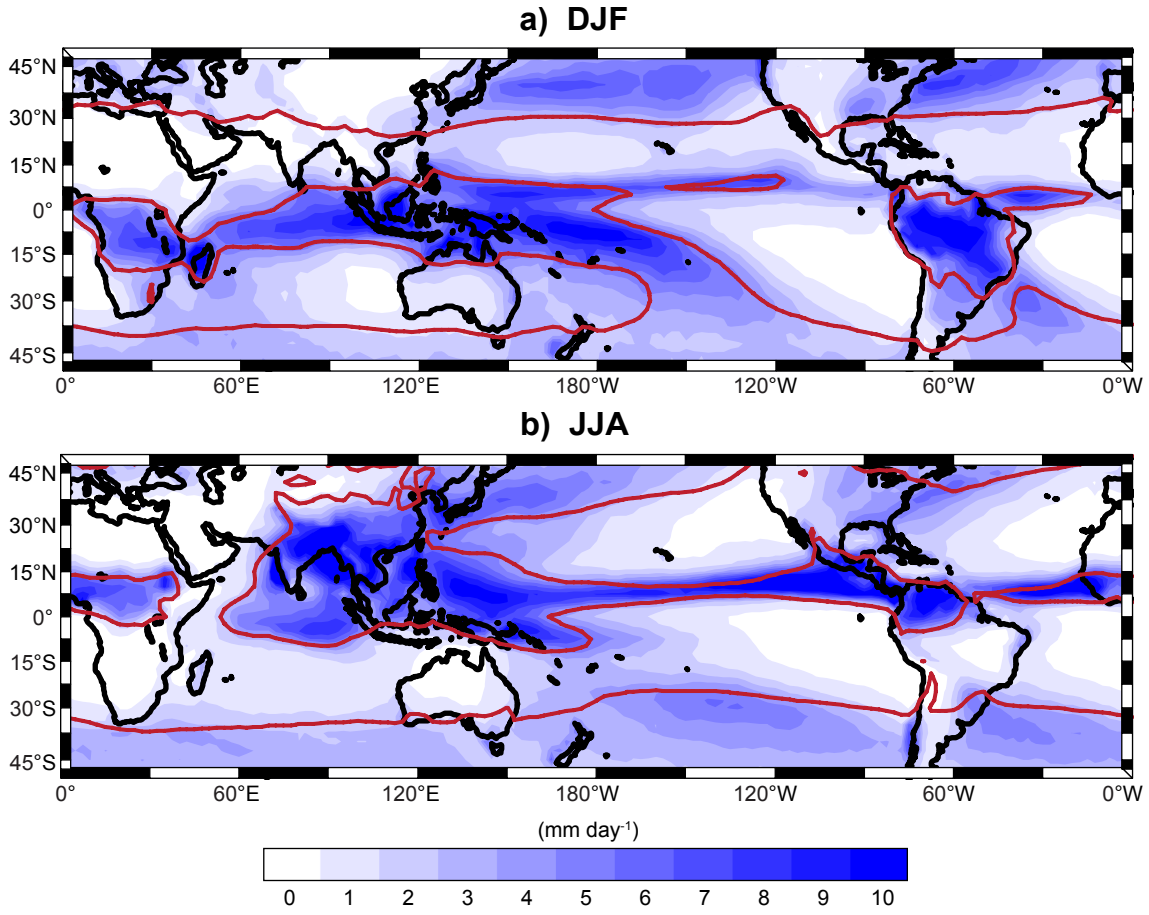

Figure 1.2: Average (1982-2008) monthly rate of precipitation (mm day^{-1}) during (a) DJF and (b) JJA. 240 W m^{-2} OLR contour outlined by red lines in each panel.

et al. 1967; Godshall 1968; Bjerknes et al. 1969; Booth and Taylor 1969; Leese et al. 1970; Streten 1970; Taljaard 1972) also noted predominant bright bands extending zonally and meridionally across the three Southern Hemisphere oceanic basins. These observations were consolidated by Streten (1973) who noted that the bands were regions of widespread convective activity and precipitation extending into the mid-latitudes from the equatorial land masses of Africa, the Indonesian archipelago, and the Amazon basin. Furthermore, Streten (1973) noted that the three bands were associated with long wave circulation patterns, described earlier by van Loon and Jenne (1972), and highly active on synoptic time scales. These features tended to be most stable in the South Pacific and South Atlantic but more variable in location and intensity, and with smaller magnitude, in the South Indian Ocean.

Overall, the majority of studies have concentrated on the most apparent and enduring of the convective bands: the SPCZ (e.g., Trenberth 1976; Vincent 1994, 1999); finding within the extensive cloud band pronounced spatial and temporal differences between the equator, tropics, and subtropics. Tropical convection, for example, is oriented zonally, associated with strong boundary layer convergence (e.g., Vincent 1994; Lintner and Neelin 2008), and located along gradients of SST (e.g., Lindzen and Nigam 1987). Further south, in the subtropics, the SPCZ becomes more diagonally oriented and appears to possess baroclinic-type disturbances with 4-5 day periodicities originating south of the Australian region (Streten 1973; Streten and Zillman 1984; Kiladis et al. 1989; Trenberth 1991). Streten (1973) found similar time scales of variability in the subtropical portions of the SACZ and SICZ as well. Variability in the tropical SPCZ, on the other hand, is dominated by periodicities longer than two weeks. The differences in variance periodicities with latitude suggest that the tropical and higher latitude SPCZ are influenced by different dynamical processes. However, the similar poleward slope of the three cloud bands suggests that the zones possess common roots.

Fewer studies have considered the SICZ and SACZ, although these were included in

the satellite climatology of Kuhnel (1989). Like the SPCZ, the other bands show variability over a wide range of time scales. The location and variability of the SICZ is critical with respect to the rainfall of southern Africa (van Heerden and Taljaard 1999; Todd and Washington 1998, 1999; Carvalho et al. 2002; Nicholson 2003). Similarly, Rickenbach et al. (2002) and Todd et al. (2003) find a dependency of South American rainfall on the variability of the SACZ. Linkages between variability in the Atlantic basin and the SPCZ are also observed (Rodwell and Hoskins 2001; Hoskins and Hodges 2005).

Interannual oscillations in the positioning of the SPCZ (Trenberth 1976; Streten and Zillman 1984; Trenberth 1997; Vincent 1999; Folland et al. 2002) suggest that slow SST modulations associated with the El Niño-Southern Oscillation (ENSO) may alter both the background climate circulation (e.g., Webster 1982; Juillet-Leclerc et al. 2006; Vincent et al. 2009) and the position of the diagonal cloud band. The quasi-stationary South Pacific SST pattern consists of large meridional and zonal temperature gradients. In the upper troposphere, winds are mostly easterly over the low latitude West Pacific warm pool and westerly in a concentrated jet stream to the south. Strong zonal gradients also exist in the wind field and appear spatially correlated with the underlying SST gradients. It is therefore reasonable to infer that the Pacific SST pattern may govern the positioning and intensity of not only basin-scale circulation features, but also the SPCZ. In essence, the location of the SPCZ is tied to the quasi-stationary long wave circulation of the hemisphere.

Many studies have proposed an important role for the East Pacific subtropical high in establishing a convective band to the west (e.g., Trenberth et al. 2000; Rodwell and Hoskins 2001; Trenberth and Stepaniak 2003; Takahashi and Battisti 2007b). Rodwell and Hoskins (2001), for example, describe how latent heating from monsoon convection over the Amazon basin strengthens the East Pacific high via an upstream Rossby wave response which produces adiabatic descent west of the Andes mountain range. Subsidence of low specific humidity air was later shown, through a series of modeling experiments (Takahashi and Battisti 2007a), to increase evaporative cooling in the East Pacific; thereby lowering

the local SST. Takahashi and Battisti (2007b) suggest that the subtropical high enhances the SPCZ by acting as a blocking mechanism for eastward propagating mid-latitude cyclones and providing diffluent meridional flow in the upper troposphere as originally suggested by Trenberth et al. (2000) and extrapolated upon by Trenberth and Stepaniak (2003). Previously, Renwick and Revell (1999) related blocking episodes over the higher latitude Southeast Pacific to wave trains originating from equatorial convection near the Dateline and found a strong association with ENSO. However, the actual physical mechanisms that constitute "blocking", on one hand, and local intensification of convection and synoptic variance within the SPCZ, on the other, remain obscure.

A clue to an overriding physical mechanism may be imbedded in the observations of Trenberth (1976). After describing the character of the SPCZ, he notes that the SPCZ "... *tends to form a 'graveyard' region for fronts moving from the southwest in the troughs of low pressure between the migratory anticyclones across Australia and New Zealand ...*". Trenberth (1991) also noted an association between the exit, or diffluent, region of the Southern Hemisphere subtropical jet stream and the location of the SPCZ. If the Trenberth (1976, 1991) observations are correct, then it would seem that the essence of an explanation may reside in the interactions of transient modes with the much more slowly varying background flow.

Other studies have suggested that the diagonal orientation of deep convection is related to the regional SST distribution as well as the location of the subtropical jet stream (Graham and Barnett 1987; Kiladis et al. 1989; Eastin and Vincent 1998; Yoshikane and Kimura 2003). Noting the importance of the SST distribution in forcing low-frequency atmospheric standing waves (e.g., van Loon and Jenne 1972; Webster 1982), these studies may be restating the notion that the SPCZ is forced by interactions between synoptic disturbances and low frequency variability of the background flow. Even so, there remains the basic question of why the quasi-stationary long waves produce regions of enhanced synoptic activity in three specific Southern Hemisphere locations.

Recently, the climate of the Southwest Pacific has become a focal point of research initiatives based on the hypothesis that the SPCZ is closely coupled with regional oceanic circulations and associated with large-scale atmospheric teleconnections (Ganachaud et al. 2007). These concerns have led to the design of a regionally coordinated experiment, the CLIVAR Southwest Pacific Ocean Circulation and Climate Experiment (SPICE), aimed at understanding the role of ocean circulation in the large-scale, low-frequency modulation of climate and generation of regional climate signatures, such as the SPCZ. A renewed call for dynamical understanding of the SPCZ came in August of this year when the Pacific Climate Change Science Program (PCCSP) sponsored an international scientific workshop on the subject at the Secretariat of the Pacific Regional Environment Programme (SPREP) office in Apia, Samoa. Portions of this thesis were presented at the Samoa workshop (Power 2010, manuscript submitted to *Eos, Trans. Amer. Geophys. Union*) and also discussed in Widlansky et al. (2010).

We focus on developing an understanding of why the SPCZ veers southward into higher latitudes away from the western Pacific Intertropical Convergence Zone (ITCZ). Furthermore, we explore why different periodicities dominate convective activity as a function of latitude. In the next chapter, we present a climatology of the SPCZ relative to both the long-term mean structure of the Southern Hemisphere and its higher frequency variance. Observations are then compared to simulations of the South Pacific climate in two atmospheric circulation models of similar spatial resolution, but either fully coupled, or uncoupled, with the ocean (Chapter 3). In Chapter 4, we propose a hypothesis suggesting that slowly varying upper troposphere zonal winds, driven in part by strong zonal SST gradients, foster regions suitable for the modification of mid-latitude Rossby waves. Chapter 5 tests the hypothesis that mid-latitude disturbances amplify in the SPCZ region when the wave characteristics are modified by the low frequency variability of the basic background flow. The testing is accomplished by controlled experiments using an atmospheric general circulation model (AGCM) to examine the sensitivity of the zonal wind basic state and

SPCZ orientation to both the Pacific SST pattern and location of the continents. We also explore temporal correlations on interannual timescales between the Pacific zonal SST gradient and intensity of the SPCZ. Composites of synoptic disturbances propagating through the SPCZ are then used to measure wave characteristics and perform diagnostics of their vertical structure. Applications of the wave modification hypothesis to the SACZ and SICZ are discussed in Chapter 6, extrapolating upon the general theory accounting for the SPCZ's spatial orientation (Widlansky et al. 2010). Finally, Chapter 7 provides a summary of results and remaining questions.

CHAPTER II

OBSERVED CLIMATOLOGY OF THE SPCZ

From the latter end of December to the beginning of March cloudy weather (with much rain, and westerly winds) is usual

–Captain Fitz-Roy (1839)

We examine in detail the 1982-2008 period within the region enclosed by 20°N-50°S and 120°E-70°W, defining the equatorial and southern parts of the Pacific basin. To gain an understanding of the spatial extent of the SPCZ, the mean OLR field during DJF is first shown. Significant modes of variability for convection in the equatorial, tropical, and subtropical regions are then compared. We next discuss the lower and upper tropospheric basic state circulation and surface boundary temperature forcing. Lastly, the mean zonal and meridional overturning atmospheric circulations and relationship to the subtropical jet stream and storm tracks are examined. Data sets used to depict the observed climatology are described in the Appendix (OLR: A.1, NCEP-NCAR reanalysis: A.3, and SST: A.4).

The DJF mean field of OLR (Figure 2.1), following Liebmann and Smith (1996), shows the SPCZ (enclosed by the 240 W m^{-2} OLR contour) extending from the tropical warm pool convection of the western Pacific in a southeastward direction towards the Southern Hemisphere mid-latitudes. A narrow equatorial strip of low OLR is also apparent and associated with the relatively weak boreal winter Northern Hemisphere ITCZ. DJF is chosen as it encloses the period of the year when the deepest convection occurs in the SPCZ. Stark longitudinal differences are observed. In the western part of the region, two convective maxima, associated with deep convection over Indonesia and a zone of extratropical disturbances, are separated by a convective minimum over Australia. The northern maximum extends eastward across the tropical warm pool, slopes southeast, and joins the extratropical convective maximum through the diagonally oriented SPCZ. To the east of the SPCZ,

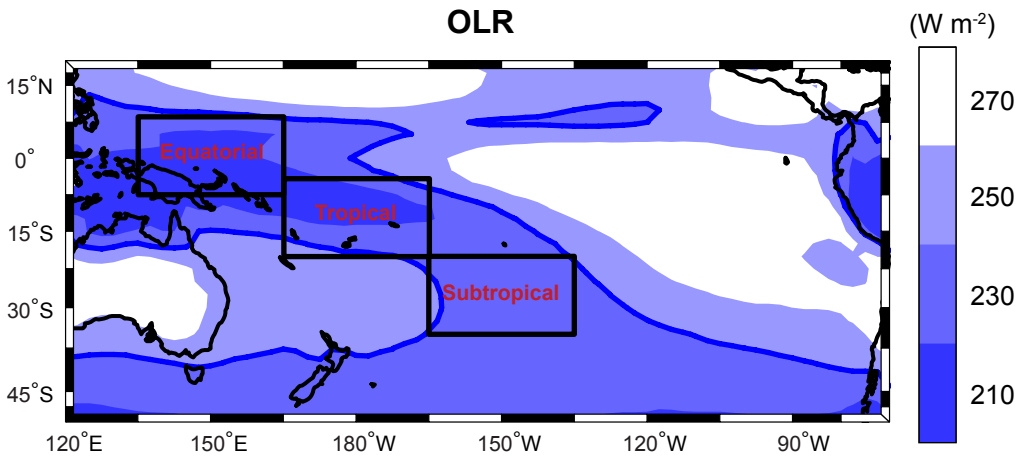

Figure 2.1: DJF climatology (1982-2008) of OLR (W m^{-2}). Black boxes represent the "Equatorial" (7.5°N-7.5°S, 135°E-165°E), "Tropical" (5°S-20°S, 165°E-165°W), and "Subtropical" (20°S-35°S, 165°W-135°W) SPCZ regions referred to in the text. 240 W m^{-2} OLR contour outlined by blue lines.

OLR values increase substantially indicating minimum convection and subsidence over the Pacific subtropical high pressure system.

2.1 Modes of variability

The standard deviation of OLR over the Pacific basin (Figure 2.2a) exceeds 35 W m^{-2} along a diagonal band corresponding to the climatological orientation of the SPCZ, or the region enclosed by the 240 W m^{-2} mean OLR contour, computed here for the November through March (NDJFM) period and indicated by gray lines for visual clarity. Normalized Fourier power spectra of OLR time series are used to compare the modes of variability for the equatorial, tropical, and subtropical SPCZ regions (Figure 2.2b-d, respectively). We use NDJFM daily OLR anomalies to provide 27 seasonal time series of sufficient temporal resolution and length for analyzing synoptic (3-6 day) to intraseasonal (30-60 day) variability. Red-noise spectra (lower-dashed lines) for mean lag-1 autocorrelations of 0.90 (b), 0.78 (c), and 0.70 (d) along with the corresponding 95% confidence spectra (upper-dashed lines) are calculated using the methods of Torrence and Compo (1998) with the assumption that each season is independent. This provides 26 degrees of freedom.

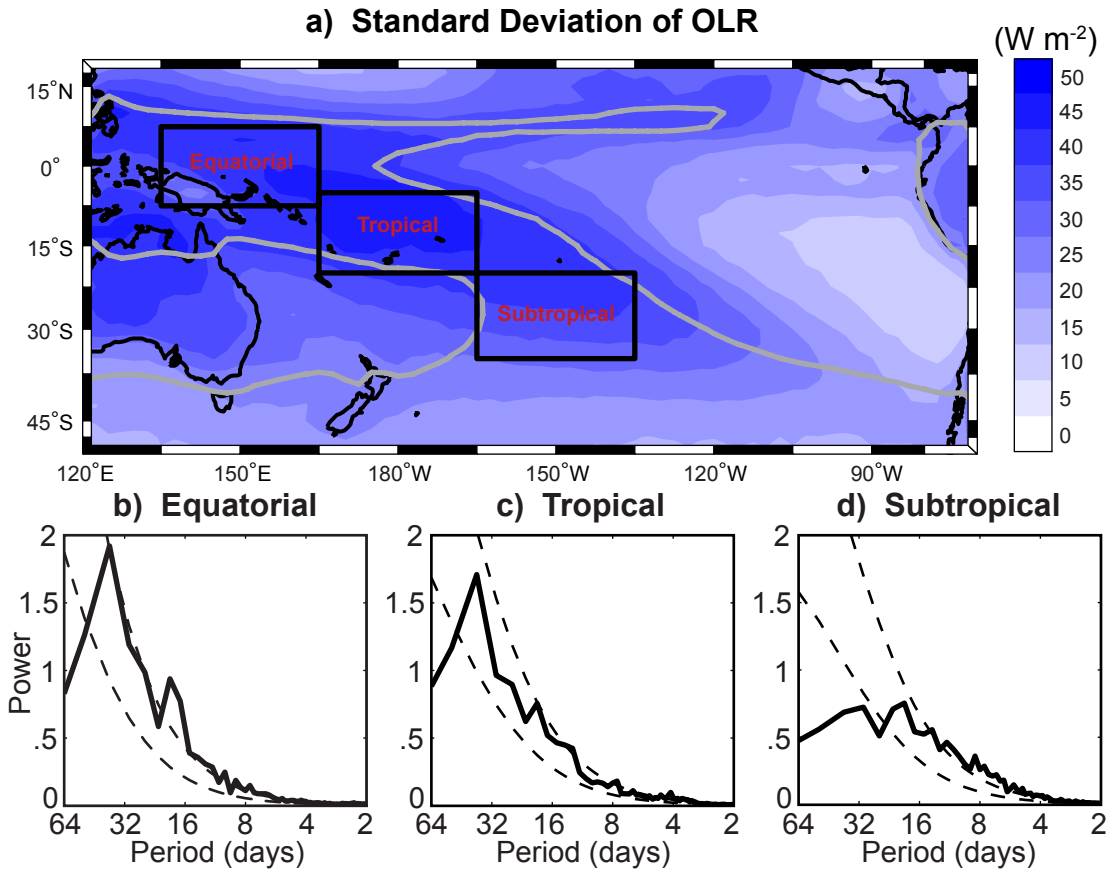

Figure 2.2: (a) Standard deviation of daily OLR anomalies (W m^{-2}) from NDJFM (1982-2008). 240 W m^{-2} OLR contour outlined by gray lines. Black boxes represent the "Equatorial" (7.5°N-7.5°S, 135°E-165°E), "Tropical" (5°S-20°S, 165°E-165°W), and "Subtropical" (20°S-35°S, 165°W-135°W) averaging regions for calculating OLR time series. (b, c, and d) Average Fourier power spectra of OLR in the equatorial, tropical, and subtropical regions of the SPCZ, respectively. Lower dashed lines are the red-noise spectra for mean lag-1 autocorrelations of 0.90 (b), 0.78 (c), and 0.70 (d). Upper dashed lines are the 95% confidence spectra.

In the equatorial and tropical SPCZ, variability peaks around 2 weeks and between 30-60 days (Figure 2.2b and c, respectively) with variance decreasing markedly towards shorter time scales. These spectra suggest that equatorward of 20°S, the SPCZ is strongly influenced by intraseasonal variability (e.g., the Madden-Julian oscillation or MJO) and other convective oscillations on timescales greater than 2 weeks. Further discussion of the MJO influence on the SPCZ is found in Matthews et al. (1996) and Widlansky (2007). While some evidence of a 2 week spectral peak also exists in the subtropical time series (Figure 2.2d), most of the significant OLR variability is constrained to synoptic timescales of less than 8 days. Mean lag-1 autocorrelations also decrease away from the tropics. The shift toward higher frequency variability poleward of 20°S suggests that synoptic disturbances provide most of the convective variance in the subtropical part of the SPCZ.

Zonal wavenumber-frequency ($k - f$) power spectra of daily OLR anomalies are computed for the DJF period, following Wheeler and Kiladis (1999), to distinguish between travelling and stationary waves. Comparison is also made between wave characteristics in equatorial and subtropical latitudes. For each analysis, OLR time series are longitudinally tapered to isolate variability in the Pacific (120°E-70°W). Some erroneous spectral peaks exist, attributed to the satellite sampling rate (Liebmann and Smith 1996; Wheeler and Kiladis 1999), which are especially prevalent around wavenumber 14. Figure 2.3 shows the (a) symmetric and (b) antisymmetric components of OLR power integrated between 15°N-15°S. Concentrations of power corresponding to Kelvin, Rossby, and inertia-gravity waves, as originally described by Matsuno (1966), are evident in the symmetric component. There is also high variance between wavenumbers 1-4 and periods of 30-60 days corresponding to the frequency of the MJO signal that was detected in the equatorial power spectra analysis (Figure 2.2a). Mixed Rossby gravity waves are apparent in the antisymmetric spectrum, along with a spurious peak ($k = 14$ days, $f \approx 0.125$) attributed to characteristics of the satellite orbit.

Pronounced differences are apparent in the wavenumber-frequency spectra of OLR in

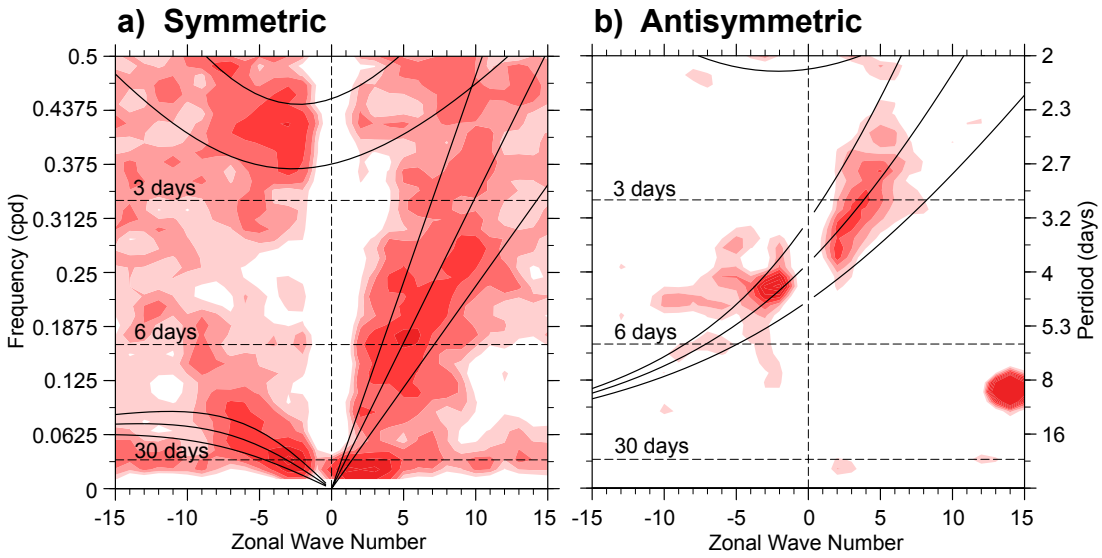

Figure 2.3: Zonal wavenumber-frequency power spectra of the (a) symmetric and (b) antisymmetric components of daily OLR anomalies calculated for the DJF period 1980-2006 as described in Wheeler and Kiladis (1999). Power has been integrated between 15°N-15°S and tapered to isolate the Pacific signal (120°E-70°W). Both components have been scaled by the background spectra by using many times a 1-2-1 filter in frequency and wavenumber. The base-10 logarithm has been taken for plotting purposes. Superimposed are the dispersion curves of selected equatorially trapped waves for equivalent depths of 12, 25, and 50 meters (solid lines). Positive (negative) wavenumbers correspond to eastward (westward) propagating waves.

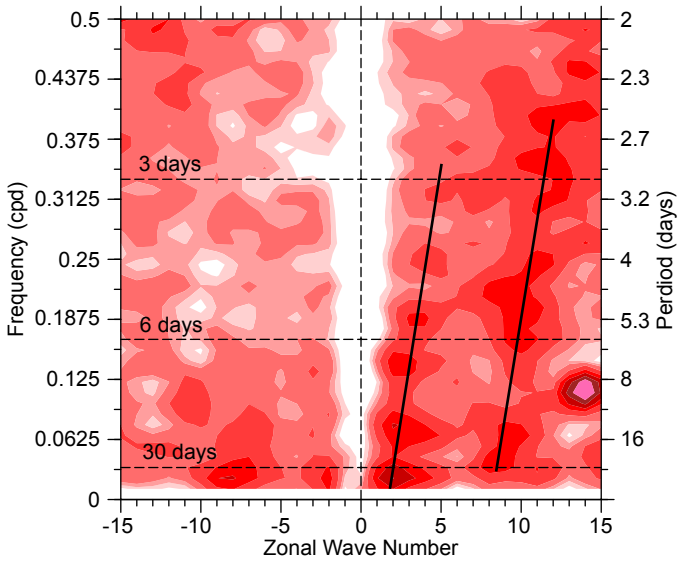

Figure 2.4: Same as Figure 2.3 but for the symmetric component of the subtropical Pacific signal (20°S-35°S, 120°E-70°W). Solid black lines highlight prominent westward propagating waves.

the subtropical (20°S-35°S) Pacific (Figure 2.4). Here, convection is more variable, at most frequencies and zonal wave numbers, than near the equator. In previous wavenumber-frequency diagnostics of the Northern Hemisphere mid-latitude storm track (e.g., Willson 1975; Fraedrich and Böttger 1978), three isolated spectral peaks were noted in geopotential height fields. Propagating long and short waves correspond to larger and smaller cyclones, while quasi-stationary planetary-scale waves are thermally and orographically forced. The travelling long waves resemble Rossby-type waves superimposed on quasi-stationary oscillations (Willson 1975), with the longest waves sometimes moving westward. Similar wavenumber-frequency patterns are observed in the OLR time series from the South Pacific. Two diagonal lines are superimposed on Figure 2.4 to denote power maxima associated with eastward propagating long ($k < 5$) and short waves ($k > 7$). Quasi-stationary waves ($f < 0.033$ days^{-1}) contain more variance at low wavenumbers than travelling waves and represent a basic state circulation with similar scale to the Pacific basin.

2.2 *Basic state circulation*

Contrasting long wave atmospheric circulation patterns exist between the warm equatorial West Pacific and much cooler waters of the Southern Ocean. Transecting the Pacific is a diagonal band of deep convection (i.e., the SPCZ) which varies on a variety of timescales. Figure 2.5a and b displays, respectively, the 850 hPa and 200 hPa geopotential height (Φ) and wind field ($\overline{U}$ and $\overline{V}$) climatology from the NCEP-NCAR reanalysis data (Kalnay et al. 1996; Kistler et al. 2001) in the context of the SPCZ orientation. In both panels, the bold blue contour (OLR = 240 W m^{-2} from Figure 2.1) encloses deep penetrative convection across the SPCZ and outlines clearly the poleward extent of the diagonal convective zone. The large black box extends from 20°S-35°S and denotes the subtropical region where time series of OLR and dynamical quantities will be extracted.

Figure 2.5a shows the lower tropospheric basic state. The highest heights of the 850 hPa pressure level are found over the cool Southeast Pacific. Around the lower troposphere high, the circulation is anti-cyclonic with westerly winds around 40°S and easterly flow to the north. Heights gradually decrease equatorward and the easterly trade winds become stronger. Convergence of the easterly flow occurs over the West Pacific and is evidence of the equatorial trough. The OLR 240 W m^{-2} contours enclose a region of lower troposphere convergence extending between the equatorial trough and the western periphery of the East Pacific high. Poleward of 40°S, 850 hPa heights abruptly decrease and the wind near the surface becomes mostly westerly.

Strong coupling between the circulation at 850 hPa and the upper tropospheric geopotential height pattern is evident by comparison of Figure 2.5a and b. Further discussion of zonal and meridional overturning circulations, which link the lower and upper troposphere, is provided in Chapter 2.4. Here, we note that the 200 hPa pressure level is highest near the equator and decreases poleward. In general, the height of the 200 hPa wind field parallels the SST distribution with greater heights occurring over warm SSTs and lower heights over cooler regions. Meridional geopotential height gradients are enhanced over the western and

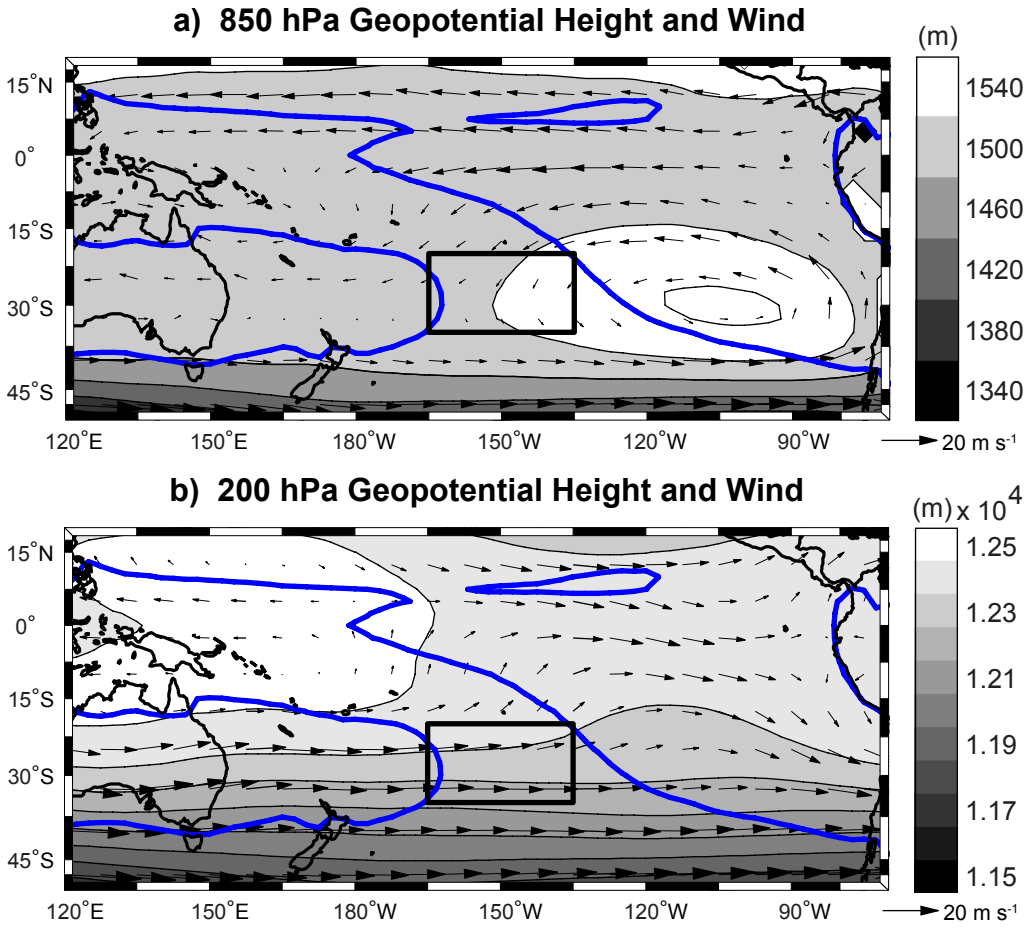

Figure 2.5: (a) DJF climatology (1982-2008) of 850 hPa geopotential height (m, shading) and winds (m s^{-1}, vectors). Large black box (located at 20°S-35°S, 165°W-135°W) represents the averaging region for calculating OLR and stretching deformation time series. 240 W m^{-2} OLR contour outlined by blue lines. (b) 200 hPa geopotential height and winds.

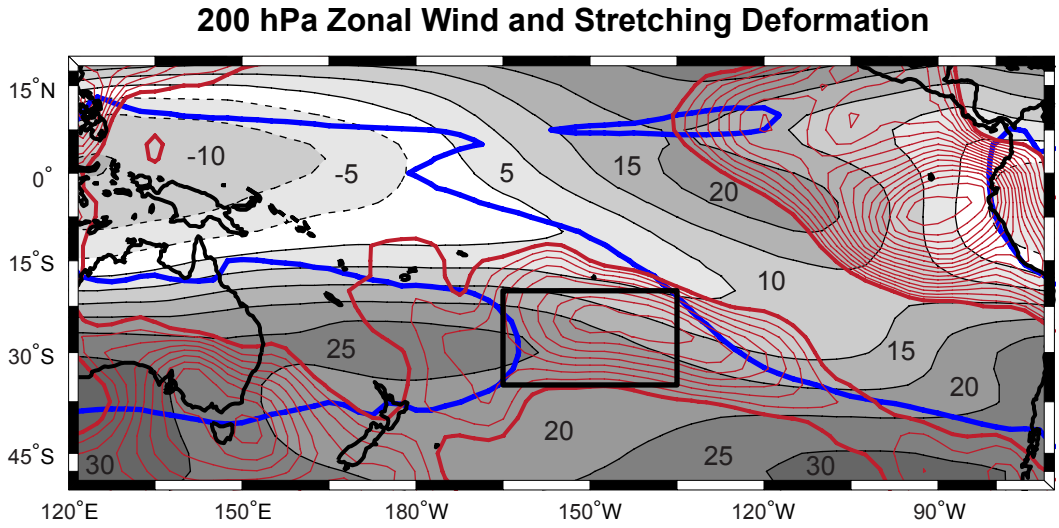

Figure 2.6: DJF climatology (1982-2008) of 200 hPa zonal winds (5 m s^{-1} shading interval, dashed lines depict negative zonal winds, zero contour omitted) and negative zonal stretching deformation (s^{-1}, red contours). Zonal stretching deformation contour interval: -5 x 10^{-7} s^{-1}; thick lines depict the zero contour. Large black box located at 20°S-35°S, 165°W-135°W represents the averaging region for calculating OLR and stretching deformation time series. 240 W m^{-2} OLR contour outlined by blue lines.

eastern parts of the Pacific basin and are consistent with the location of the subtropical jet stream maxima near Australia and South America.

An analysis of the 200 hPa zonal wind component ($\overline{U}$: Figure 2.6) is performed to determine steering currents of mid-latitude synoptic waves which may impact the SPCZ diagonal region. Superimposed on the upper tropospheric zonal wind field are red contours of $\partial\overline{U}/\partial x < 0$, the negative stretching deformation of the zonal wind field. Westerly winds are outlined by solid black contours to highlight the subtropical jet stream location (poleward of 20°S), as well as equatorial westerlies over the central Pacific. To the northeast of the SPCZ, strong westerlies extend from the Northern Hemisphere into the central South Pacific. This is the "westerly duct" (Webster and Holton 1982; Tomas and Webster 1994; Duane et al. 1999) through which disturbances of one hemisphere can potentially influence the other hemisphere over a wide range of frequencies. Weaker easterlies are observed over the tropical warm pool.

The diagonal SPCZ (enclosed by the blue OLR contours between 20°S-35°S) lies in a region of decreasing westerly winds to the east of the Australian subtropical jet stream maximum (i.e., the jet stream exit region). The jet is perpendicular to the poleward gradients of surface temperature and 200 hPa geopotential height, or atmospheric thickness gradient ($\frac{\partial \Phi}{\partial y}$). Following Holton (2004), and noting that zonal flow is quasi-geostrophic for synoptic-scale motions ($\overline{U} \approx \overline{U_g}$), we see that the zonal jet is related to the thickness gradient:

$$\overline{U_g} = -\frac{1}{f}\frac{\partial \Phi}{\partial y} \tag{1}$$

where f is the Coriolis parameter and $\frac{\partial \Phi}{\partial y}$ points from the equator towards the mid-latitudes, parallel to the meridional SST gradient (discussed in Chapter 2.3). Large meridional height gradients, around 30°S in the West Pacific, force strong 200 hPa westerlies (Figure 2.5b). Smaller Φ gradients, such as in the central Pacific, force weaker zonal winds. The subtropical jet stream typically decelerates between these two regions, resulting in negative zonal stretching deformation ($\partial\overline{U}\big/\partial x < 0$, depicted by red contours). For later reference, these contours show maximum values in the exit region of the subtropical jet stream denoted by the black box. Although subtropical westerlies are much weaker during DJF than in winter, previous studies (reviewed by Vincent 1999) found convection in the SPCZ related to the summer jet, but physical mechanisms explaining the interaction remained elusive. At this stage, we note that a region of negative zonal stretching deformation is collocated with the SPCZ in the subtropics.

The zonal component of the upper tropospheric flow is an order of magnitude greater than the meridional winds, as evident by the orientation and magnitude of vectors in Figure 2.5b. However, the 200 hPa meridional flow ($\overline{V}$) is diffluent near the subtropical SPCZ and is now considered. Divergence in the latitudinal direction (i.e., $\partial\overline{V}\big/\partial y > 0$) supports outflow from deep convection (e.g., Vincent 1999) and, perhaps, lends to a diagonally oriented cloud band. In this region, horizontal shearing of the zonal ($\partial\overline{U}\big/\partial y$) and meridional ($\partial\overline{V}\big/\partial x$) flow also occurs. We therefore briefly consider here the total stretching (D_1) and

shearing (D_2) deformation of the mean 200 hPa flow:

$$D_1 = \frac{\partial \overline{U}}{\partial x} - \frac{\partial \overline{V}}{\partial y} \tag{2}$$

$$D_2 = \frac{\partial \overline{V}}{\partial x} + \frac{\partial \overline{U}}{\partial y} \tag{3}$$

The resultant deformation magnitude (D) is rotationally invariant (Bluestein 1977) and may be defined as the sum of the squares of each deformation component:

$$D = D_1^2 + D_2^2 \tag{4}$$

Following Bluestein (1977), the axis of dilation (θ_d), or action of expansion, is also calculated from D_1 and D_2:

$$\theta_d = \frac{1}{2}\tan^{-1}\left(\frac{D_2}{D_1}\right) \tag{5}$$

Figure 2.7 shows the total stretching deformation (D_1: red contours), resultant deformation magnitude (D: proportional to the length of tick marks), and axis of dilation (θ_d: tick mark orientation) of the 200 hPa flow. Negative total stretching deformation (i.e., $D_1 < 0$) is collocated with the SPCZ poleward of 15°S and exceeds the magnitude of $\partial\overline{U}\big/\partial x < 0$ (comparison of red contours in Figures 2.6 and 2.7). The resultant deformation magnitude is also large and oriented diagonally, from northwest to southeast, within the boundaries of the SPCZ. The striking collocation of $D_1 < 0$ and low OLR, along with the diagonal orientation of θ_d (Bluestein 1977), suggests that weak divergence of the meridional flow further supports a diagonally oriented South Pacific cloud band. However, for the remainder of this study, we restrict consideration of stretching deformation forcing on the SPCZ to only the zonal wind component.

2.3 Surface boundary forcing

The corresponding SST climatology (Reynolds et al. 2002) is shown in Figure 2.8. The large black box (labeled "A") extends from 20°S-35°S and denotes the subtropical SPCZ

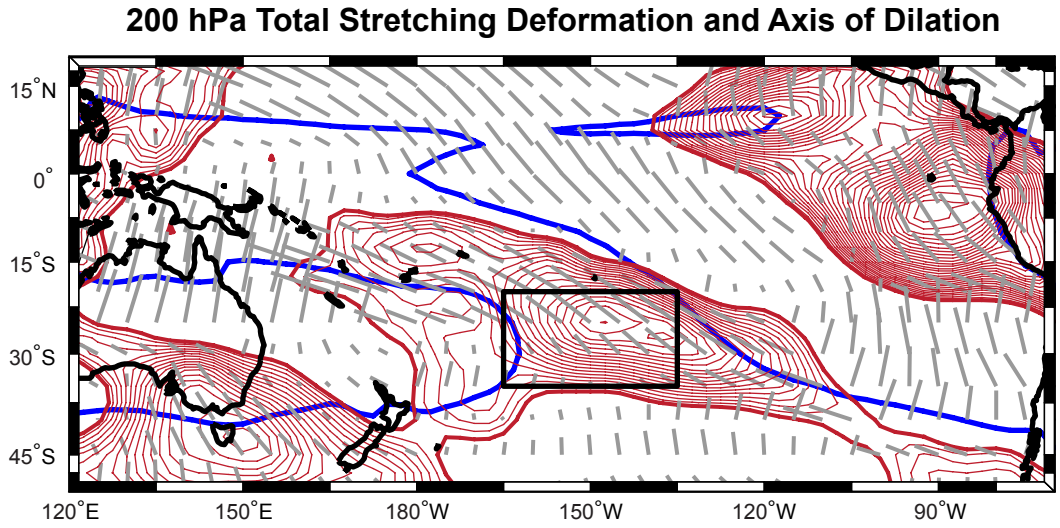

Figure 2.7: Same as Figure 2.6 except for the total negative stretching deformation (s^{-1}, red contours) and axis of dilation (gray tick marks) of the 200 hPa flow. Total stretching deformation contour interval: -5 x 10^{-7} s^{-1}; thick lines depict the zero contour. Orientation of each tick mark denotes the axis of dilation orientation and the length is proportional to the resultant deformation magnitude, as described in Bluestein (1977).

region. Two smaller boxes ("B" and "C") are used to compute zonal gradients of SST. Temperatures greater than 28°C are shaded to designate the spatial extent of the West Pacific warm pool. A basin-scale meridional (zonal) SST gradient is observed south (southeast) of the warm pool. The eastern boundary of the SPCZ (defined arbitrarily by the 240 W m^{-2} OLR contour between 20°S-35°S) transects the meridional SST gradient and is located southwest of the maximum zonal SST gradient, which exceeds 5°C across the subtropical South Pacific. This gradient is calculated as the difference between the mean SST in box B and box C which are separated by about 6,300 km.

Figure 2.9 shows the large-scale zonal component of the SST gradient calculated following the methods of Rowell (2001). Two SST averaging regions (15° latitude by 60° longitude) are defined for each grid point such that the latitudes of their centers are the same latitude as the grid point. The relative dimensions of the averaging boxes reflect the greater length-scale of SST anomalies in the zonal direction and also approximate the longitudinal distance between boxes B and C. Each grid point separates a "western" and

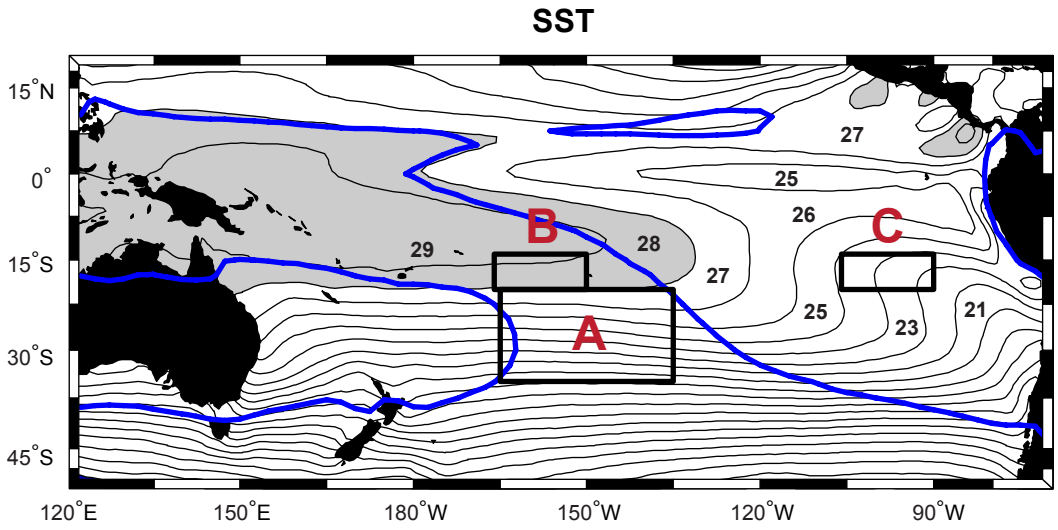

Figure 2.8: DJF climatology (1982-2008) of SST (1°C interval, gray shading indicates temperatures above 28°C). Large black box ("A" located at 20°S-35°S, 165°W-135°W) represents the averaging region for calculating OLR and stretching deformation time series. Small black boxes ("B" and "C" located at 14.5°S-20.5°S, 165.5°W-149.5°W and 14.5°S-20.5°S, 105.5°W-89.5°W, respectively) denote regions used to calculate the SST index. 240 W m^{-2} OLR contour outlined by blue lines.

"eastern" box. The difference between their average SSTs, divided by the distance between their centers, is the large-scale zonal SST gradient (°C 1,000 km^{-1}). Gray shading indicates where SSTs decrease from west to east; on condition that at least 40% of each averaging region is open water. Superimposed on the zonal SST gradient are contours of $\partial\overline{U}/\partial x < 0$. Minimum OLR and regional $\partial\overline{U}/\partial x < 0$ are collocated in the subtropical SPCZ (box A) and positioned slightly poleward and west of the maximum large-scale zonal SST gradient (confirmed by Figure 2.9 to be between box B and box C). Statistical relationships between SST, OLR, and the character of the zonal flow are described further in Chapter 5.

2.4 Zonal and meridional overturning circulations

The Pacific basin is characterized by large-scale surface temperature gradients in the zonal and meridional directions (Figure 2.8). Pronounced longitudinal differences in the OLR climatology (Figure 2.1) are also observed. Intense precipitation occurs in the region of

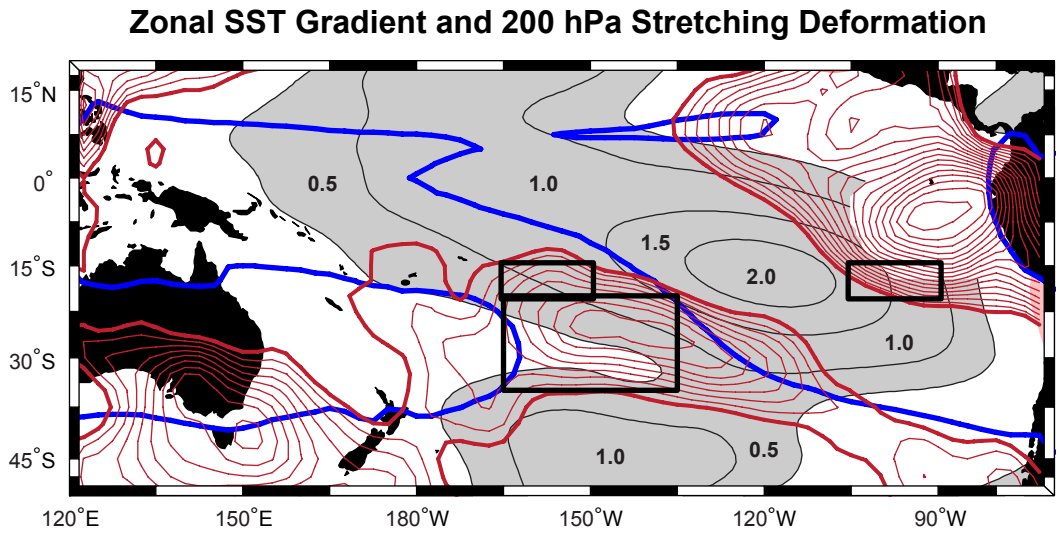

Figure 2.9: Same as Figure 2.8 except for zonal SST gradient (°C 1000 km^{-1}, shading) and 200 hPa zonal stretching deformation (s^{-1}, red contours).

the Indonesian archipelago and the tropical warm pool, extending southeastward along the SPCZ during DJF. Rising motion is driven by surface heating and latent heat release from convection in these regions, while diabatic cooling and subsidence is common in other parts of the Pacific. (Thermal forcing mechanisms of the overturning circulations are discussed in Appendix B.) Widlansky (2007) showed that convective variability in the SPCZ, on synoptic to interannual timescales, is significantly correlated with changes in the Pacific Walker cell and regional Hadley circulation.

Zonal and meridional wind jets also occur at a variety of pressure levels, but are especially prevalent in the lower and upper troposphere where they are the horizontal complements to vertical pressure velocities, thereby acting as the horizontal branches of the overturning circulation cells. The zonal and meridional circulation cells feedback upon the SPCZ, influencing which regions are favorable for convection. Storminess diagonally transects the South Pacific from the northwest to southeast, forcing strong ascent at varying latitudes and longitudes. To examine the structure of overturning circulations and interactions with the SPCZ, zonal and meridional transects of the Pacific troposphere are selected

at distinct latitudes and longitudes.

2.4.1 Walker cell and other zonal overturning circulations

We first explore the large-scale zonal overturning circulations by dividing the South Pacific basin into three latitude bands, each corresponding to the box regions used in Figure 2.2 (equatorial: 7.5°N-7.5°S, tropical: 5°S-20°S, and subtropical: 20°S-35°S) to compare modes of variability within the SPCZ. The SPCZ transects these latitude ranges at different longitudes and we can expect the rising branches of the zonal circulations to occur where convection is strongest.

Zonal mass stream functions (ψ_Z: kg s^{-1}) are calculated using Equation 6 (Hartmann 1994) where the outer integral is taken over the respective latitude range.

$$\psi_Z = \frac{a}{g} \int_{\varphi_S}^{\varphi_N} \int_{0}^{p} \overline{u}^* dp d\varphi \tag{6}$$

Here, $\overline{u}^*$ is the deviation of the DJF mean eastward component of wind from its zonal-mean value, p is atmospheric pressure (1000-100 hPa), a is the mean radius of Earth, and g is the gravitational acceleration. Zonal cross sections of ψ_Z, vertical pressure velocities (-ω: 10^{-2} Pa s^{-1}), and $\overline{U}$ are displayed in Figure 2.10. Each latitude range is sufficient in size to approximately preserve conservation of zonal mass flux. Flow is clockwise, in the longitude-pressure plane, around positive stream functions and zonal gradients are suggestive of rising motion. Positive vertical pressure velocities (red shading) are often observed here, although in some regions this relationship does not hold because convergence of the meridional flow opposes the vertical forcing from zonal wind convergence.

The Walker cell (Julian and Chervin 1978) is clearly apparent in the cross sections of the Pacific, especially at equatorial and tropical latitudes (left column of Figure 2.10a and b, respectively). Here, the mean zonal stream function exceeds 5 x 10^{10} kg s^{-1} near the equator between 180°W-150°W. Rising motion occurs to the west, over the tropical warm pool, and is associated with the equatorial SPCZ. Subsidence is observed to the east of

the SPCZ over the cooler surface waters near the South American coast. Comparison with the OLR climatology (Figure 2.1) shows that maximum rising motion is also collocated with the varying longitudinal location of deep convection. For example, convection and ascent in the equatorial SPCZ are both strongest near 150°E. Further south, convection shifts eastward because of the SPCZ diagonal orientation and the rising branch of the zonal overturning circulation also shifts east (e.g., maximum ascent occurs near 180°W in the tropics and between 150°W-120°W in the subtropics as shown, respectively, in Figure 2.10b and c).

Several interesting characteristics of the zonal wind basic state ($\overline{U}$) are illustrated by longitude-pressure cross sections (Figure 2.10, right column). Considering first the equatorial and tropical latitudes, we note that the westerly duct, or upper branch of the Pacific Walker cell, is located above 400 hPa and at longitudes where subsidence is largest (120°W-90°W). In the lower troposphere, the central Pacific is characterized by easterlies (i.e., the lower branch of the Walker cell), which, especially in the tropics, converge near the SPCZ (150°E-150°W). In the upper troposphere, easterly winds are observed in the West Pacific and the zonal flow is divergent over the tropical SPCZ.

Poleward of 20°S, the sign of the zonal flow is entirely positive above 700 hPa; however, stark longitudinal differences in magnitude are apparent (Figure 2.10c). Previously, we observed that the subtropical jet stream decelerates (i.e., $\partial\overline{U}/\partial x < 0$) in the upper troposphere over the central Pacific (Figure 2.6). Two additional prudent observations are gained by comparing the subtropical cross sections of vertical pressure velocity and zonal wind (Figure 2.10c, left and right columns). Greatest deceleration, or convergence, of the zonal flow occurs at 200 hPa near 150°W and, below this region, strong ascent (2 x 10^{-2} Pa s^{-1}) is evident. The meridional flow must, therefore, be divergent in the upper troposphere for rising motion (i.e., deep convection or low OLR) to be supported in the subtropical SPCZ.

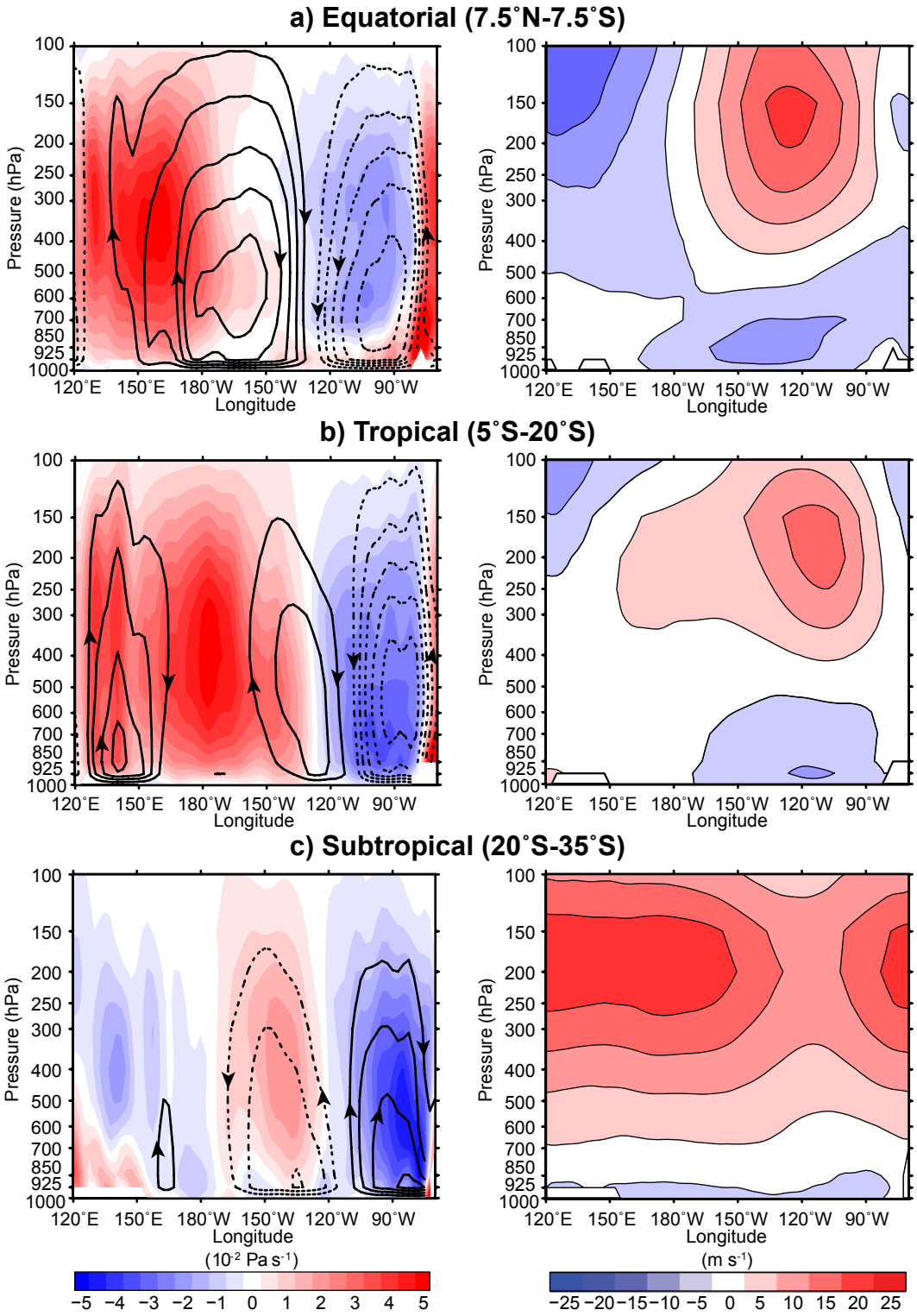

Figure 2.10: Zonal cross sections of mass stream functions (contour interval: 1 x 10^{10} kg s^{-1}; zero contour omitted) and zonal wind (m s^{-1}, shading), left and right columns respectively; for the (a) equatorial (7.5°N-7.5°S), (b) tropical (5°S-20°S), and (c) subtropical (20°S-35°S) Pacific (120°E-70°W). Zonal flow is clockwise around positive stream functions (solid contours). Overlaid on the left column are vertical pressure velocities (-ω shading interval: 5 x 10^{-3} Pa s^{-1}). Positive (negative) values depict rising (sinking) velocity anomalies.

2.4.2 Hadley circulation

We now compare meridional overturning circulations over the western (120°E-165°E), central (180°W-135°W), and eastern (120°W-75°W) Pacific. Numerous studies, summarized by Grimm and Ambrizzi (2009), explored interactions between the Pacific Hadley circulation and Rossby waves in the Southern Hemisphere; often discovering teleconnections between the tropics and higher latitudes on a variety of space and temporal scales. As noted previously, the SPCZ transects the Pacific diagonally. Maximum convection is located at different latitudes in each longitude range. We can, therefore, expect rising branches of meridional circulations to occur at latitudes (i.e., equatorial, tropical, or subtropical) where convection is strongest for the respective longitude band.

The range of each cross section is defined to be 45° longitude to approximately conserve mass flux within the meridional bands. Strength of meridional circulations can, therefore, be estimated by gradients of meridional mass stream functions (ψ_M: kg s^{-1}):

$$\psi_M = \frac{2\pi a \cos\varphi}{g} \int_0^p [v]\, dp \tag{7}$$

where φ is the latitude range (20°N-50°S) and $[v]$ is the zonal average of the meridional mean wind ($\overline{V}$) for the respective longitude cross sections (i.e., western, central, and eastern Pacific). Other terms are as defined by Equation 6, again following Hartmann (1994). Each region is separated by 15° longitude, limiting mass flux leakage from one section to another and allowing comparison to be made between different Pacific regions.

Meridional cross sections of ψ_M, -ω, and $\overline{V}$ are displayed in Figure 2.11. Flow is clockwise, in the latitude-pressure plane, around positive stream functions and meridional gradients are suggestive of rising motion. Strength of meridional circulations, in most regions (e.g., central Pacific: 5 x 10^{11} kg s^{-1}), are an order of magnitude larger than the equatorial Walker cell (5 x 10^{10} kg s^{-1}). As with the previous zonal circulation analysis, positive vertical pressure velocities (red shading) are often collocated with horizontal gradients of the

stream function; although in some regions the relationship does not hold because convergence of the zonal flow (Figure 2.10) opposes the meridional forcing component of rising motion. For example, while strong Hadley cells are evident in both hemispheres of the eastern Pacific (Figure 2.11c), the region is in the subsiding branch of the Walker circulation and negative pressure velocities (blue shading) are evident throughout most of the Southeast Pacific (120°W-75°W).

Further west, in regions more directly forced by the SPCZ (Figure 2.11a and b), rising motions (exceeding 5 x 10^{-2} Pa s^{-1}) are evident where convection is strongest (western Pacific: 10°N-15°S; central Pacific: 5°S-25°S). Locations of the rising branches of the overturning circulations closely match the diagonal orientation of deep convection enclosed by the OLR 240 W m^{-2} contours in Figure 2.1. In the West Pacific, the meridional circulation is mostly thermally direct with the rising branch of the Northern Hemisphere Hadley cell above the warmest surface waters near the equator. The stream function analysis shows thermally indirect circulations over the central Pacific. For example, rising motion occurs away from the equator, in the subtropical SPCZ, where convection is strongest. Northerly winds are convergent in the low-levels and reverse in the upper troposphere. Subsidence occurs over warm waters near the equator, completing the Southern Hemisphere circulation cell. (See Appendix B for further comparison of thermally direct and indirect overturning circulations.)

2.4.3 Subtropical zonal jet stream and vertical wind shear

In Chapter 2.2, we discussed the horizontal structure of the 200 hPa zonal wind maximum. The jet originates near Australia and decelerates over the central Pacific, accounting for a region of $\partial\overline{U}\big/\partial x < 0$ in the subtropical SPCZ. Here, we examine vertical cross sections of $\overline{U}$ in a manner similar to the previous section (Figure 2.10), except that a latitudinal transect is now made for the western, central, and eastern Pacific (Figure 2.11, right column). Circulating from west to east at the 200 hPa level, strong westerlies (i.e., the jet maximum

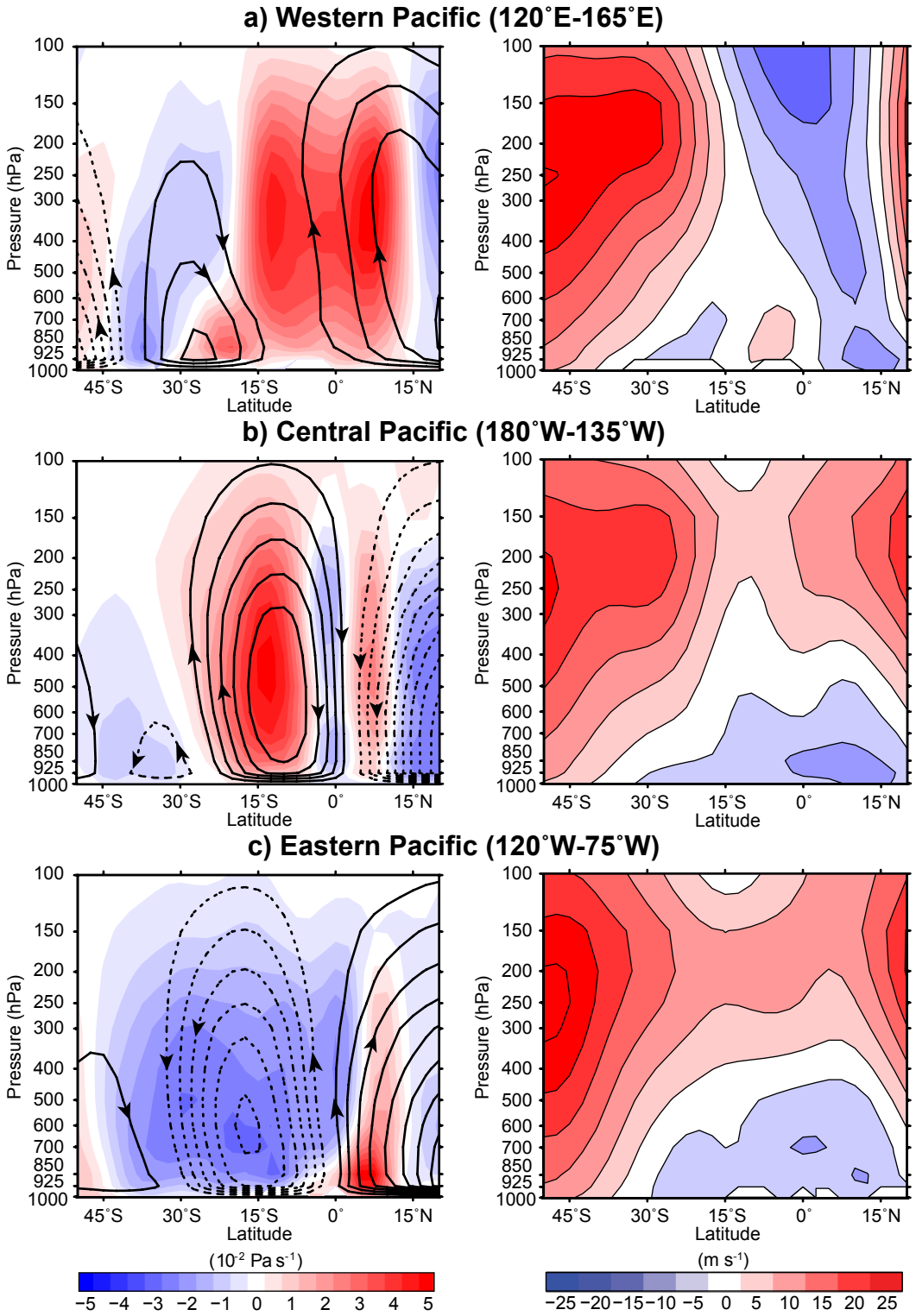

Figure 2.11: Same as Figure 2.10 except for meridional cross sections of mass stream functions (contour interval: 1 x 10^{11} kg s^{-1}; zero contour omitted; left column), vertical pressure velocities (-ω shading interval: 5 x 10^{-3} Pa s^{-1}; left column), and zonal wind (right column). Meridional flow is clockwise around positive stream functions (solid contours). Averaging regions are (a) "Western Pacific" (120°E-165°E), (b) "Central Pacific" (180°W-135°W), and (c) "Eastern Pacific" (120°W-75°W).

which exceeds 20 m s^{-1}) become increasingly confined to higher latitudes. Weaker westerlies (5-10 m s^{-1}) are observed at all other latitudes in the upper troposphere, except in the western Pacific where equatorial easterlies (-15 m s^{-1}) are found. Elsewhere, easterly winds are only observed in the lower troposphere.

Vertical zonal wind shear ($\partial\overline{U}/\partial z$) is observed in each longitude region and throughout most latitudes. Shear is greatest where strong westerlies extend far into the subtropics, such as in the western Pacific. In that region especially, the jet stream supplies baroclinic energy for intensifying cyclonic disturbances. $\partial\overline{U}/\partial z$ decreases further east as the jet stream weakens and bends poleward, south of the SPCZ. Eastin and Vincent (1998) postulated that divergent outflow in the meridional direction, produced by strong equatorial convection in the West Pacific, curves southeastward due to the Earth's rotation, enhancing the subtropical jet stream and vertical shear near the diagonal SPCZ. In the central Pacific, convection occurs in the subtropics and equatorward meridional winds are observed (Figures 2.5b and 2.11b, left column). Outflow from the diagonal cloud band could, therefore, limit intensification of upper troposphere westerlies and force the subtropical jet stream to veer southward and become more parallel to the SPCZ.

2.5 Storm tracks from the mid-latitudes

Convection in the SPCZ varies on a wide range of modes. OLR slowly oscillates in the tropics while the subtropical diagonal cloud band is more heavily influenced by higher frequency modes, as discussed in Chapter 2.1. However, a question remains concerning what influences variability on synoptic timescales of less than 8 days. Noting that the basic zonal flow (Figure 2.6) consists of a subtropical jet stream, extending from Australia into the SPCZ, and also a region of westerly winds linking the Northern Hemisphere kinematically with the South Pacific (Webster and Holton 1982; Tomas and Webster 1994; Duane et al. 1999), we now measure mean disturbance activity as a way to explore storm tracks which may influence the SPCZ.

Disturbance activity is measured by computing the eddy perturbation kinetic energy (PKE) from the 200 hPa zonal (u') and meridional (v') wind deviations from climatology (following e.g., Arkin and Webster 1985; Webster and Yang 1989; Matthews and Kiladis 1999):

$$PKE = \frac{1}{2}\left(\overline{u'^2 + v'^2}\right) \tag{8}$$

The PKE climatology (Figure 2.12) consists of a maxima extending from south of Australia towards the subtropical SPCZ and in the central Pacific well north of the equator. PKE exceeds 160 m^2 s^{-2} near the subtropical jet stream and decreases to less than 100 m^2 s^{-2} over regions of the East Pacific. Further north, some disturbance activity (exceeding 100 m^2 s^{-2}) clearly extends from the Northern Hemisphere, through the westerly wind duct, and into the equatorial region of the central Pacific as noted by Arkin and Webster (1985) and discussed by Webster and Yang (1989). However, no clear linkage between Northern Hemisphere disturbance activity and the SPCZ can be infered from either Figure 2.12 or a literature review.

Synoptic disturbance activity in the diagonal SPCZ seems to, instead, originate in the mid-latitudes south of Australia where PKE is large (Streten 1973; Streten and Zillman 1984; Kiladis et al. 1989; Trenberth 1991). In Chapter 5, we explore how disturbance activity propagates into the SPCZ. Interestingly, widespread convection (as inferred by OLR values less than 240 W m^{-2}) is not observed in the subtropics near where the disturbances originate, but rather is concentrated further east in a diagonal band near where the subtropical jet stream weakens (Figure 2.6). Objectives for the remainder of this study are to first determine what forces a decelerating zonal flow over the South Pacific and then examine why this region of negative stretching deformation is conducive for the accumulation of disturbances which results in enhanced convection near the SPCZ.

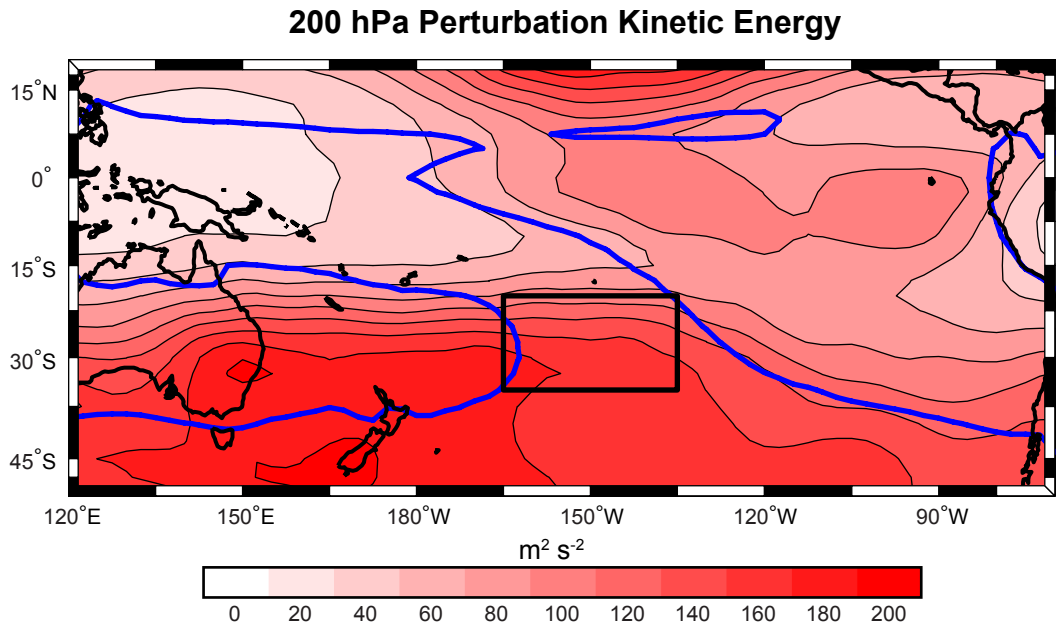

Figure 2.12: DJF climatology (1982-2008) of 200 hPa PKE (20 m^2 s^{-2} shading interval). Large black box located at 20°S-35°S, 165°W-135°W represents the averaging region for calculating OLR and stretching deformation time series. 240 W m^{-2} OLR contour outlined by blue lines.

CHAPTER III

SIMULATED CLIMATOLOGY OF THE SPCZ

Uncertainty of which factors most determine the background basic state of the Southern Hemisphere motivates analysis of how well numerical models simulate the diagonal cloud band and long wave circulation pattern. Goals of this chapter are to explore the "predictability" of the SPCZ on long time scales, in both an ocean-atmosphere coupled and uncoupled model, and to provide a robust climatology for comparison with controlled numerical experiments in later chapters. We first examine the South Pacific climatology depicted by the Geophysical Fluid Dynamics Laboratory (GFDL) global coupled model (CM2.1). The simulation was conducted at NOAA's GFDL and forced by observed radiation parameters from the 20th century ("20C3M" experiment described in detail by Delworth et al. 2006). Wittenberg et al. (2006) provides an evaluation of the GFDL performance at simulating the tropical Pacific climate, but their study does not extensively explore how the SPCZ is depicted. To answer this question, we have made a comparison to an ensemble of 10 control simulations using an uncoupled coarse resolution atmospheric general circulation model (AGCM) provided by the International Centre for Theoretical Physics (ICTP). Descriptions of both models are provided in the Appendix (GFDL CM2.1: C.1, ICTP AGCM: C.2).

Following the methodology utilized in the previous chapter, where the observed South Pacific climate is depicted, we examine the region enclosed by 20°N-50°S and 120°E-70°W in each model domain. Emphasis is applied to examining how simulations of the SPCZ are related to boundary forcing mechanisms and large scale circulations. For each model, the seasonal cycle of OLR is first shown and comparison is made between the ensemble mean and individual simulations. Next, significant modes of convective variability are examined.

We then discuss the SPCZ in the context of the lower and upper tropospheric basic state circulation. Comparisons between different surface boundary temperature forcings, model depictions of the SPCZ, and the observed climatology are finally provided.

3.1 Coupled general circulation model

The GFDL CM2.1 well simulates many features of the South Pacific climate, including the SPCZ. CM2.1 is chosen because, compared to CM2.0, SPCZ precipitation is in better agreement with observations (Wittenberg et al. 2006); although rainfall in the tropical West Pacific is still too high. For consistency with the observational analysis in Chapter 2, simulated OLR is used as a proxy of deep convection and precipitation. Figure 3.1a and b provides a comparison of DJF and JJA seasonal mean OLR for the later portion of the 20^{th} century (1982-2000) control experiment (CM2.1, henceforth referred to as the GFDL model, simulation, or experiment). The ensemble average of five runs is shown in the left column. We clearly see a diagonal band of simulated deep convection, representative of the SPCZ, especially during DJF.

Several subtle discrepancies do exist; however, between the observed SPCZ location (Figure 2.1) and simulated convection. During DJF, the GFDL model depicts the SPCZ separating from the ITCZ near New Guinea, which is further west than where the observed cloud band veers poleward around the Dateline. In the subtropics, convection is oriented diagonally away from the equator, but the area enclosed by the 240 W m^{-2} OLR contour is narrower than observed. The JJA simulated SPCZ is also shifted more to the west, but correctly shows no poleward diagonal cloud band. Connection with the mid-latitude storm track is only evident during summer months (DJF).

Perhaps the most pronounced bias in the GFDL experiment is the tendency to simulate two horizontal bands of tropical convection, one in each hemisphere, during DJF (Figure 3.1a). Numerous studies (e.g., Latif et al. 2001; AchutaRao and Sperber 2002; Davey et al. 2002) have explored the ("double") ITCZ bias located south of the equator in many

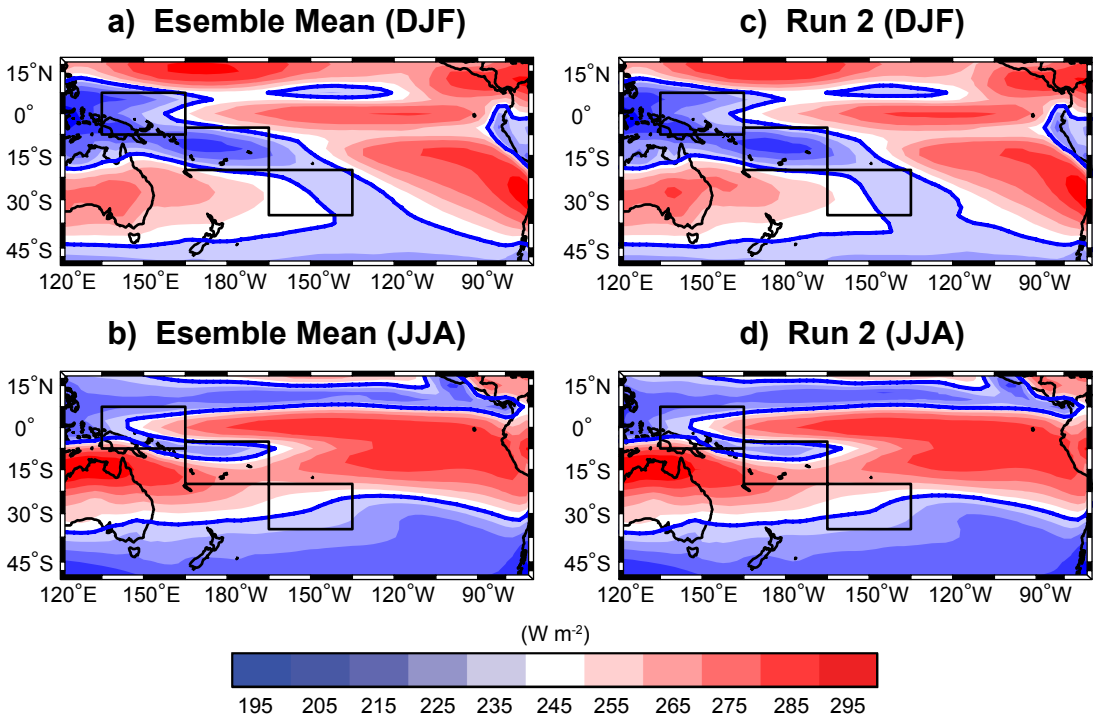

Figure 3.1: GFDL climatology of OLR (W m^{-2}) for DJF and JJA (top and bottom rows, respectively). Ensemble mean and run two are shown (left and right columns, respectively) for the period 1982-2000. Black boxes represent the "Equatorial" (7.5°N-7.5°S, 135°E-165°E), "Tropical" (5°S-20°S, 165°E-165°W), and "Subtropical" (20°S-35°S, 165°W-135°W) SPCZ regions referred to in Chapter 2. 240 W m^{-2} OLR contour outlined by blue lines.

climate simulations. While some coupled GCMs depict a South Pacific cloud band oriented almost completely parallel to the ITCZ (Lin 2007), the GFDL model does simulate a diagonal cloud band; however, an incorrect horizontal OLR minimum (< 260 W m^{-2}) still exists in the Southeast Pacific. Wittenberg et al. (2006), in an analysis of the tropical Pacific climate and ENSO variability in the GFDL model, noted that this anomalous horizontal convective band may be forced by the temperature gradient between a cold SST bias along the equator in the East Pacific and a warm bias to the south. They further note that the distribution of SST anomalies is skewed towards warm ENSO events in most, but not all, of the five GFDL runs and perhaps explains some of the enhanced convection in the tropical Southeast Pacific.

Each ensemble member possesses a unique frequency and intensity of ENSO variability which forces subtle differences in the mean SPCZ. Peak inter-ensemble standard deviations of OLR (Figure 3.2) are in the western and central tropical Pacific (> 15 W m^{-2}). In these regions, variability between ensemble members appears to mostly be determined by the different frequency and amplitude of ENSO events in each simulation (Wittenberg et al. 2006). High variance between ensemble members extends poleward in two clusters, east and west of the mean SPCZ position (i.e., outside of the gray contours in Figure 3.2).

We now compare the OLR seasonal climatology from only run two of the ensemble suite (Figure 3.1 right column) with the average from all five runs (left column). Run two is chosen for comparison because daily average model output is available for the period 1992-2000, which will be used subsequently to examine modes of SPCZ variability on timescales shorter than the seasonal cycle. Run two simulates a diagonal band of low OLR during DJF which is almost identical to the ensemble average SPCZ in the tropics, but slightly wider in longitudinal scope throughout the subtropics. Elsewhere during DJF, run two shows a double ITCZ bias in the East Pacific, similar to the ensemble mean, which also mostly disappears during JJA. From Figure 3.1, we verify that in run two there is a seasonal cycle of the SPCZ location and orientation similar to the other ensembles. Due

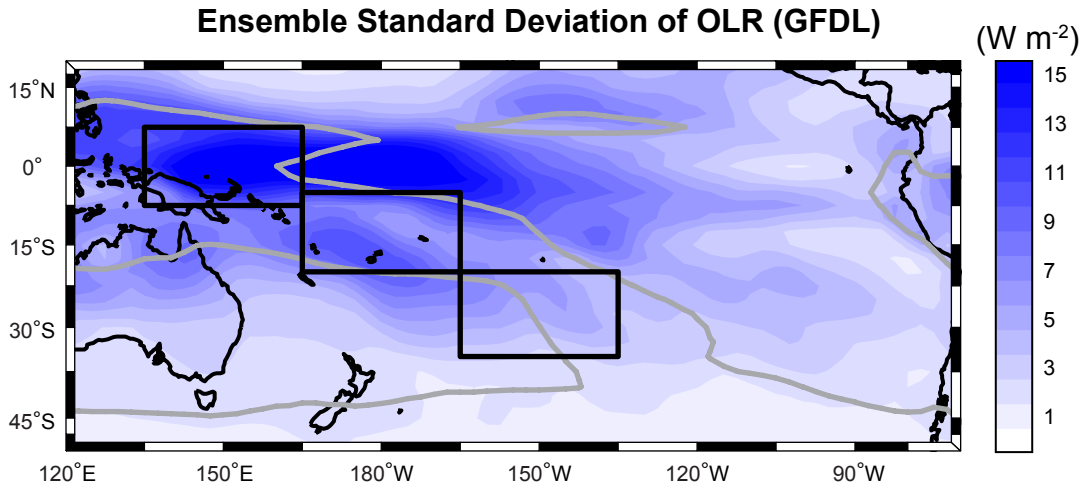

Figure 3.2: Standard deviation between GFDL ensembles of seasonal average OLR (W m^{-2}) for the DJF period (1982-2000). Black boxes represent the "Equatorial" (7.5°N-7.5°S, 135°E-165°E), "Tropical" (5°S-20°S, 165°E-165°W), and "Subtropical" (20°S-35°S, 165°W-135°W) SPCZ regions referred to in Chapter 2. 240 W m^{-2} OLR contour outlined by gray lines.

to the correspondence of the SPCZ spatial and seasonal features in both run two and the ensemble average, the climate simulation of run two is considered representative of the GFDL CM2.1 experiment for purposes of studying the SPCZ.

The standard deviation of daily OLR anomalies (NDJFM) from run two (Figure 3.3a) is similar to the observed variability (Figure 2.2a) over most of the Pacific basin. Throughout the simulated SPCZ (enclosed by the 240 W m^{-2} mean OLR contours) the standard deviation exceeds 35 W m^{-2}, which is about equivalent to the observed magnitude. However, in the Southeast Pacific, a notable difference between simulated OLR variability and observations is evident. The GFDL model overly excites convective variability in a horizontal band collocated with the double ITCZ anomaly seen in Figure 3.1. How coupled model convection errors in the East Pacific influence the SPCZ remains uncertain (Ganachaud et al. 2007), but answers to this question are beyond the scope of this study.

Here, we limit discussion to the simulated modes of variability for the equatorial, tropical, and subtropical SPCZ regions (Figure 3.3b-d, respectively). We use NDJFM daily

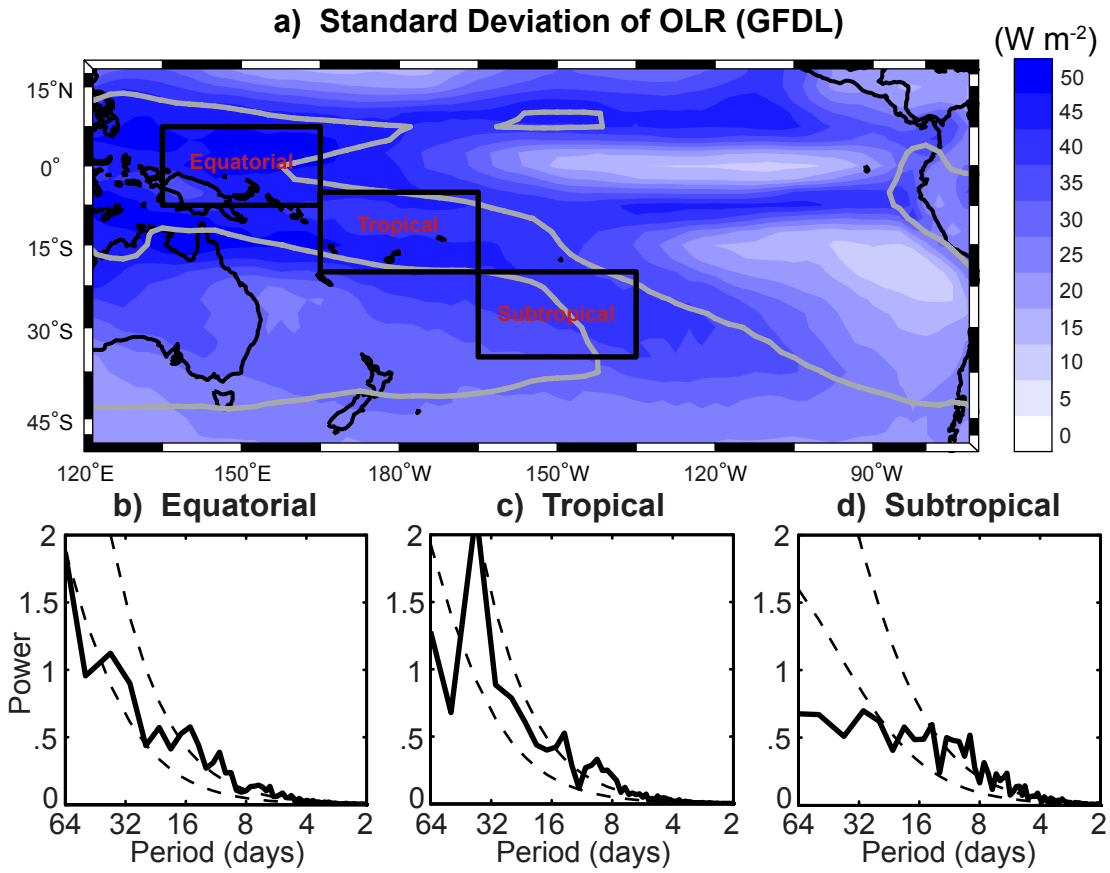

Figure 3.3: GFDL run two: (a) Standard deviation of daily OLR anomalies (W m^{-2}) for NDJFM (1992-2000). 240 W m^{-2} OLR contour outlined by gray lines. Black boxes represent the "Equatorial" (7.5°N-7.5°S, 135°E-165°E), "Tropical" (5°S-20°S, 165°E-165°W), and "Subtropical" (20°S-35°S, 165°W-135°W) averaging regions for calculating OLR time series. (b, c, and d) Average Fourier power spectra of OLR in the equatorial, tropical, and subtropical regions of the SPCZ, respectively. Lower dashed lines are the red-noise spectra for mean lag-1 autocorrelations of 0.95 (b), 0.83 (c), and 0.79 (d). Upper dashed lines are the 95% confidence spectra.

OLR anomalies (available for run two from 1992-2000) to provide 9 seasonal time series. The extended austral summer season is again used for the spectra calculations. Red-noise spectra (lower-dashed lines) for mean lag-1 autocorrelations of 0.95 (b), 0.83 (c), and 0.79 (d) along with the corresponding 95% confidence spectra (upper-dashed lines) are calculated following the Torrence and Compo (1998) methodology utilized in Chapter 2.1. In all SPCZ regions, OLR variability is slightly more "red" (i.e., larger autocorrelations) in the GFDL simulation than calculated from satellite data (equatorial: 0.90, tropical: 0.78, subtropical: 0.70), suggesting slower varying convection in the model.

In the equatorial SPCZ, a variability peak around 2 weeks exceeds the 95% confidence threshold and is similar to observations, but the GFDL model does not simulate significant intraseasonal variability (Figure 3.3b). However, GFDL variability does peak between 30-50 days in the tropical region (c), suggesting that a portion of the SPCZ oscillates on intraseasonal timescales in the model. Also noted in the tropics are a 2 week spectral peak and convective oscillations on synoptic timescales of less than 8 days. Each of these modes is similar to variability detected in observations. Poleward of 20°S (d), the power spectra of simulated convection is strikingly similar to observations, showing significant variability mostly constrained to synoptic frequencies less than 2 weeks.

The GFDL CM2.1 experiment simulates a basic state circulation that is also similar to observations. Figure 3.4a and b displays, respectively, the 850 hPa and 200 hPa geopotential height (Φ) and wind ($\overline{U}$ and $\overline{V}$) from the GFDL model. A comparison with the observed lower troposphere basic state (Figure 2.5a) yields several subtle differences. At the 850 hPa level, the simulated West Pacific equatorial trough is deeper, while the East Pacific high is slightly weaker than observed. In the tropical Pacific, easterly trade winds are too strong and extend too far west as previously noted by Wittenberg et al. (2006). Interestingly, deep convection of the equatorial SPCZ is also shifted west, compared to observations.

Similar to the observed basic state, the height of the 200 hPa wind field in the GFDL model (Figure 3.4b) parallels the SST distribution with greater heights occurring over

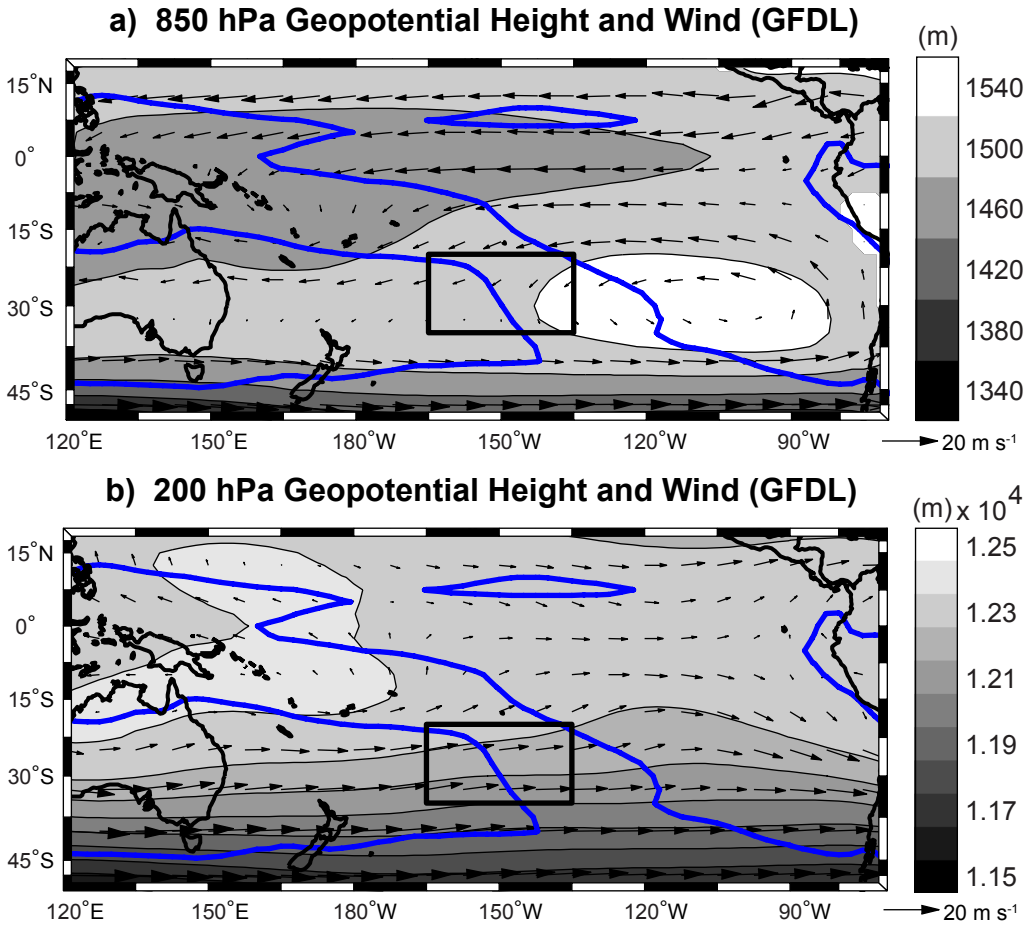

Figure 3.4: GFDL run two: DJF climatology (1982-2000) of (a) 850 hPa geopotential height (m, shading) and winds (m s^{-1}, vectors) and (b) 200 hPa geopotential height and winds. Large black box ("A": located at 20°S-35°S, 165°W-135°W) described in Chapter 2. 240 W m^{-2} OLR contour outlined by blue lines.

warm SSTs and lower heights over cooler waters. Meridional geopotential height gradients ($\partial\Phi/\partial y$) are greatest over the western and eastern parts of the Pacific basin, away from the equator, and smaller elsewhere. The simulated gradient pattern is consistent with the observed location of the subtropical jet stream maxima south of Australia and near South America.

Figure 3.5 confirms that the GFDL model simulates realistic 200 hPa westerly wind maxima in two regions of the subtropics: south of Australia (35 m s^{-1}) and in the extreme Southeast Pacific (25 m s^{-1}). Between these two jet stream maxima is the SPCZ (black box), where zonal winds decelerate to less than 20 m s^{-1}. Equatorward of the SPCZ, westerly winds bridge the South Pacific with the Northern Hemisphere, but are weaker than observed. Closer to the subtropical SPCZ, superimposed contours of negative zonal stretching deformation ($\partial\overline{U}\big/\partial x < 0$) are collocated with the deepest convection (OLR < 240 W m^{-2}). We saw from Figure 3.1 that the simulated SPCZ is narrower than observed and also shifted east in the subtropics. A similar $\partial\overline{U}\big/\partial x < 0$ pattern is evident in the GFDL model. The zonal stretching deformation minimum ($\partial\overline{U}\big/\partial x \approx -2.5 \times 10^{-6} s^{-1}$) is near the eastern border of the SPCZ; however, the magnitude is about 30% smaller than observed. Near the western border of Box A, the region of negative zonal stretching deformation is even more reduced. Here, simulated convection is also suppressed. Most notable about the GFDL simulation of the South Pacific climate is that, while subtle biases are evident, there remains a strong collocation between $\partial\overline{U}\big/\partial x < 0$ and the location of the diagonal cloud band.

3.2 Atmospheric general circulation model

We now explore how a coarse global climate model (ICTP AGCM), which is uncoupled with the ocean, simulates the basic state circulation and the SPCZ. Resolution is defined by eight vertical levels and total wavenumber 30. The model is forced by a fixed annual cycle of monthly climatological SSTs and land boundary conditions. Data are from the

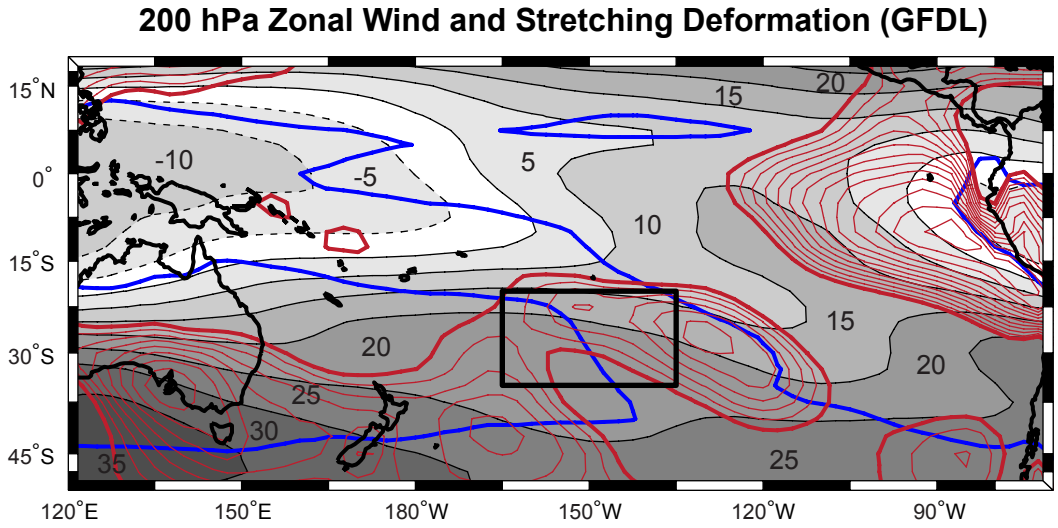

Figure 3.5: GFDL run two: DJF climatology (1982-2000) of 200 hPa zonal winds (5 m s^{-1} shading interval, dashed lines depict negative zonal winds, zero contour omitted) and negative zonal stretching deformation (s^{-1}, red contours). Zonal stretching deformation contour interval: -5x10^{-7} s^{-1}; thick lines depict the zero contour. 240 W m^{-2} OLR contour and box "A" outlined by blue and black lines, respectively.

European Centre for Medium-Range Weather Forecasts' (ECMWF) reanalysis (ERA15: Gibson et al. 1997) and averaged over the 1981-1990 period to achieve a balance between warm and cold ENSO events in the SST field. For this "Control" experiment, 10 ensemble runs of the ICTP AGCM are each integrated for 26 years. The first two years of integration are discarded, as discussed in Appendix C.2, to allow for sufficient climate spin up from an atmosphere at rest. Independency between runs is achieved by initially forcing each ensemble member with random radiation parameters using the methods described by Kucharski et al. (2006). 10 independent samples of the Control experiment describe the model response to a prescribed annual cycle of SST.

Figure 3.6 shows the OLR seasonal climatology simulated by the ICTP ensemble average (left column) for DJF and JJA (a and b, respectively). A pronounced seasonal cycle of convection is clearly apparent, with the simulated diagonal cloud band most established during DJF. Comparison of Figure 3.6 with observed OLR (Figure 2.1) indicates that the AGCM simulates a diagonal band of convection similar in location and intensity to the

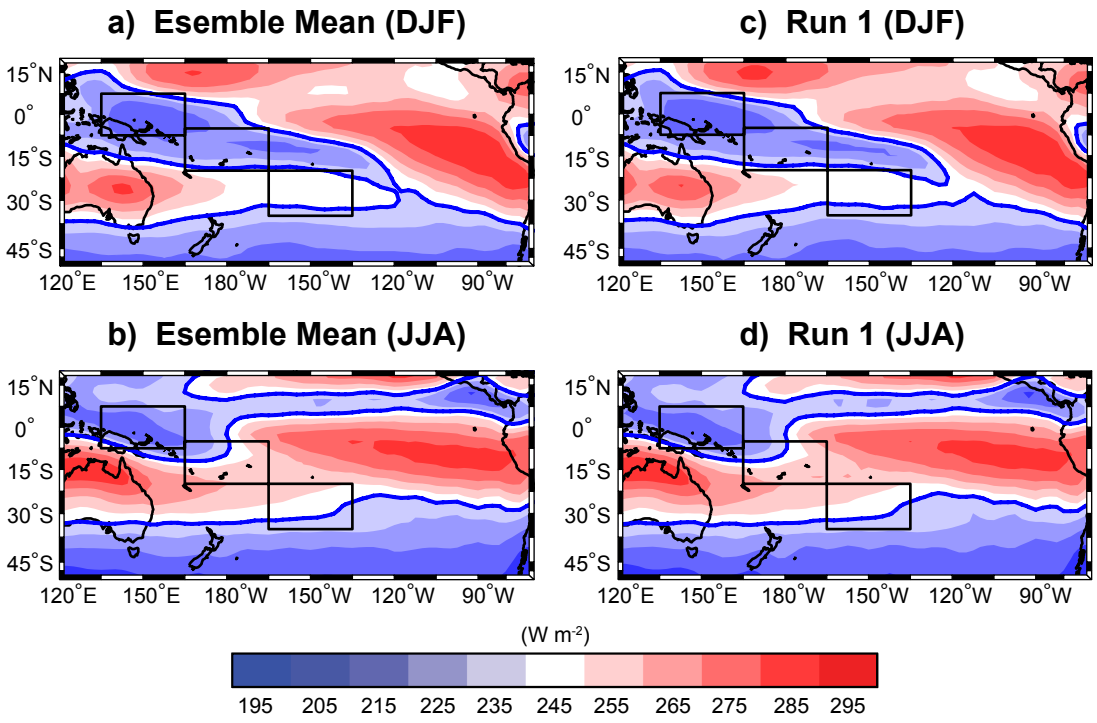

Figure 3.6: ICTP climatology of OLR (W m^{-2}) for 24 DJF and JJA seasons (top and bottom rows, respectively). Ensemble mean and run one are shown (left and right columns, respectively). Black boxes represent the "Equatorial" (7.5°N-7.5°S, 135°E-165°E), "Tropical" (5°S-20°S, 165°E-165°W), and "Subtropical" (20°S-35°S, 165°W-135°W) SPCZ regions referred to in Chapter 2. 240 W m^{-2} OLR contour outlined by blue lines.

observed SPCZ, although the model cloud band is more zonally oriented and shifted east in the subtropics. Lin (2007) also finds a zonal bias of the SPCZ in an analysis of 22 coupled GCMs (including the GFDL model); however, complex coupled models often depict a South Pacific cloud band oriented almost parallel to the ITCZ. In this uncoupled Control experiment, the AGCM simulates deep convection in the tropical SPCZ, but OLR values are higher than observed in most of the subtropics. Elsewhere, the simplified model simulates a weaker ITCZ, especially during DJF when convection is even more sporadic than observed over the equatorial central Pacific. Unlike the GFDL experiment, no double ITCZ problem is apparent in the uncoupled simulation.

The climatology from one arbitrarily chosen run is compared to the ensemble mean by examining the right and left columns of Figure 3.6, respectively. Similar patterns in the

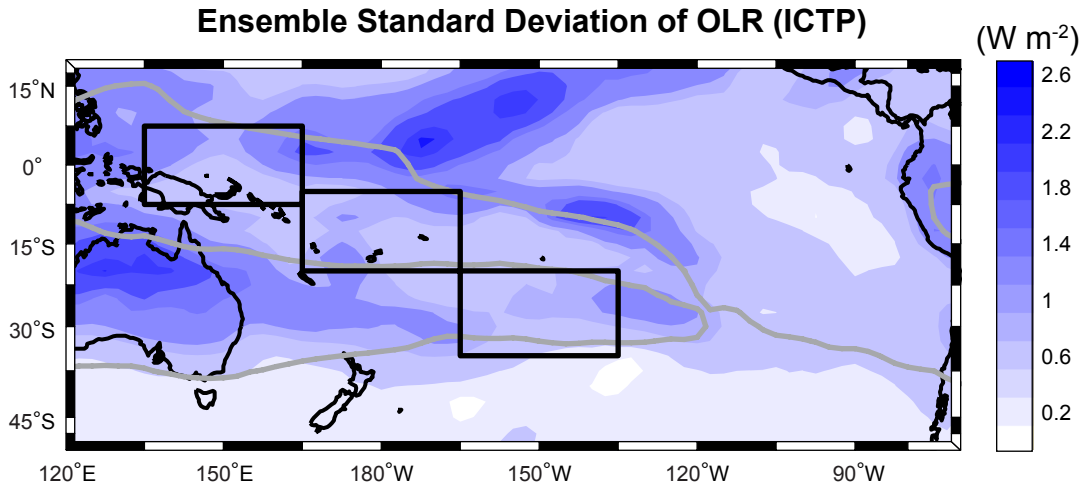

Figure 3.7: Standard deviation between ICTP ensembles of seasonal average OLR (W m^{-2}) for 24 DJF seasons. Black boxes represent the "Equatorial" (7.5°N-7.5°S, 135°E-165°E), "Tropical" (5°S-20°S, 165°E-165°W), and "Subtropical" (20°S-35°S, 165°W-135°W) SPCZ regions referred to in Chapter 2. 240 W m^{-2} OLR contour outlined by gray lines.

OLR fields are noted, although run one simulates slightly weaker convection in the subtropical SPCZ compared to the ensemble average. Several interesting observations of how the ITCP model varies between runs is made by looking at the inter-ensemble standard deviation (Figure 3.7). In general, there is low variability between ICTP runs with standard deviations being about an order of magnitude smaller than for the GFDL ensemble (Figure 3.2), although here we are comparing ensembles of different sizes (ICTP: 10 runs, GFDL: 5 runs). Ensemble variability is especially small in the higher latitudes (typically low OLR), Southeast Pacific (higher OLR), and throughout most of the tropical SPCZ. In these regions, cloud cover characteristics are mostly constant for the entire ensemble during DJF. Larger variability between runs occurs in the equatorial central Pacific and over Australia, although there are also variance peaks along the western and eastern boundaries of the SPCZ, and in the subtropics where the cloud band is most diagonal (20°S-35°S, 135°W-120°W). Here, the frequency of convection varies slightly between different members of the ICTP ensemble.

Only run one is analyzed further because both its mean OLR (Figure 3.6) and basic state circulation (examined subsequently) are similar to the ensemble average. The standard deviation of daily OLR anomalies is shown in Figure 3.8, along with a comparison of power spectra from different SPCZ regions. As was done for the analyses of observations and the GFDL simulation, the annual cycle has been removed from the OLR data and only the ND-JFM period is retained to provide a time series of sufficient length for examining variability on intraseasonal and shorter timescales. Maximum variability of convection is observed over Australia and along the borders of the mean SPCZ, although the standard deviations in Figure 3.8a are smaller than both observed by satellites (Figure 2.2a) or simulated by the GFDL model (Figure 3.3a). A portion of the lower standard deviations in the tropical SPCZ is attributed to the lack of intraseasonal variability simulated by the uncoupled ICTP model (Figure 3.8b and c). In the equatorial and tropical SPCZ, lag-1 autocorrelations of simulated OLR time series (equatorial: 0.74 and tropical: 0.65) are lower than observed (equatorial: 0.90 and tropical: 0.78) and no spectral peaks between 30-60 days are noted. Significant variability is constrained to timescales shorter than 2 weeks for all regions of the SPCZ in the uncoupled simulation. In the subtropical SPCZ, the model power spectra (Figure 3.8d) is nearly identical to observations and autocorrelations are also more similar.

Coarse model resolution of topography (3.75° latitude-longitude grid) may account for some of the basic state circulation biases evident by comparison of Figure 3.9 with the observed winds and geopotential heights in the lower and upper troposphere (Figure 2.5). Previous studies have linked model resolution of the Andes to simulations of the East Pacific subtropical high (Rodwell and Hoskins 2001) and formation of the SPCZ to the west (Takahashi and Battisti 2007b). In the Southeast Pacific, the surface high simulated by the ICTP model is weaker than observed and 850 hPa heights are slightly lower. The simulated high pressure circulation is also less longitudinally constrained than the East Pacific high depicted in the NCEP reanalysis. In the AGCM, positive height anomalies at 850 hPa extend westward through the simulated SPCZ diagonal branch. Equatorward of these

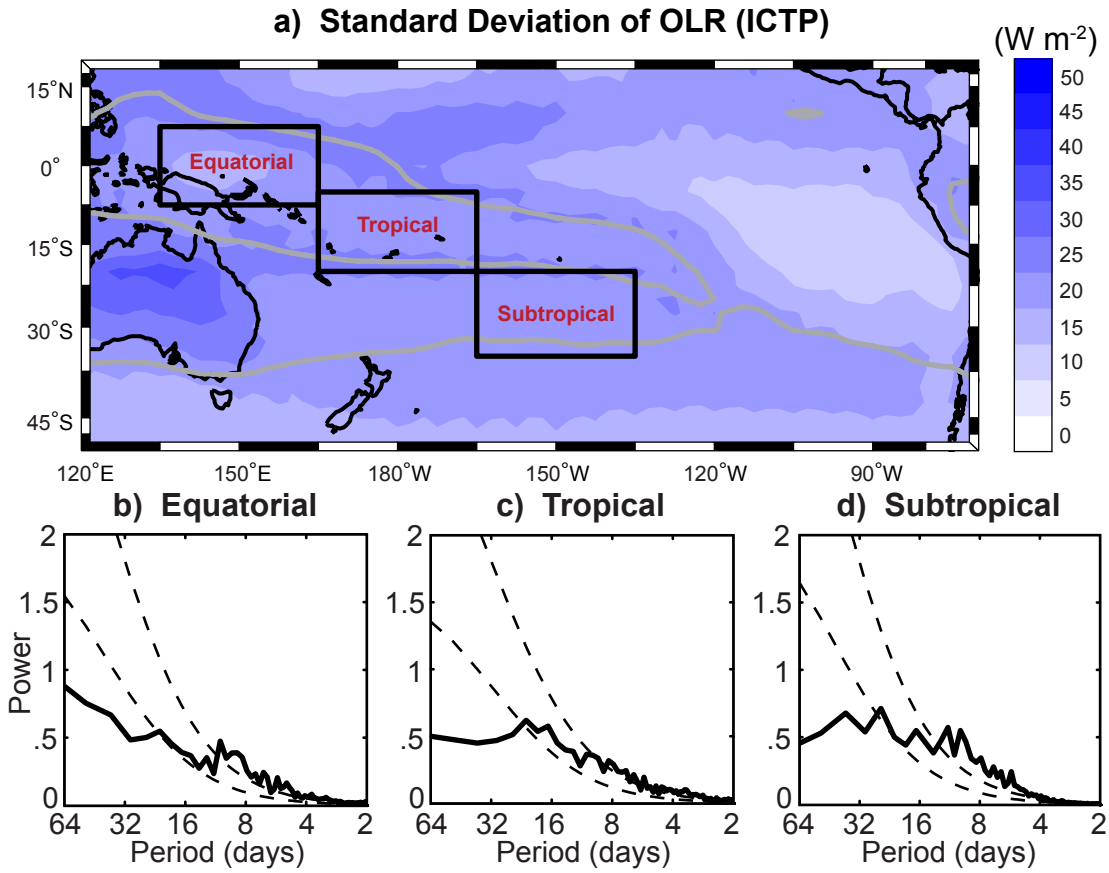

Figure 3.8: ICTP run one: (a) Standard deviation of daily OLR anomalies (W m^{-2}) for NDJFM (24 seasons). 240 W m^{-2} OLR contour outlined by gray lines. Black boxes represent the "Equatorial" (7.5°N-7.5°S, 135°E-165°E), "Tropical" (5°S-20°S, 165°E-165°W), and "Subtropical" (20°S-35°S, 165°W-135°W) averaging regions for calculating OLR time series. (b, c, and d) Average Fourier power spectra of OLR in the equatorial, tropical, and subtropical regions of the SPCZ, respectively. Lower dashed lines are the red-noise spectra for mean lag-1 autocorrelations of 0.74 (b), 0.65 (c), and 0.77 (d). Upper dashed lines are the 95% confidence spectra.

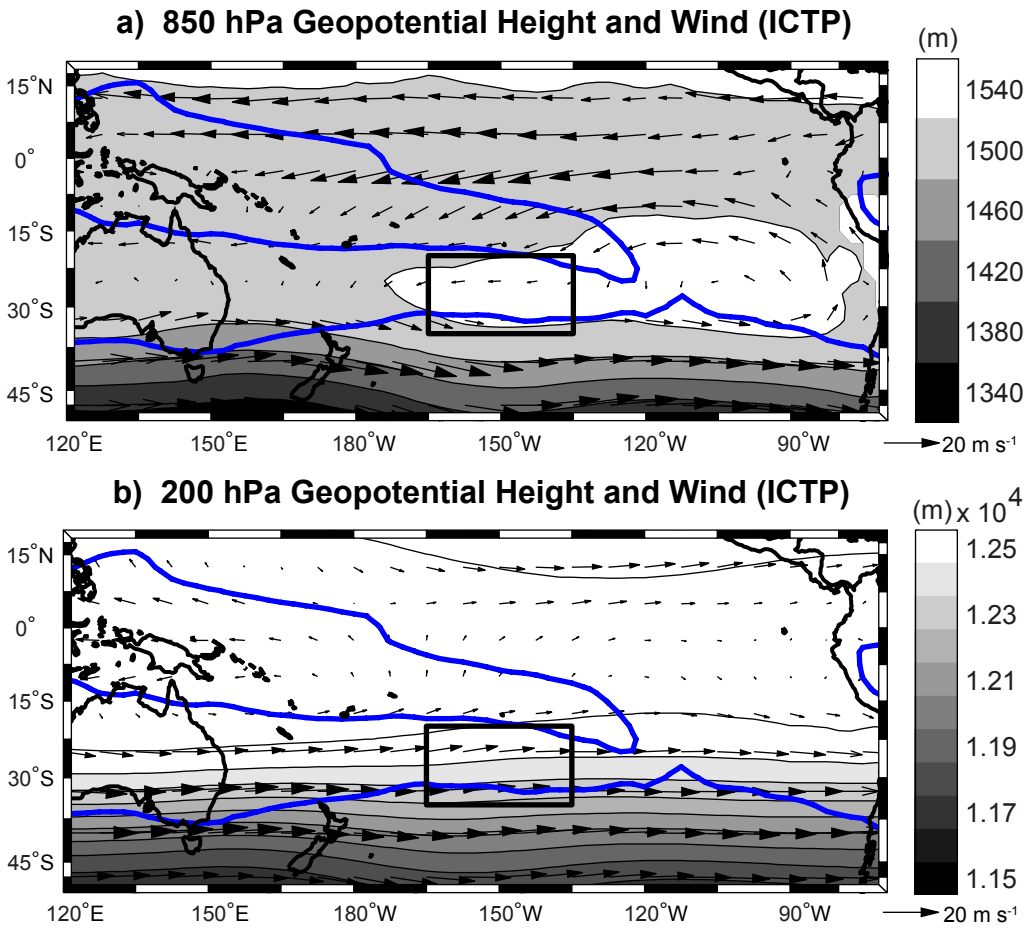

Figure 3.9: ICTP run one: DJF climatology (24 seasons) of (a) 850 hPa geopotential height (m, shading) and winds (m s^{-1}, vectors) and (b) 200 hPa geopotential height and winds. Large black box ("A": located at 20°S-35°S, 165°W-135°W) described in Chapter 2. 240 W m^{-2} OLR contour outlined by blue lines.

anomalies are trade winds which also extend too far west. In the upper troposphere, the meridional height gradient is anomalously strong at all longitudes and shifted equatorward. There is also less cyclonic rotation in the East Pacific at 200 hPa.

Geopotential height biases are reflected in the 200 hPa zonal wind and stretching deformation fields (Figure 3.10). The AGCM simulates a 200 hPa westerly wind maximum between 30°S-50°S and easterlies over the West Pacific warm pool but with some biases. The Control climatology possesses a westerly duct in the central equatorial Pacific, although the winds are weaker than both observations and the GFDL simulation. There is

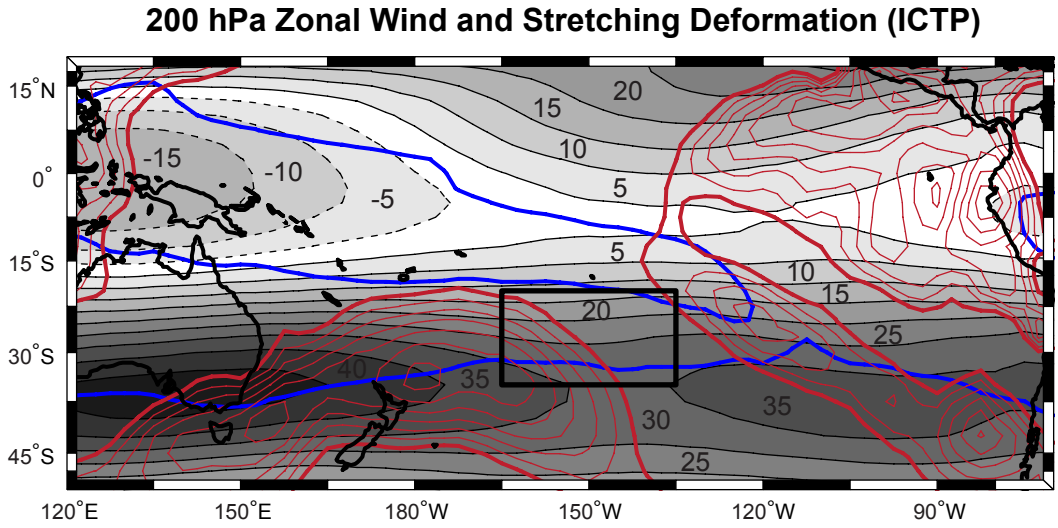

Figure 3.10: ICTP run one: DJF climatology (24 seasons) of 200 hPa zonal winds (5 m s^{-1} shading interval, dashed lines depict negative zonal winds, zero contour omitted) and negative zonal stretching deformation (s^{-1}, red contours). Zonal stretching deformation contour interval: -5x10^{-7} s^{-1}; thick lines depict the zero contour. 240 W m^{-2} OLR contour and box "A" outlined by blue and black lines, respectively.

also an equatorward shift of the Southern Hemisphere jet stream, resulting in a positive $\overline{U}$ bias exceeding 10 m s^{-1} throughout the diagonal SPCZ region at 20°S-35°S. Molteni (2003) documented similar 200 hPa zonal wind biases in simulations of the Southern Hemisphere using the same AGCM.

Despite the jet stream being too strong throughout the South Pacific basin, two regions of large-scale negative zonal stretching deformation still occur in the subtropics. Between Australia and east of New Zealand, the model enhanced jet stream decelerates from 45 m s^{-1} to 30 m s^{-1} ($\partial\overline{U}/\partial x = -3 \times 10^{-6} s^{-1}$). Further east, where the lowest OLR values in the subtropics are simulated, the jet stream bends poleward and $\partial\overline{U}/\partial x = -1.5 \times 10^{-6} s^{-1}$. The ITCP model simulates a narrow band of negative zonal stretching deformation collocated with the diagonal SPCZ, although the $\partial\overline{U}/\partial x$ magnitude is smaller than in the GFDL model ($-2.5 \times 10^{-6} s^{-1}$) and observations ($-3.5 \times 10^{-6} s^{-1}$). There is also no continuous band of $\partial\overline{U}/\partial x < 0$ between the mid-latitudes south of Australia and the SPCZ; however, the $\partial\overline{U}/\partial x$ discontinuity is small in area and only slightly positive.

3.3 Comparison between models and observations

Each model simulates the salient characteristics of the Pacific basic state circulation, however, subtle differences exist between models and compared to observations. The East Pacific high is present in both the GFDL and ICTP simulations, although surface pressures are somewhat lower compared to the NCEP reanalysis. Negative zonal stretching deformation is also reduced in the central Pacific and both models simulate a cloud band which is narrower, less diagonal, and further east than observed. Within the diagonal branch of the SPCZ, convection oscillates mostly on synoptic timescales in models and observations, although variability is reduced in the uncoupled simulation. In only the coupled model, an anomalous band of convection (i.e., the double ITCZ problem) extends horizontally in the tropical Southeast Pacific and merges with the SPCZ.

Comparison between the GFDL simulated SST (Figure 3.11) and the SST climatology used to force the ICTP model (Figure 3.12) yields several clues about why the coupled and uncoupled models simulate the Pacific basic state circulation differently. The most striking differences between SST fields are in the tropical East Pacific. In a narrow strip along the equator, colder SSTs are simulated by the GFDL model, while a warm bias exists to the south. Wittenberg et al. (2006) noted strong equatorial upwelling in the GFDL model and that precipitation biases are collocated with local SST biases (higher rainfall is common over warmer waters, and vice versa). Enhanced upwelling of cold equatorial deep water may be a result of an excited Ekman pumping mechanism driven by trade winds (Figure 3.4a) that are too strong. The complex meridional SST gradient in the East Pacific forces too little precipitation on the equator, where SSTs are too cold, and enhanced precipitation in the South Pacific double ITCZ, where SSTs are too warm. No double ITCZ bias is evident in the ICTP simulation, which is forced by observed SSTs.

Away from the tropical East Pacific, simulated and observed SSTs are mostly similar. The GFDL model (Figure 3.11) correctly simulates a tropical warm pool in the west and a large-scale meridional SST gradient throughout the subtropics. A basin-scale zonal SST

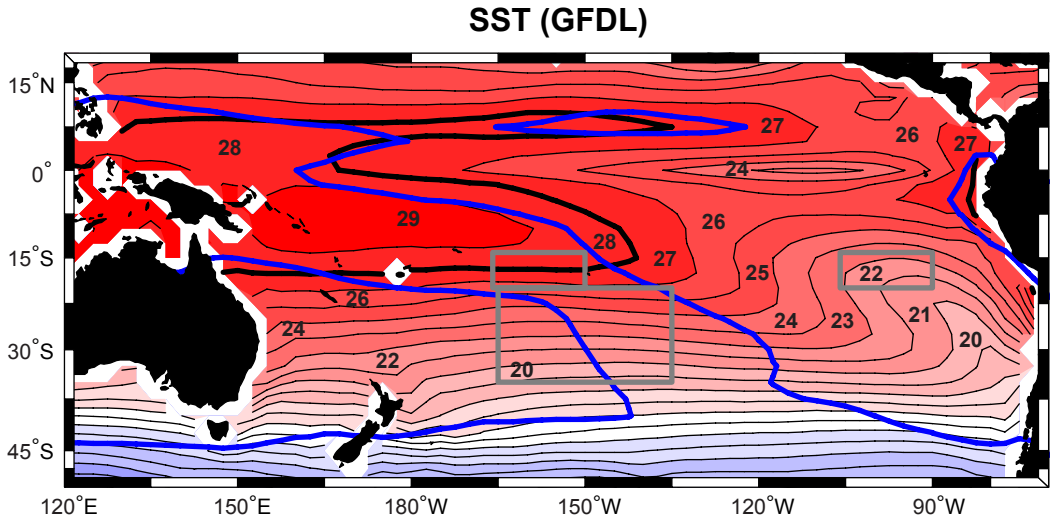

Figure 3.11: GFDL run two: DJF climatology (1982-2000) of SST (1°C interval, thick black contour encloses temperatures above 28°C). Gray boxes denote averaging regions ("A", "B", and "C") described in Chapter 2. 240 W m^{-2} OLR contour outlined by blue lines.

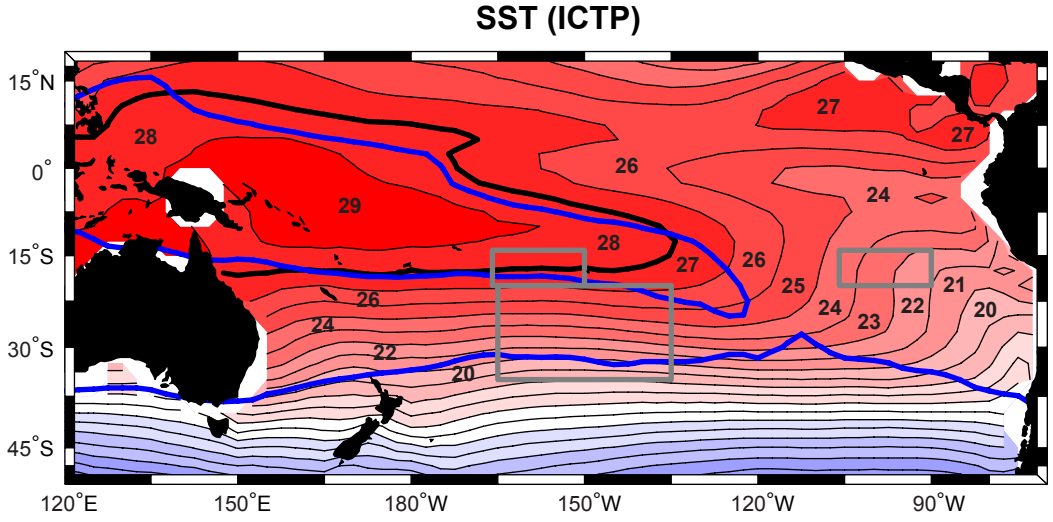

Figure 3.12: Same as Figure 3.11, but for the ICTP boundary forcing: ERA15 SST climatology during DJF (1981-1990).

gradient, which transects the SPCZ in the tropics and subtropics, is also clearly apparent. SSTs in box B are about 6°C warmer than box C in the GFDL model, ERA-15 data used to force the ICTP model (1981-1990), and NOAA satellite observations (1982-2008, see Figure 2.8).

Figure 3.13 provides a comparison of meridional average (20°S-35°S) OLR and zonal stretching deformation for the simulated and observed Pacific climate. Observed $\partial\overline{U}\big/\partial x < 0$ (gray shading) is clearly collocated with low OLR in the central Pacific. Elsewhere, stretching deformation is mostly positive and convection is weak. A similar spatial relationship is seen for the GFDL and ICTP models, although the lowest OLR and $\partial\overline{U}\big/\partial x < 0$ is shifted slightly east. The ICTP model does, however, simulate an anomalous region of $\partial\overline{U}\big/\partial x > 0$ just west of the OLR minimum. Elsewhere, the stretching deformation and convection relationship mostly holds in the uncoupled model. In summary, the coupled and uncoupled model each simulates most of the large-scale climate features associated with the SPCZ. Collocation of a basin scale zonal SST gradient, $\partial\overline{U}\big/\partial x < 0$, and low OLR, in models and observations, suggests that the orientation of the SPCZ may be forced by surface temperatures and related to the longitudinally varying zonal flow in the upper troposphere.

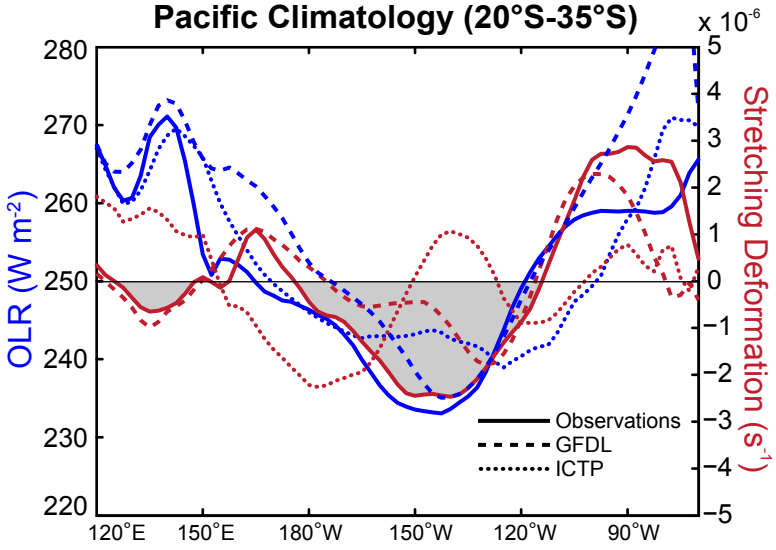

Figure 3.13: DJF climatology of OLR (blue) and 200 hPa zonal stretching deformation (red) for observations (1982-2008: solid), GFDL run two (1982-2000: dashed), and ICTP run one (24 seasons: dotted). Averaging is done over a 15° latitude band (20°S-35°S). Gray shading depicts regions of negative zonal stretching deformation from observations.

CHAPTER IV

HYPOTHESIS: WAVE ENERGY ACCUMULATION

Figures 2.6, 3.5, and 3.10 reveal the complex latitudinal and longitudinal structure in both the observed and simulated zonal wind field. Zhang and Webster (1989) explored the dynamical impacts of the sign of the basic zonal flow and the degree of latitudinal shear in zonally symmetric atmospheres. Relatively small differences were found in wave structure and propagation speed for easterly or westerly equatorial winds. But a comparison of Figures 2.1 and 2.6 suggests less subtle relationships between longitudinal variations of observed convection and the basic state; especially between low OLR and $\partial\overline{U}\big/\partial x < 0$ in the diagonal portion of the SPCZ such as in box A. For later reference, note that the negative stretching deformation region exists southwest of a large SST zonal gradient between boxes B and C, as shown in Figure 2.9. In the model domains, similar relationships exist between the zonal SST gradient, convergence of the zonal flow, and convection (e.g., see the respective fields from the ICTP Control simulation in Figures 3.12, 3.10, and 3.6).

The relationship between longitudinal stretching deformation of the climatological background state and imbedded transients has been studied extensively although principally with a low-latitude focus, such as in the lower troposphere of the tropical SPCZ. Numerical experiments with a wave source in a longitudinally varying basic flow (Webster and Holton 1982) showed evidence of transients being trapped in regions where $\partial\overline{U}\big/\partial x < 0$. To first approximation, such trapping, together with the increase in regional wave energy density, occurs when the longitudinal group speed of the mode (C_{gx}) approaches zero. But a series of studies (Webster and Chang 1988; Webster and Chang 1997; Chang and Webster 1990, 1995) showed that there are also kinematic implications of waves propagating through a zonally varying basic flow. Based on earlier work of Bretherton and Garrett (1968) and

Lighthill (1978), a series of rules were derived relating the structure and energy of waves to the character of the background zonal flow. Under the constraints that the background wind field varies gradually in space and the frequency of synoptic-scale Rossby waves is conserved, Webster and Chang (1997) derived the following expressions:

$$\frac{dk}{dt} = -k\frac{\partial \overline{U}}{\partial x} \tag{9}$$

$$\frac{d\xi}{dt} = -\xi\frac{\partial \overline{U}}{\partial x} \tag{10}$$

Here, k is the longitudinal wave number emerging from the assumption of normal mode solutions of the form $\propto i\,(kx + mz - \omega_r t)$, where m is the vertical wave number and ω_r is the intrinsic frequency of the mode in a frame of reference where $\overline{U} = 0$ (Webster and Chang 1988). ξ is the wave energy density given by $\xi = \rho g h^2 \big/ 2$, where ρ is density and h is the equivalent depth of the mode. The wave action density (ϵ), conserved along a ray (i.e., along a path defined as $dx/dt = C_{gd}$), is essentially ξ divided by ω_r (Lighthill 1978). The substantial derivative is defined to follow the local Doppler-shifted group speed of the mode, $C_{gd} = \overline{U}\,(x) + C_{gx}$, and is given by:

$$\frac{d}{dt} = \frac{\partial}{\partial t} + C_{gd}\frac{\partial}{\partial x} \tag{11}$$

The longitudinal group speed is defined as:

$$C_{gx} = -\left[\frac{\beta\left(k^2 + \beta\,(2n+1)/c\right) - 2k^2\beta}{\left(k^2 + \beta\,(2n+1)/c\right)^2}\right] \tag{12}$$

on an equatorial β–plane, where $c = \sqrt{gh}$ and n is the latitudinal nodal number. Details of Rossby wave propagation in a heterogeneous zonal flow are given in Webster and Chang (1997) and only the salient properties are presented here. These are:

(i) The group velocity for synoptic-scale Rossby waves is eastward relative to the basic state.

(ii) Changes in the scale of the wave are determined by the sign of the zonal stretching deformation. From Equation 9, if $\partial \overline{U} \big/ \partial x < 0$ then k will increase along a ray, hence

decreasing its longitudinal scale. As k increases, the longitudinal group speed C_{gx} will correspondingly decrease, as can be seen from Equation 12.

(iii) From Equation 9, if $\partial\overline{U}\big/\partial x < 0$ then the wave energy density will increase along a ray.

Farrell and Watterson (1985) used ray tracing to examine how synoptic scale Rossby waves propagate through a decelerating zonal flow and found kinematic results similar to Webster and Chang (1997), but for mid-latitude disturbances in the Northern Hemisphere. Following Equation 9 and also assuming that the disturbance length scale is much smaller than the length scale of the basic state, they demonstrated that the zonal wavenumber of a disturbance increases monotonically for propagation into an opposing current which varies along the path:

$$\frac{dk}{dx} = \frac{1}{dx/dt}\frac{dk}{dt} = \frac{-k\overline{U}_x}{\left(\overline{U} + C_{gx}\right)} \tag{13}$$

Considering the case for an eastward propagating Rossby wave ($C_{gx} > 0$) entering a region of convergent zonal velocity ($\partial\overline{U}\big/\partial x < 0$), such as east of Australia in the jet exit region seen in Figure 2.6, Farrell and Watterson (1985) show qualitatively that the disturbance would be observed to increase in amplitude and decrease in zonal wavelength until maximum amplitude is reached when its wavelength has been reduced to about half its original scale. The disturbance may then continue to steepen as the amplitude falls and ultimately may become "cutoff" from the long wave circulation. They find that Rossby waves are unable to penetrate convergent flows as small as 10^{-6} s^{-1} over 4000 km ($\partial\overline{U}\big/\partial x < -3.5\times10^{-6}$ s^{-1} is observed in the subtropical SPCZ). According to Farrell and Watterson (1985), convergent flow acts as a filter, or like a "hydraulic breakwater" in surface gravity wave theory, to Rossby waves entering a $\partial\overline{U}\big/\partial x < 0$ region.

The Farrell and Watterson (1985) ray tracing analysis is applicable to Southern Hemisphere mid-latitude Rossby waves which have been observed to propagate from south of Australia, along the decelerating jet stream, into the subtropical SPCZ (Trenberth 1991).

We pose the hypothesis that eastward propagating disturbances encounter a region of negative zonal stretching deformation in the upper troposphere where their longitudinal extent shrinks, their group speed is reduced, and wave energy "accumulates" (i.e., locally increases). The expected result is a highly energetic convective region (i.e., low OLR) oriented diagonally away from the equator in the South Pacific.

CHAPTER V

TESTING THE HYPOTHESIS

To test the hypothesis of wave energy accumulation, we need to determine the factors that control the Southern Hemisphere circulation patterns which produce a region of negative zonal stretching deformation in the region of the SPCZ. Furthermore, we must provide evidence that disturbances passing though such a region are modified according to Equations 9 and 10. We perform controlled numerical experiments using the ICTP global climate model to address the first problem and then quantify interannual changes in the observed SPCZ. We then use additional numerical experiments to examine how the SPCZ responds to various types of ENSO events (i.e., by forcing the model with four surface heating patterns centered in different regions of the equatorial Pacific). The second problem concerning wave modification is addressed by compositing synoptic disturbances as they enter the negative zonal stretching deformation region. We compute **Q** vectors to analyze the vertical modification of these disturbances and to determine if wave energy accumulation leads to enhanced convection.

Before investigating the factors that determine the background basic state of the Southern Hemisphere, we examine a case study of disturbances in the subtropics. The period 1 December 2005 to 28 February 2006, representative of typical ENSO-neutral conditions, is chosen for the case study. Figure 5.1 shows a longitude-time plot of OLR and negative zonal stretching deformation at 200 hPa averaged between 20°S-35°S around the entire Southern Hemisphere. Neither the OLR nor $\partial\overline{U}\big/\partial x$ fields have been filtered.

A striking feature of the longitude-time section is that the shaded OLR regions (< 240 W m^{-2}) occur in three longitudinal bands, each corresponding to a major quasi-stationary Southern Hemisphere convergence zone (SICZ: 25°E-50°E, SPCZ: 165°W-135°W, and

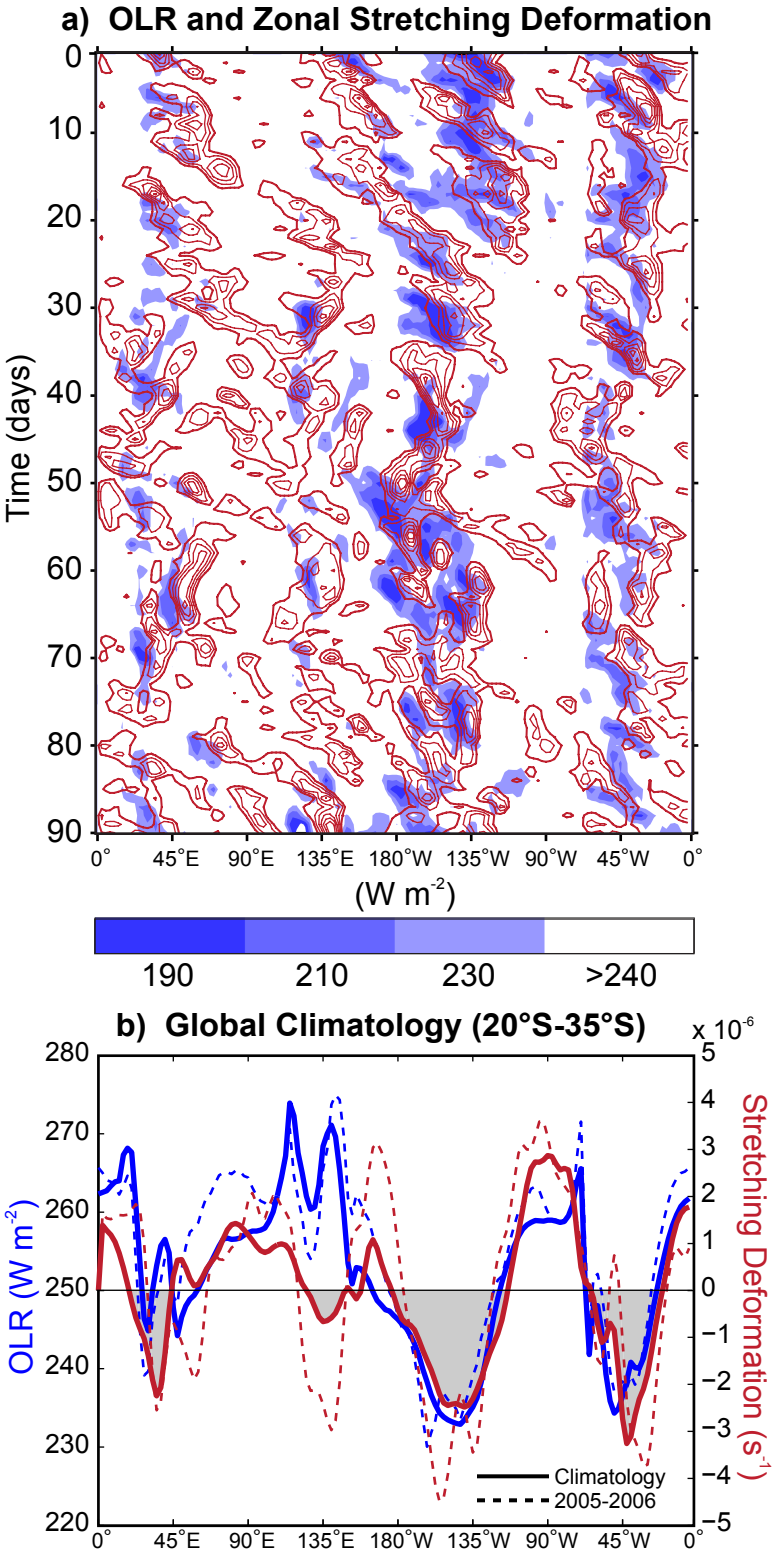
a) OLR and Zonal Stretching Deformation
Time (days)
0
10
20
30
40
50
60
70
80
90
0°
45°E
90°E
135°E
180°W
135°W
90°W
45°W
0°
(W m-2)
190
210
230
>240
b) Global Climatology (20°S-35°S)
x 10-6
OLR (W m-2)
Stretching Deformation (s-1)
280
270
260
250
240
230
220
5
4
3
2
1
0
−1
−2
−3
−4
−5
Climatology
2005-2006

Figure 5.1: (a) Hovmoller (longitude-time) of observed OLR (shading depicts values less than 240 W m^{-2}) and 200 hPa zonal stretching deformation (s^{-1}, contours) during 1 December 2005 to 28 February 2006. Zonal stretching deformation contour interval: -4x10^{-6} s^{-1}; thick lines depict the -2x10^{-6} s^{-1} contour. Averaging is done over a 15° latitude band (20°S-35°S). (b) 2005-2006 DJF (dashed lines) and 27 season climatology (solid lines) of OLR (blue) and zonal stretching deformation (red). Gray shading depicts regions of negative zonal stretching deformation, according to climatology.

SACZ: 60°W-30°W) as described by Streten (1973) and Kodama (1993). Low OLR is also occasionally observed in a fourth narrow band near 135°E; however, moisture support does not often exist for deep convection over central Australia. A clear demarcation between the central and eastern South Pacific is apparent around 120°W in both the OLR and $\partial\overline{U}\big/\partial x$ distribution. The longitude-time section suggests that the eastern border of the SPCZ corresponds spatially and temporally to the sign change of zonal stretching deformation (Figure 5.1b). Within the $\partial\overline{U}\big/\partial x < 0$ contours, zonal propagation speed slows down. Outside of negative stretching deformation zones, which often correspond to jet stream exit regions, any disturbance that develops is observed to propagate more rapidly eastward with a reduction in amplitude as suggested by Equations 9-12. We will quantify these observations in Chapter 5.3.

Figure 5.1a is representative of other years as well. Figure 5.1b shows a comparison of the 2005-2006 DJF of OLR and 200 hPa $\partial\overline{U}\big/\partial x$ (dashed lines) with the 27-year climatology (solid lines) of the same quantities in the same latitude band. Gray shading represents long-term average negative zonal stretching deformation. Except for subtle differences, the mean fields reflect the characteristics of the 2005-2006 case study. As with the case study, three pronounced areas where $\partial\overline{U}\big/\partial x < 0$ coincides with OLR minima are apparent, each corresponding to a major Southern Hemisphere convergence zone plus a fourth weaker region of $\partial\overline{U}\big/\partial x < 0$ near 135°E. On the other hand, Figure 5.1b indicates that regions where $\partial\overline{U}\big/\partial x > 0$ almost always have OLR values representative of shallow convection, or no convection at all.

5.1 Longitudinal variability of the climatological circulation

To gain an understanding of the factors that determine the background basic state of the Southern Hemisphere, we conduct a series of controlled numerical experiments using the AGCM provided by the ICTP and described in the Appendix (C.2). The idealized AGCM is configured, initialized from an atmosphere at rest, and integrated for a 26 year period according to the methodology used to obtain a climatology of the Control simulation (Chapter 3.2). Again, the first two years of integration are discarded and the 24 remaining years used to compile DJF seasonal averages.

Four experiments are conducted (summarized in Table 1):

(i) A "Control" run, where the model is forced by a fixed annual cycle of monthly climatological SSTs and land boundary conditions. The Control experiment describes the model response to a prescribed annual cycle of SST and a detailed climatology is examined in Chapter 3.2.

(ii) A "Topography" experiment examines the circulation response to the removal of elevated land surfaces. The surface boundary elevation of the coarse model, shown in Figure 5.2, is made flat in a global channel between 61°N-61°S. For later reference in Chapter 6, the simulated 250 W m^{-2} OLR contour (dashed line) is overlaid on the topography map because this higher threshold more accurately encloses weaker convection in the South Atlantic and South Indian Convergence Zones. Under normal conditions, both the SACZ and SICZ are oriented near elevated topographic features, while the SPCZ is not. However, in this experiment, the Andes, East African Highlands, Himalayas, and most of the Rockies are removed and the resultant forcing on the South Pacific climate is analyzed.

(iii) An "Orography" experiment examines the circulation response to the removal of continents in the same channel as the Topography experiment (61°N-61°S). In this zonal aqua-channel experiment, land surfaces are treated as ocean in the model by

using observed land surface temperatures to prescribe an artificial SST pattern. Land albedo is also lowered to match an ocean surface. Elsewhere, climatological boundary sea and land conditions are used. In essence, we attempt to determine the role of land processes in forcing the DJF climatology.

(iv) An "SST" experiment configured to test the importance of the zonal gradient of Pacific SST in forcing the quasi-stationary characteristics of the Southern Hemisphere. Specifically, the SST distribution of the Control experiment in the Pacific basin (61°N-61°S, 120°E-71°W) is replaced with the zonal average of the observed values by setting $dSST_{Pacific}/dx = 0$. The zonally averaged SST maintains an annual cycle consistent with the monthly varying climatology. Figure 5.3 shows the imposed heating anomaly in the Pacific basin during DJF. Elsewhere, SSTs have the same evolving climatological annual cycle used in the Control experiment. Large changes to the SST field are mostly confined to the tropics and subtropics because the observed zonal SST gradient used in the Control experiment is small poleward of 35°S, except for in portions of the North Pacific.

The purpose of the experiments is not to simulate exactly the observed atmospheric structure of the Southern Hemisphere. Such a task would have to be performed using a much higher resolution model. Rather, we attempt to determine the changes in simulated climatologies relative to the Control with, or without, SST alterations and topographic or orographic forcing factors. For each of the controlled numerical experiments, variations in the location and strength of convection, in addition to the frequency and propagation of disturbance activity, will be examined.

Figures 5.4-5.6 show respectively the Southern Hemisphere DJF climatology of simulated OLR, sea-level pressure (SLP), and 200 hPa zonal wind for the (a) Control, (b) Topography, (c) Orography, and (d) SST experiments. Departures from the Control simulation are shown for the Topography, Orography, and SST experiments. Comparison of Figure 5.4a with observed OLR (Figure 2.1) confirms the findings in Chapter 3.2 that the

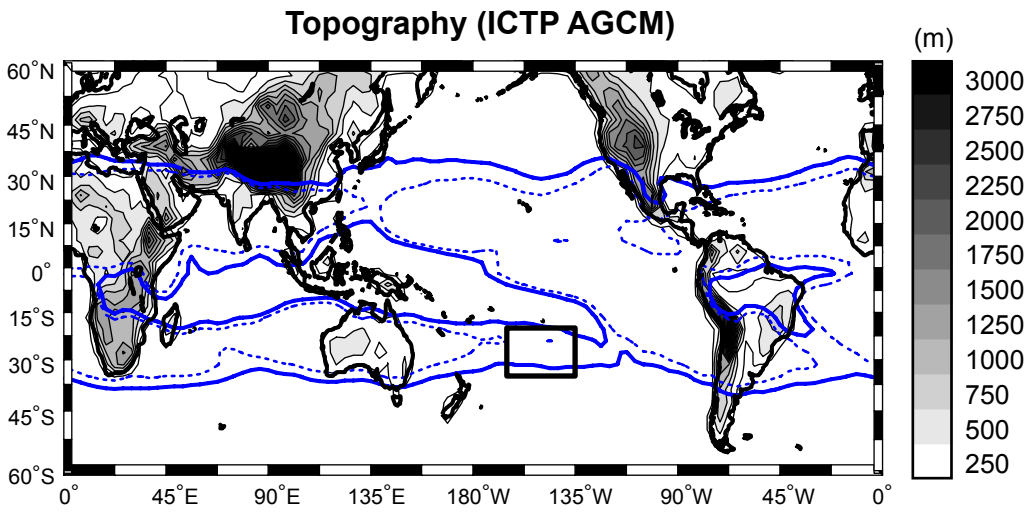

Figure 5.2: Land surface elevation (m) boundary condition in the ICTP AGCM. Large black box ("A": located at 20°S-35°S, 165°W-135°W) described in Chapter 2. Control OLR climatology for DJF indicated by blue contours: 240 W m^{-2} (solid) and 250 W m^{-2} (dashed).

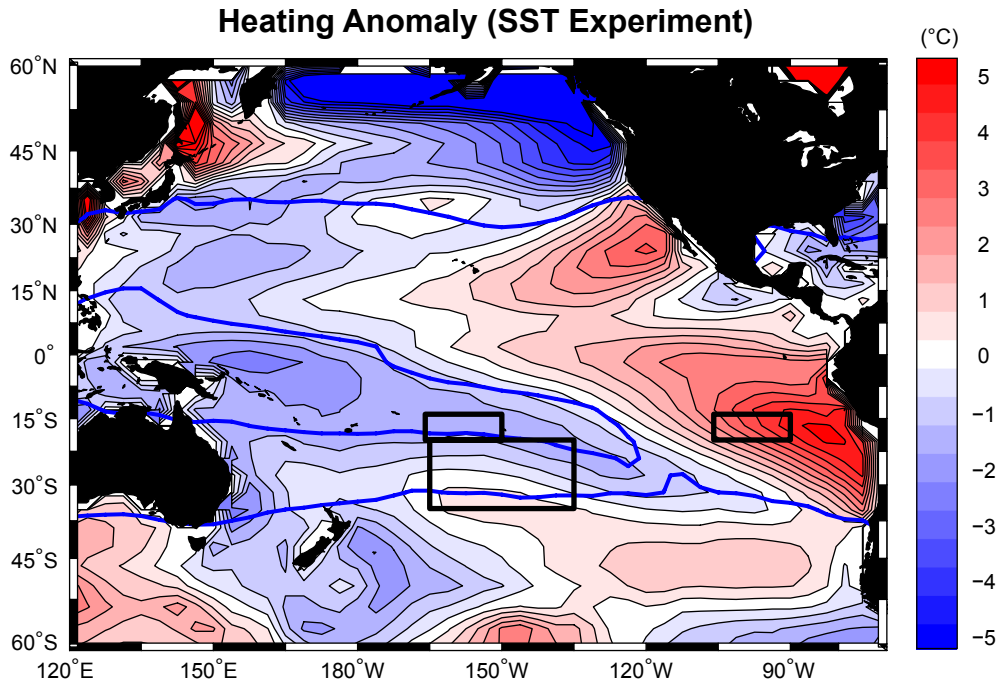

Figure 5.3: SST Experiment: Heating anomaly (°C) during DJF. Black boxes denote averaging regions ("A", "B", and "C") described in Chapter 2. 240 W m^{-2} OLR contour outlined by blue lines.

Table 1: Description of ICTP AGCM experiments. Topographic (land surface elevation), Orographic (land characteristics replaced as ocean surface), and SST forcing factors are altered for the indicated latitude and longitude ranges.

Experiment	**Details**	**Latitude Range Altered**	**Longitude Range Altered**
Control	Fixed annual cycle of monthly SSTs and land boundary conditions	—	—
Topography	Flat land surface	61°N-61°S	Global
Orography	Zonal aqua-channel	61°N-61°S	Global
SST	$\frac{d\,(\mathrm{SST}_{\mathrm{Pacific}})}{dx} = 0$	61°N-61°S	Pacific basin (120°E-71°W)

AGCM simulates a diagonal band of convection similar in location and intensity to the observed SPCZ, although again we note that the modeled convective zone is more zonally oriented. A thorough analysis of simulated convection and the basic state circulation of the South Pacific was provided in Chapter 3.2. Here, we briefly summarize a few features of the long wave pattern important to the SPCZ orientation. The idealized AGCM simulates a surface high pressure in the Southeast Pacific that is weaker than observed and extends too far west. These biases are evident in Figure 5.5a which shows that the simulated SLP exceeds 1016 hPa in much of the subtropical Pacific. The subtropical jet stream is also shifted equatorward in the model and 200 hPa westerlies are stronger than observed throughout the diagonal SPCZ (Figure 5.6a). Northeast of the SPCZ, the Control climatology possesses a westerly duct in the eastern equatorial Pacific, although it is weaker than observed.

Figure 5.7 shows the simulated OLR (blue) and 200 hPa zonal stretching deformation (red), averaged between 20°S-35°S, across the Pacific basin for each of the four experiments. The Control experiment is represented by solid lines and gray shading indicates regions of $\partial\overline{U}\big/\partial x < 0$ for the idealized experiments (dashed lines). In general, the Control

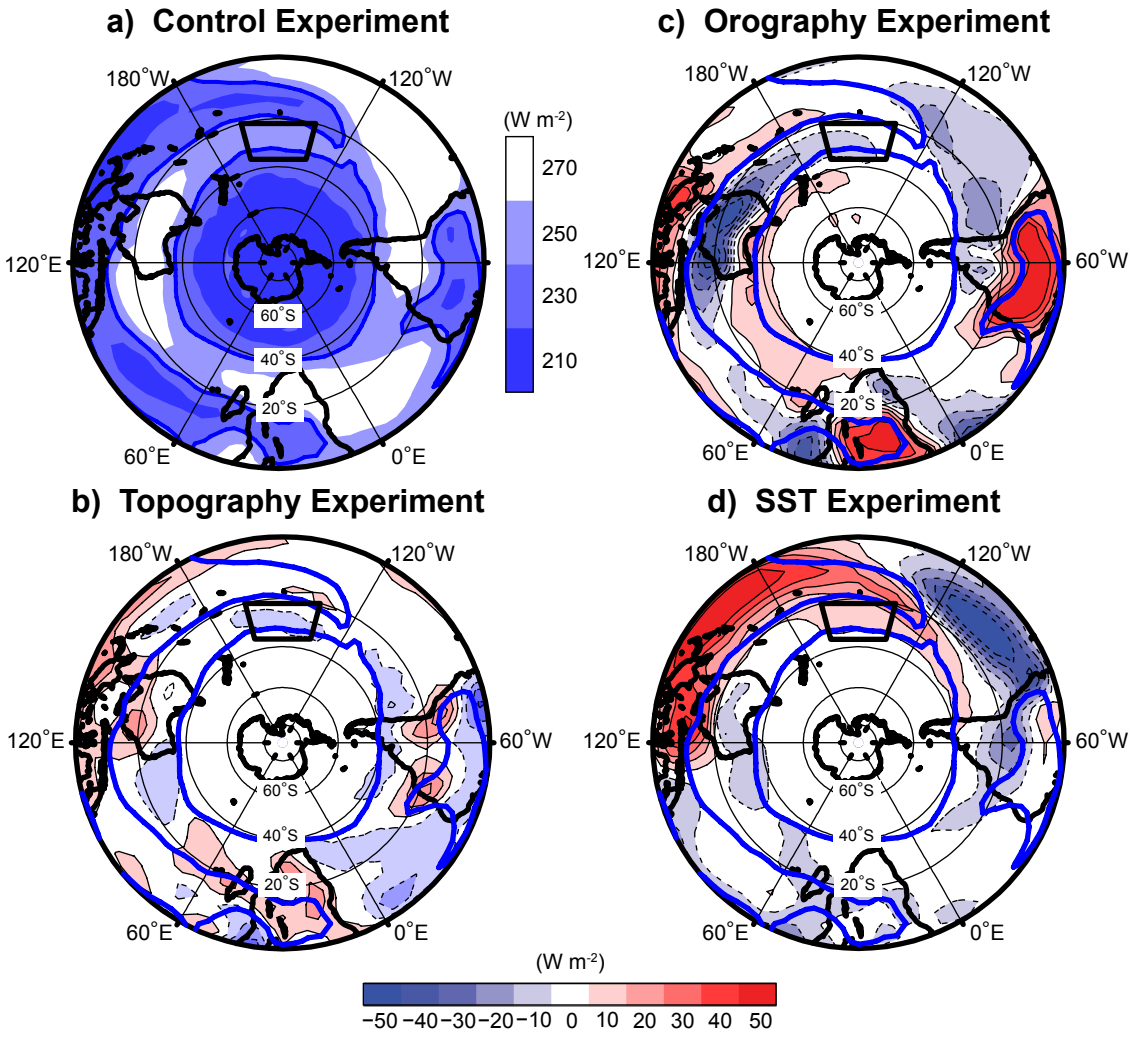

Figure 5.4: DJF climatology (24 seasons) of simulated OLR (W m^{-2}) for (a) Control, (b) Topography, (c) Orography, and (d) SST experiments. Departures from the Control simulation are shown for the Topography, Orography, and SST experiments. Trapezoids correspond to the OLR averaging box A described in Chapter 2. The 240 W m^{-2} OLR contour from the Control experiment is outlined by blue lines in each panel.

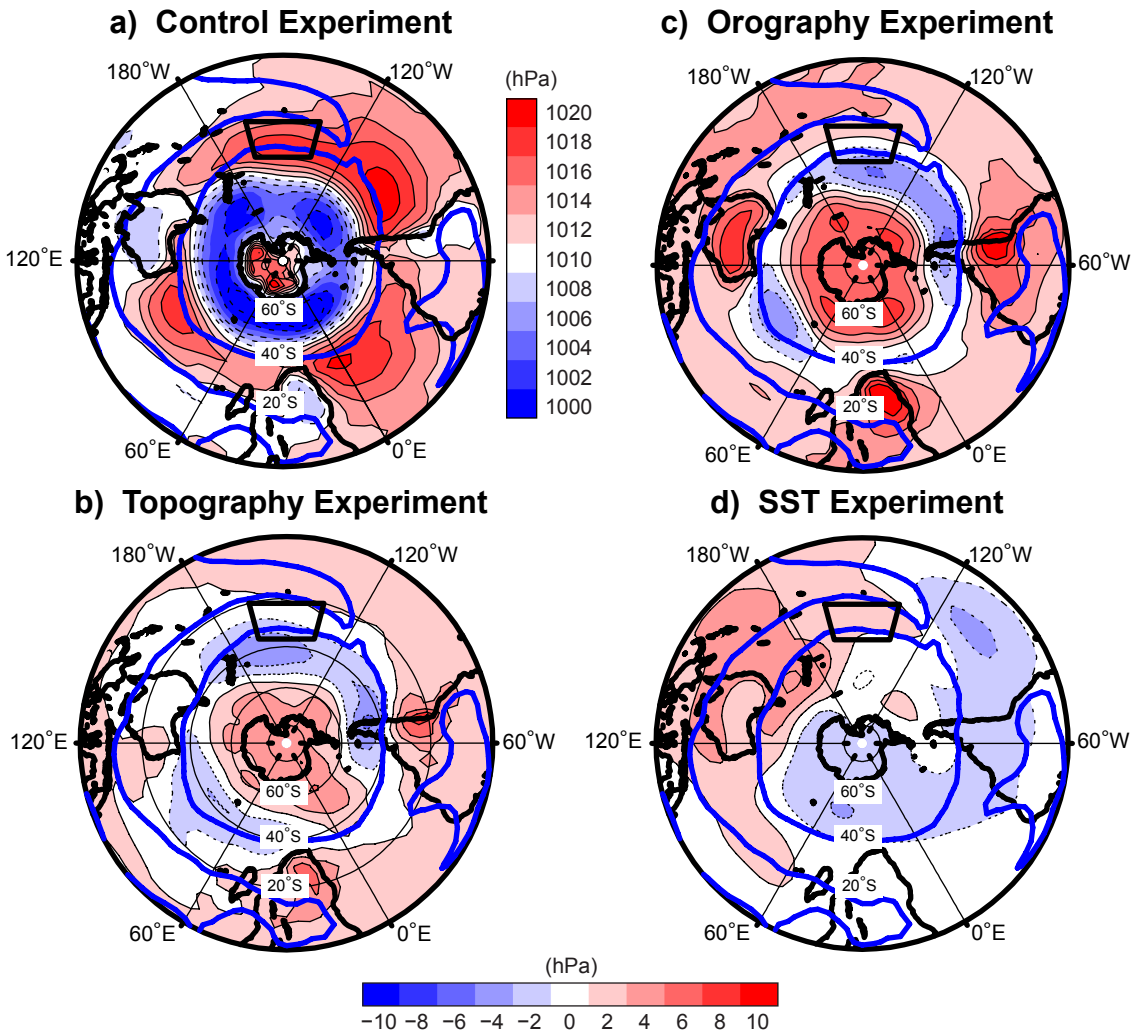

Figure 5.5: Same as Figure 5.4, but for sea-level pressure.

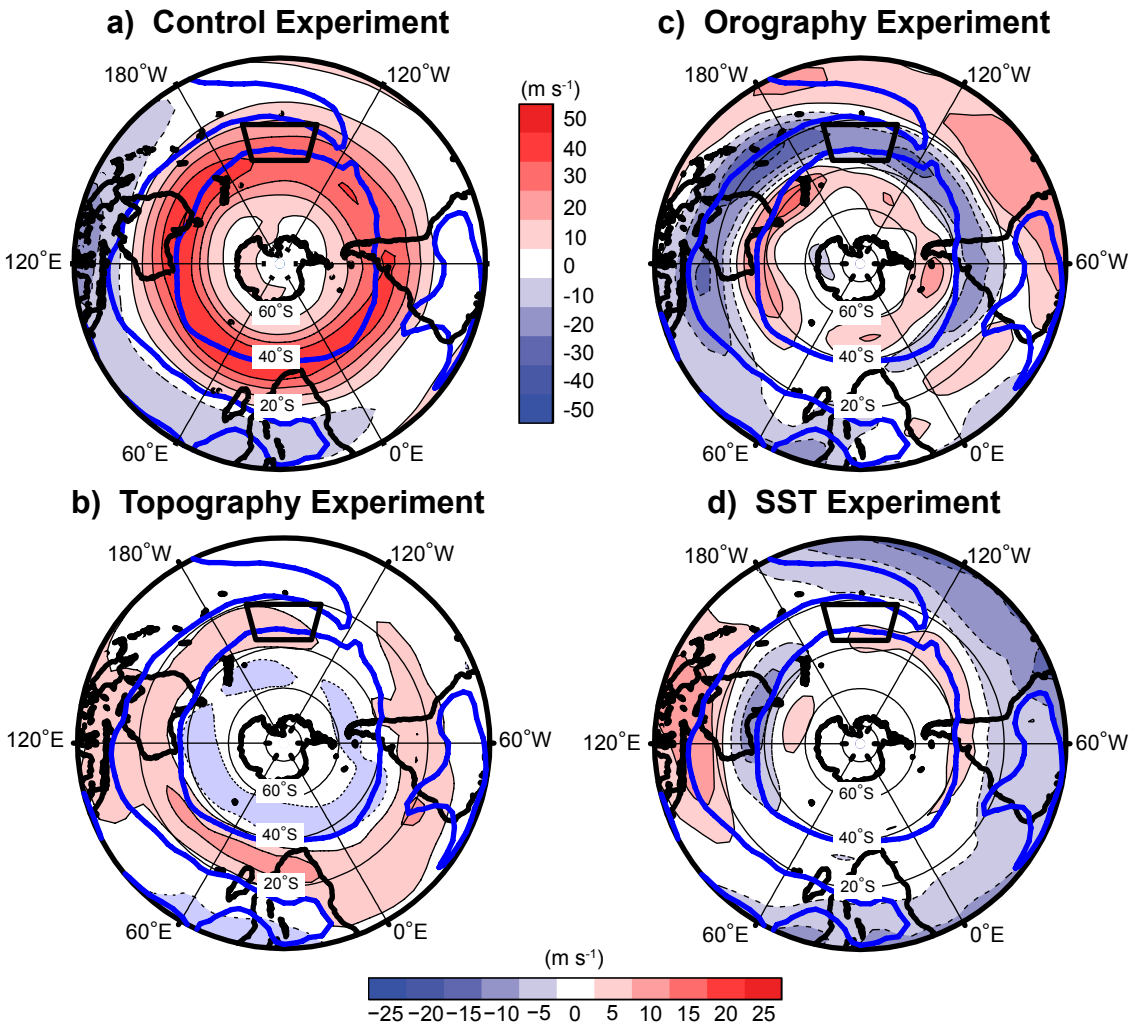

Figure 5.6: Same as Figure 5.4, but for 200 hPa zonal wind.

experiment shows a reasonable coincidence between low OLR and regions of $\partial\overline{U}\big/\partial x < 0$. A notable difference is evident between 150°W-130°W where convection is simulated but with a positive or near-zero zonal stretching deformation for each experiment.

Removal of land elevation (Topography experiment), or even the presence of land completely (Orography experiment), does not force large convective changes in the SPCZ subtropical region (Figure 5.4b and c, respectively), although strong OLR anomalies are observed near the location of each "continent". Surface pressures increase near the "continents" and also over most of the ocean basins in both experiments, except in the mid-latitudes where modest pressure drops occur (Figure 5.5b and c). The changes in the OLR distribution over Australia and Indonesia when the landmasses are removed (Figure 5.4c) are consistent with a southward shift of the simulated tropical SPCZ, and therefore a more zonally oriented band of convection extending into the central Pacific. The replacement of Australia with a warm ocean boundary essentially enlarges the West Pacific warm pool and shifts convection poleward. Only small changes near Australia and Indonesia are noted in the Topography experiment. Here, the land is either mostly flat or elevated surfaces are not depicted by the coarse model resolution. Elsewhere, convection decreases where the Andes and East African Highlands have been removed, but neither signal extends far into the adjacent ocean basins. In both experiments, pronounced OLR, SLP, and zonal wind anomalies (Figure 5.6b and c) are mostly constrained to regions outside the 180°W-120°W region, or away from the Control SPCZ (Figure 5.7a and b). While there are changes in the central Pacific circulation occurring with the removal of topography or orography, negative zonal stretching deformation still occurs in the vicinity of the subtropical SPCZ and convection in this zone remains mostly unchanged.

Removal of the Pacific zonal SST gradient (SST experiment) produces strong changes in the OLR (Figure 5.4d) and 200 hPa zonal wind patterns (Figure 5.6d) especially over the Pacific (Figure 5.7c, dashed lines), but also extending, to a lesser degree, into the Atlantic

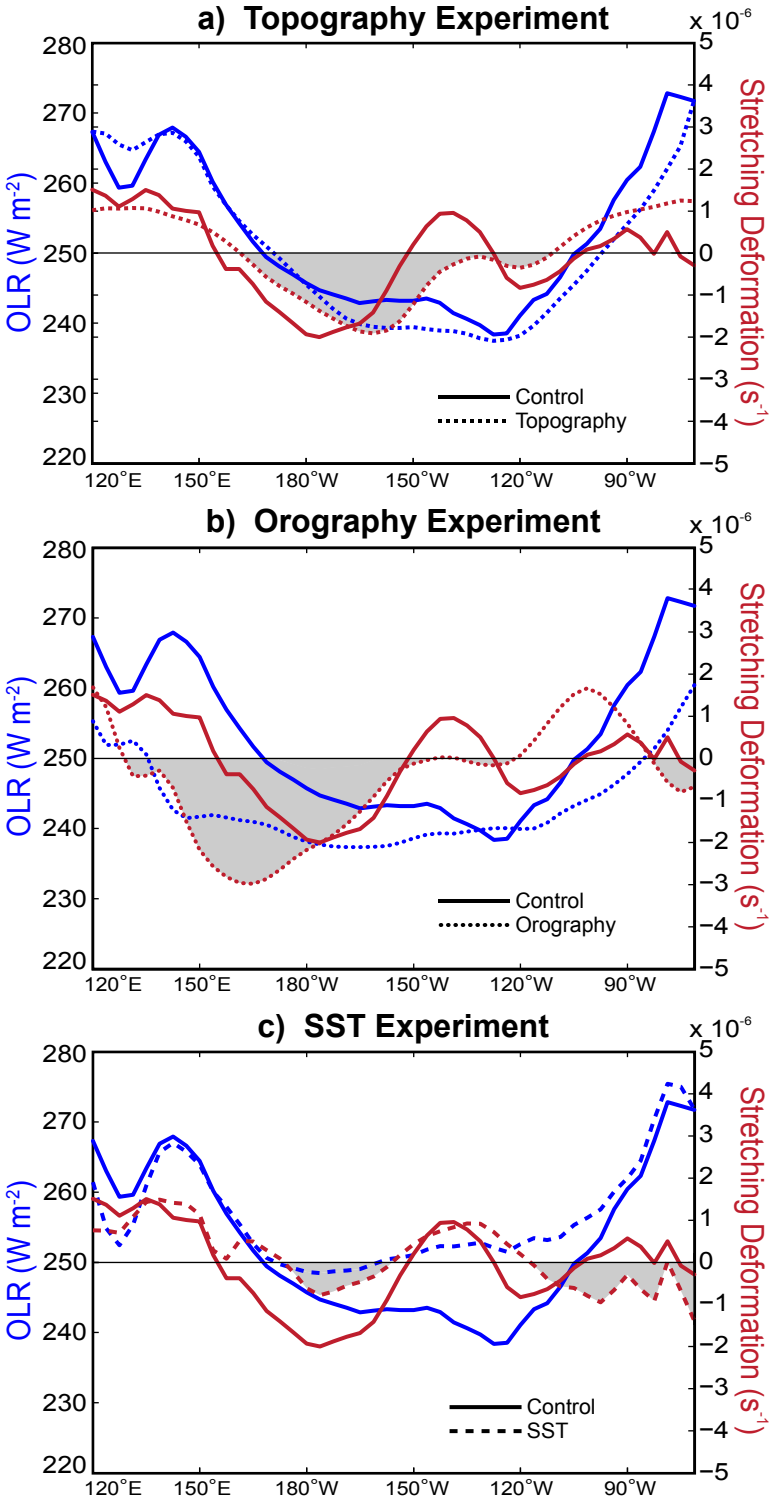

Figure 5.7: DJF climatology (24 seasons) of simulated OLR (blue) and 200 hPa zonal stretching deformation (red) for the (a) Topography, (b) Orography, and (c) SST experiments. Solid lines indicate values from the Control experiment. Averaging is done over a 15° latitude band (20°S-35°S). Gray shading depicts regions of negative zonal stretching deformation from each respective experiment.

and Indian basins. SLP anomalies are also mostly constrained to the Pacific basin (Figure 5.5d), where pressures are about 4 hPa higher than the Control in the west and drop by an equivalent amount in the east. Positive OLR anomalies (reduced convection) exceed 50 W m^{-2} in the tropical SPCZ region (120°E-180°W); with an axis of positive OLR anomalies oriented diagonally and coinciding with the location of the SPCZ in the Control run. To the northeast of the Control SPCZ, large OLR reductions occur suggesting a migration of the SPCZ to the northeast. Clearly, the zonal SST gradients are related to the location and orientation of the SPCZ.

The 200 hPa zonal wind, sea-level pressure, and OLR fields in the SST experiment are similar to patterns observed during El Niño events (e.g., Streten and Zillman 1984; Trenberth 1997; Vincent 1999). Upper tropospheric easterly winds over the West Pacific warm pool become weaker, or even westerly, while easterly wind anomalies are found throughout the remainder of the tropics. All of these features are consistent with a weaker Pacific Walker circulation. To the south, the jet stream weakens over Australia (-20 m s^{-1}) and strengthens over the eastern Pacific (+10 m s^{-1}). In the subtropical region of the SPCZ, zonal stretching deformation becomes less negative, compared to the Control, and positive OLR anomalies (10-20 W m^{-2}) are also observed (Figure 5.7c).

To confirm that the AGCM simulates realistic perturbations of the basic state on synoptic timescales, we compare a case study of simulated disturbances in the subtropics (Figure 5.8) to the observational case study discussed at the beginning of this chapter (Figure 5.1). Here, we examine a longitude-time plot of unfiltered OLR and negative zonal stretching deformation at 200 hPa. Similar to the observational analysis, the fields are averaged between 20°S-35°S around the entire Southern Hemisphere. The 19^{th} DJF period of the simulation is shown because of its close similarity to the 24 year seasonal average (Figure 5.8b, dashed and solid lines, respectively), although each year is similar to climatology because there is no interannual SST variability in the uncoupled model.

Like the longitude-time plot of observations, three bands of low OLR are simulated

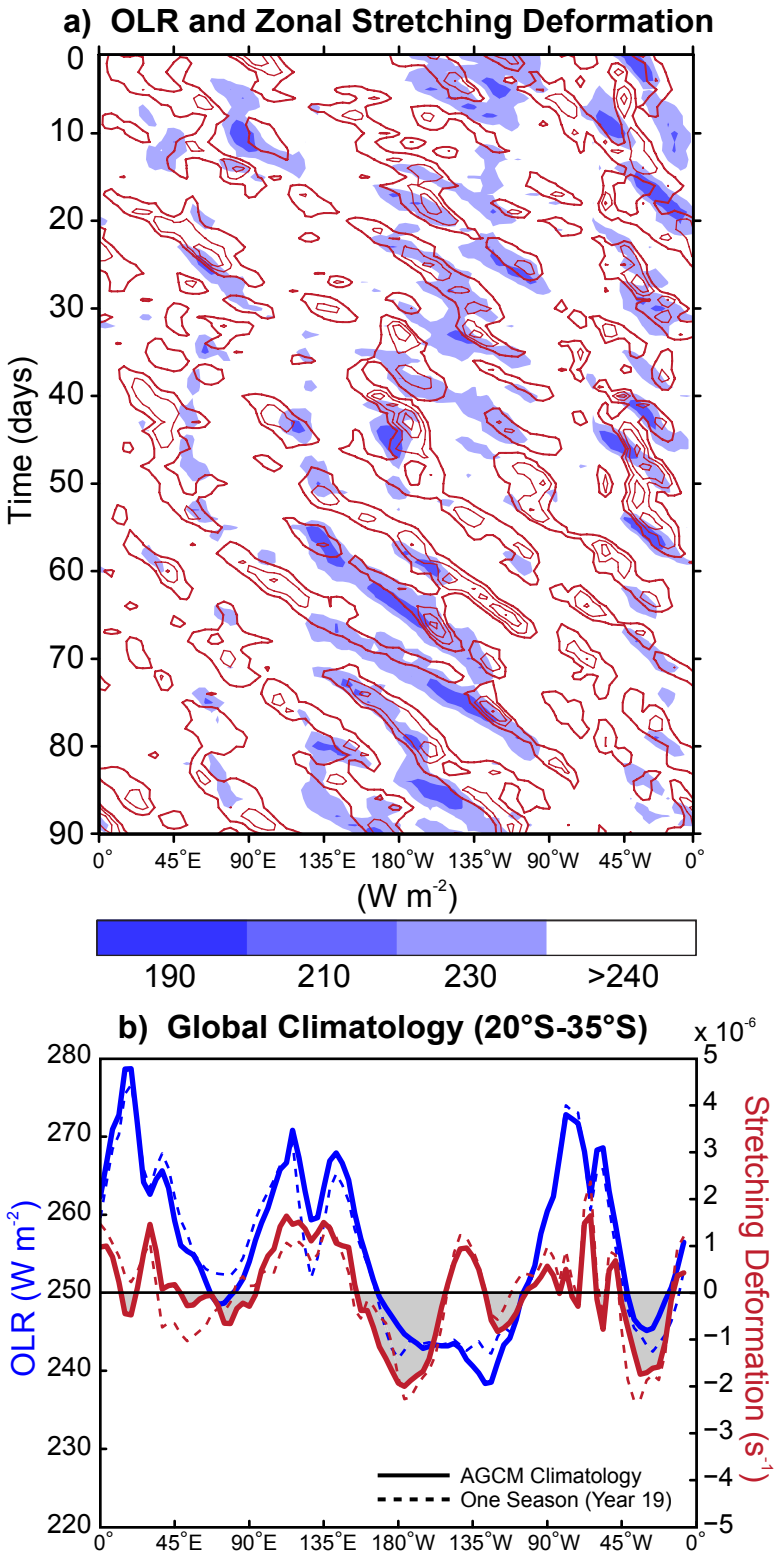

Figure 5.8: Same as Figure 5.1, but for the ITCP AGCM Control experiment during DJF for the 19th year of the simulation.

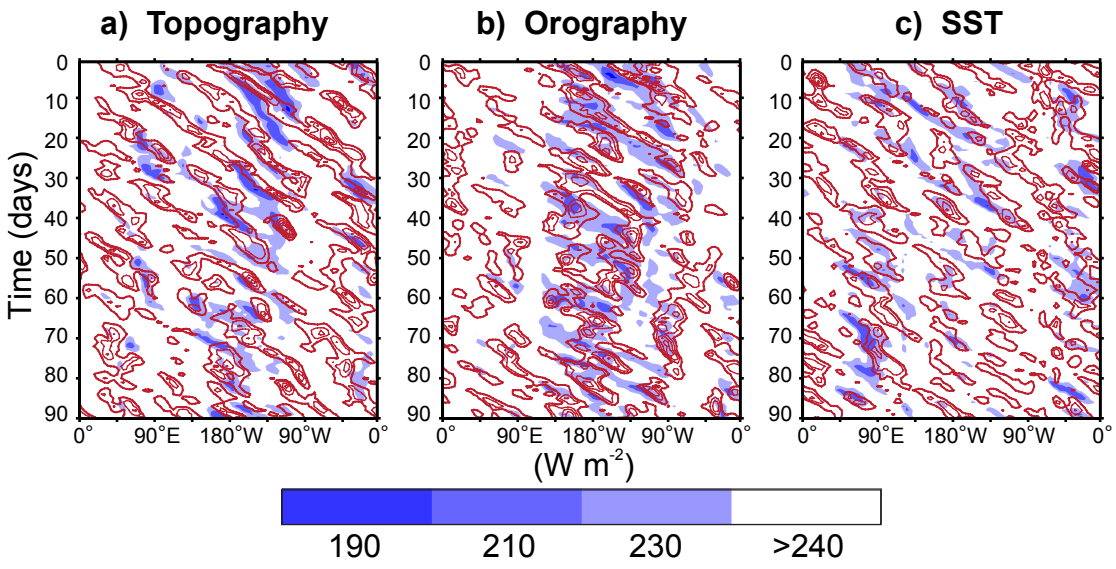

Figure 5.9: Same as Figure 5.1a, but for the (a) Topography, (b) Orography, and (c) SST experiments during DJF for the 19th year of the simulation.

(Figure 5.8a) and $\partial\overline{U}/\partial x < 0$ coincides with OLR minima in each region (Figure 5.8a, gray shading). Convection in the model is most frequent and strongest in the central Pacific, especially around 135°W. Elsewhere, low OLR is simulated over parts of the Indian and Atlantic oceans. In each of the three convective bands, however, average OLR is slightly higher than observed and there are some periods when no convection is apparent at all. Simulated disturbances also often track more rapidly than observed across the Pacific.

In both the Topography and Orography experiments (Figure 5.9a and b), the occurrence of convection over the central Pacific is mostly similar to the Control. Periods of OLR values less than 240 W m^{-2} (blue shading) are clearly simulated in the SPCZ region (e.g., near 180°W). Elsewhere, convection is slightly less common than the Control, especially in the Atlantic basin when the continents are completely removed. Over the Pacific, a striking decrease of convective events occurs when the zonal SST gradient is removed (Figure 5.9c). Disturbances still seem to propagate into the Pacific, but convection rarely amplifies. To the east and west, bands of convection over the Indian and Atlantic basins remain, which is expected because SSTs are the same as the Control outside of the Pacific.

In summary, results of the numerical experiments point to the importance of the Pacific zonal SST gradient in determining where regions of negative zonal stretching deformation exist and, hence, where enhanced disturbance activity and OLR minima are likely to occur. The distributions of mountain ranges and land surfaces, both in the Northern and Southern Hemispheres, have a much smaller impact on the location of convection, at least in the central Pacific basin of the coarse GCM which is forced by fixed monthly varying SSTs.

5.2 Interannual variability of the SPCZ

The idealized numerical experiments have shown that the SST distribution dictates, to a large degree, the background quasi-stationary flow of the Southern Hemisphere; clarifying the much simpler arguments of Webster (1972) and Gill (1980). Furthermore, these patterns have attendant regions of negative zonal stretching deformation that force higher frequency disturbances to become more energetic. Slow modulations of the background SST, such as occurring during ENSO events, should modify the basic sate and carry with these modifications signatures of zonal stretching deformation consistent with changes in the location of the SPCZ. We next test this hypothesis using time series and case study analyses of observations and then compare the results to a series of specified numerical experiments forced by various surface heating patterns which represent four different types of ENSO events.

5.2.1 Observational experiments

During most El Niño periods, the SPCZ exhibits a distinct shift to the northeast (Streten and Zillman 1984; Trenberth 1997; Vincent 1999; Juillet-Leclerc et al. 2006; Vincent et al. 2009). An opposite shift towards the southwest accompanies La Niña. Similar migrations of convective and zonal wind anomalies are simulated by the SST experiment (Figures 5.4d and 5.6d). The relationship between SST and wind distributions can be tested by seeing if the zonal SST gradient is correlated with 200 hPa zonal stretching deformation and whether

changes in the zonal wind fields are matched by variations in the strength of SPCZ convection.

An SST gradient index (the difference in SST between boxes B and C shown in Figure 2.8) is developed to quantify interannual changes across the South Pacific basin. The index is standardized by removing the mean and dividing by the standard deviation. Figure 5.10a shows a time series of the index. Pronounced interannual variability is observed with smaller values typically associated with El Niño and larger values with La Niña. For example, the gradient increase between 1998, a strong El Niño period, and 1999, a strong La Niña period, exceeds two standard deviations. Overlaid on Figure 5.10a is the linear trend suggesting that the South Pacific zonal SST gradient may have increased from 1982-2008. Caution should be applied when interpreting whether the long-term gradient change is significant, as some of the 27 year signal could be attributed to interannual variability.

Interannual variability of the off-equatorial zonal SST gradient is highly correlated with large heating anomalies in the equatorial Pacific, as shown by the linear regression of the SST index onto monthly SST anomalies (Figure 5.11). The long term SST trend was removed prior to computing the regression; however, retaining the trend would result in only slight changes to the regression anomalies. SST anomalies in the equatorial Pacific have been linked previously in many studies to global teleconnection processes (e.g., Trenberth 1997) and SPCZ variability (e.g., Vincent et al. 2009). In general, the SST regression map is similar to the canonical ENSO pattern, although anomalies are more pronounced than typical in the off-equatorial region near where the zonal SST gradient is defined.

Figure 5.10b and c show the corresponding seasonal averages of OLR and 200 hPa zonal stretching deformation, respectively, for box A (Figure 2.8) located in the subtropical SPCZ. The OLR and $\partial\overline{U}\big/\partial x$ indices are standardized using the methods discussed above to allow comparison with the SST gradient index. Interannual variability is also evident for both OLR and $\partial\overline{U}\big/\partial x$, with the indices typically increasing (decreasing) during El Niño

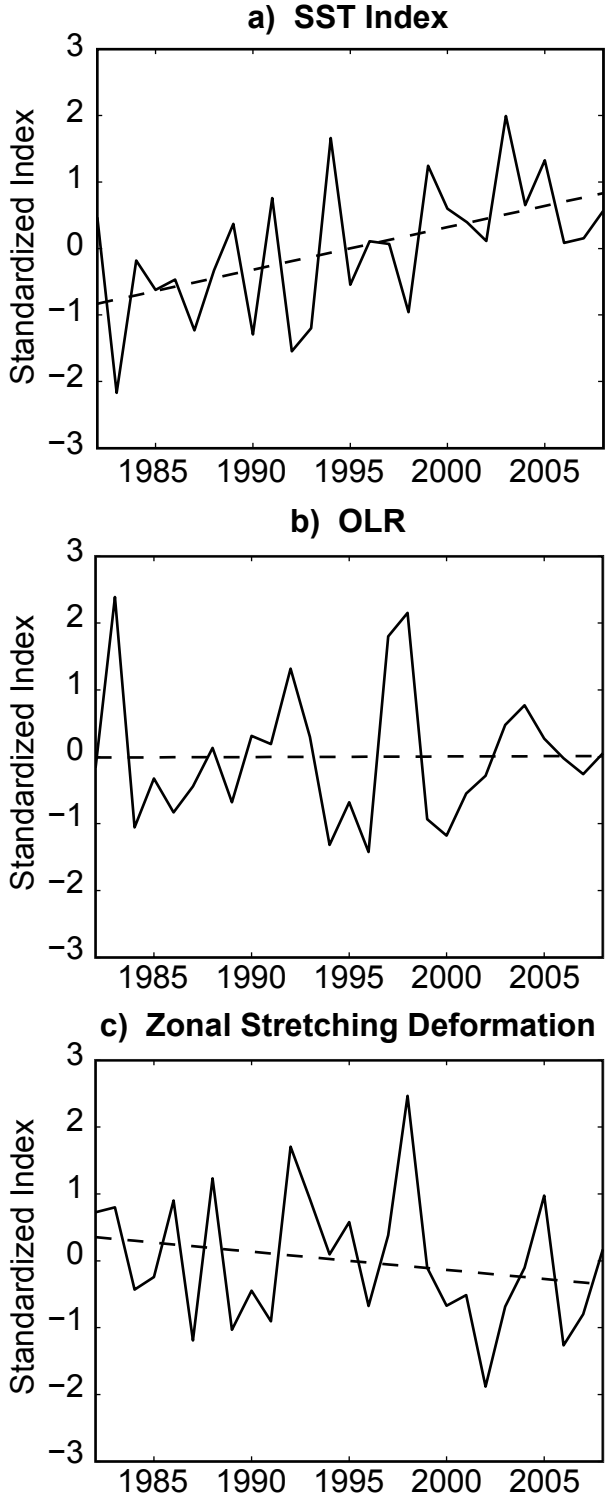

Figure 5.10: Standardized SST index (a), OLR (b), 200 hPa zonal stretching deformation (c), and corresponding linear trends (dashed lines) for the averaging regions described in Figure 2.8 (SST index: difference between boxes B and C; OLR and zonal stretching deformation averages: box A).

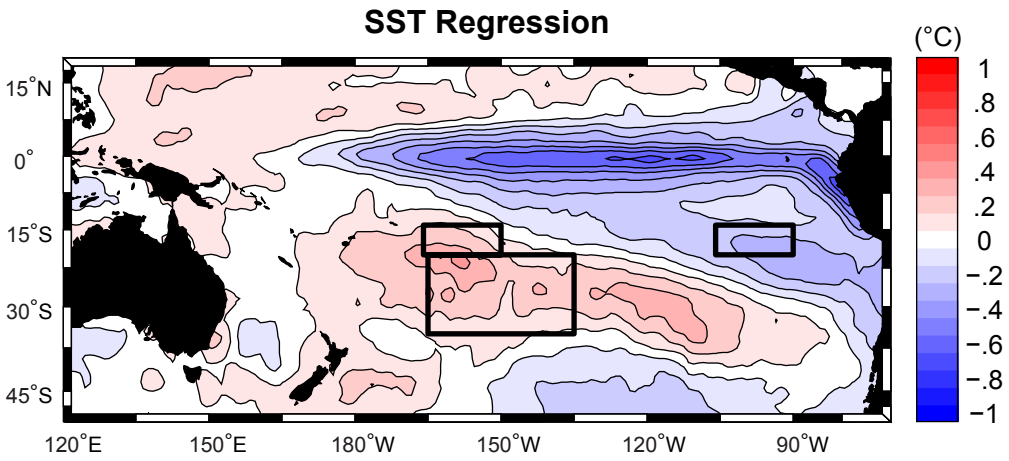

Figure 5.11: Linear regression of the standardized SST index (from Figure 5.10) onto monthly SST anomalies during DJF (1982-2008). The linear trend of the SST index has been removed. Black boxes denote averaging regions ("A", "B", and "C") described in Chapter 2.

(La Niña) events. These variations are out-of-phase with the SST index. Seasons experiencing an above average SST gradient typically exhibit stronger convection (lower OLR) and stronger zonal stretching deformation near the diagonal SPCZ. During El Niño periods (reduced SST gradient), OLR is higher and $\partial\overline{U}\big/\partial x$ is less negative. Interestingly, the OLR index appears to show no long-term linear trend, although $\partial\overline{U}\big/\partial x$ does become increasingly negative as the SST gradient increases. The correlation between seasonally averaged SST gradients and 200 hPa $\partial\overline{U}\big/\partial x$ is -0.33. The SST correlation with OLR is also negative and slightly larger (r = -0.43). A statistically significant positive correlation at the 95% level (assuming 27 independent DJF averages for the period 1982-2008) between seasonally averaged OLR and 200 hPa $\partial\overline{U}\big/\partial x$ (r = 0.52) was found, suggesting a significant decrease in OLR (i.e., stronger subtropical SPCZ) when $\partial\overline{U}\big/\partial x$ becomes more negative.

Recently, several studies have categorized different types of ENSO events based on spatial distributions of SST (e.g., Larkin and Harrison 2005; Ashok et al. 2007; Kao and Yu 2009; Kug et al. 2009) and investigated how the location of equatorial heating anomalies force teleconnections with other regions (Weng et al. 2007; Kim et al. 2009). Larkin and Harrison (2005) identified warming events in the central equatorial Pacific that differ from

the canonical El Niño, which is essentially warming of the East Pacific cold tongue and often cooling in the adjacent subtropics. SST anomalies during central Pacific warming events are smaller than East Pacific events, but set against a higher background SST and possibly more conducive to formation of deep convection (Kim et al. 2009). Interestingly, central Pacific warming events have become more prevalent in recent decades (Kug et al. 2009), but a dynamical explanation for the evolving ENSO characteristics remains elusive (Kim et al. 2009).

Weng et al. (2007) investigated how tropical precipitation patterns respond to different types of El Niño events; however, limited work has been done to understand the SPCZ's response to varying spatial patterns of equatorial heating. As previously discussed, the idealized SST experiment indicated that the large-scale circulation is clearly forced by the zonal SST gradient in the Pacific (Figures 5.4-5.6d). In that experiment, the Pacific SST field was altered everywhere between 61°N/S and large heating anomalies were imposed both near the equator and in the subtropics. A remaining question then is whether the SPCZ is more sensitive to equatorial or subtropical zonal temperature gradients. Interannual SST variability in the tropical and subtropical Pacific is closely associated with the equatorial SST variability (Figure 5.11), yet the off-equatorial zonal temperature gradient does not respond uniformly during every El Niño (Figure 5.10a). These caveats merit further analysis of the ENSO-SPCZ relationship.

To determine how the SPCZ responds to each type of ENSO, we first classify ENSO events by the location and sign of seasonal SST anomalies (Table 2). We follow the classification methodology of Kug et al. (2009), but restrict focus to only ENSO events occurring since 1982 and during DJF, when the SPCZ is most active, to correspond with the South Pacific climatology presented earlier. The center column of Table 2 contains the Oceanic Niño Index (ONI) which is a commonly used indicator of relative ENSO strength (positive values indicate warming in the Niño 3.4 region: 120°W-170°W). However, for El Niño events concentrated in only the eastern or central Pacific, the Niño 3 or Niño 4 indices

provide a more accurate description of the respective heating anomalies. (The ONI and the Niño 3 and 4 indices are defined in Appendix A.5.) SST anomalies, either warm or cool ENSO events of a variety of intensities, may also occur simultaneously in the central and eastern Pacific. For these "mixed" warming or cooling events, the ONI provides a representative intensity measurement (Kug et al. 2009).

Table 2: Classification of ENSO events by location of warming or cooling (Kug et al. 2009) and SST anomalies defined by the Oceanic Niño Index (ONI: Niño 3.4), Niño 3 (Eastern Pacific Warming), and Niño 4 (Central Pacific Warming) during DJF. Indices are described in Appendix A.5. Case studies of the respective classifications are indicated by an asterisk.

Type of ENSO event	**DJF season**	**ONI (Niño 3.4)**	**Niño 3**	**Niño 4**
Eastern Pacific Warming	1982/83 1997/98*	2.3 2.3	3.1 3.2	
Central Pacific Warming	1990/91 1994/95* 2002/03 2004/05 2006/07	0.4 1.2 1.2 0.7 0.8		0.8 1.1 1.1 1.0 0.9
"Mixed" Warming	1986/87 1987/88 1991/92*	1.2 0.7 1.8		
La Niña (typically "Mixed" Cooling)	1984/85 1988/89 1995/96 1998/99* 1999/00 2000/01 2007/08	-0.9 -1.7 -0.7 -1.4 -1.6 -0.6 -1.4		

Comparison of Table 2 with Figure 5.10a helps clarify the convoluted relationship between ENSO and the zonal SST gradient. As expected, the SST index was well below the trend line during both El Niño events confined to the East Pacific, while the gradient was above normal during almost every La Niña (except 2007/08). However, a less consistent

relationship is evident between the SST index and ENSO for the central Pacific and mixed warming events. The zonal SST gradient was larger than normal during 3 out of 5 central Pacific warming events and below normal for 2 out of 3 seasons with warming conditions mixed over the central and East Pacific. Warming in the central equatorial Pacific may sometimes be associated with an enhanced zonal SST gradient near the SPCZ, more commonly associated with La Niña. It is also apparent from Table 2 that SST anomalies were mostly confined to the East Pacific during the two strongest El Niño events (1982/83 and 1997/98), while the three most recent El Niños have been central Pacific events of moderate intensity.

Composites of SST, OLR, and 200 hPa zonal wind are computed for each of the DJF seasons listed in Table 2. Figures 5.12-5.15 show one example of each ENSO classification, though the examples are generally representative of other events within their similar classification. Overlaid on each composite is the 240 W m^{-2} OLR contour from the 1982-2008 period, providing a reference of the climatological SPCZ location. Considering first the SSTs of each case study (top panel in each figure), it is clear that the largest temperature anomalies almost always occur equatorward and east of the SPCZ. SST anomalies are also present in the subtropics, but usually are of the opposite sign of equatorial anomalies. Together, temperature anomalies are often arranged in meridional dipole patterns and SSTs in the subtropics appear closely related to the tropics. Cooling occurs poleward of the largest equatorial warming during El Niño, with SSTs decreasing within the climatological SPCZ boundary (Figures 5.12-5.14). During La Niña (Figure 5.15), the dipole pattern is reversed and SSTs warm in the subtropics around the SPCZ. Typically, the zonal SST gradient east of the SPCZ (box B minus C) decreases during El Niño and increases during La Niña; however, this relationship does not always hold and SSTs anomalies in each box can sometimes be minimal (e.g., during the 1994/95 central Pacific warm event).

In the tropics, SST anomalies and convection are mostly collocated with negative OLR anomalies typically located over waters warmer than climatology. The ENSO composites

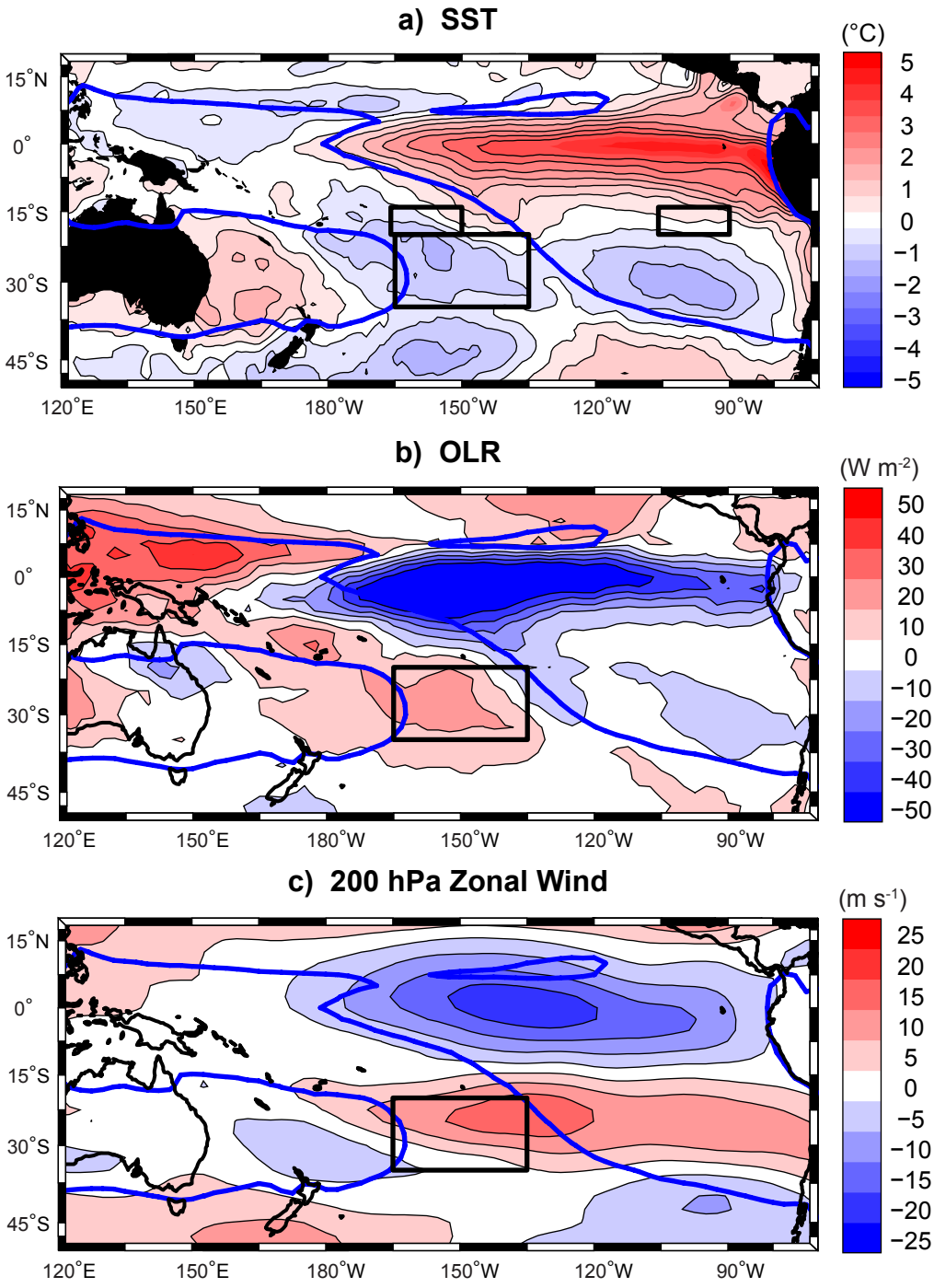

Figure 5.12: A case study of an eastern Pacific warm event (1997/98 El Niño). Anomalies from the 1982-2008 DJF climatology are shown for (a) SST (°C), (b) OLR (W m^{-2}), and (c) 200 hPa zonal winds (m s^{-1}). Black boxes denote averaging regions ("A", "B", and "C") described in Chapter 2. 240 W m^{-2} OLR contour outlined by blue lines.

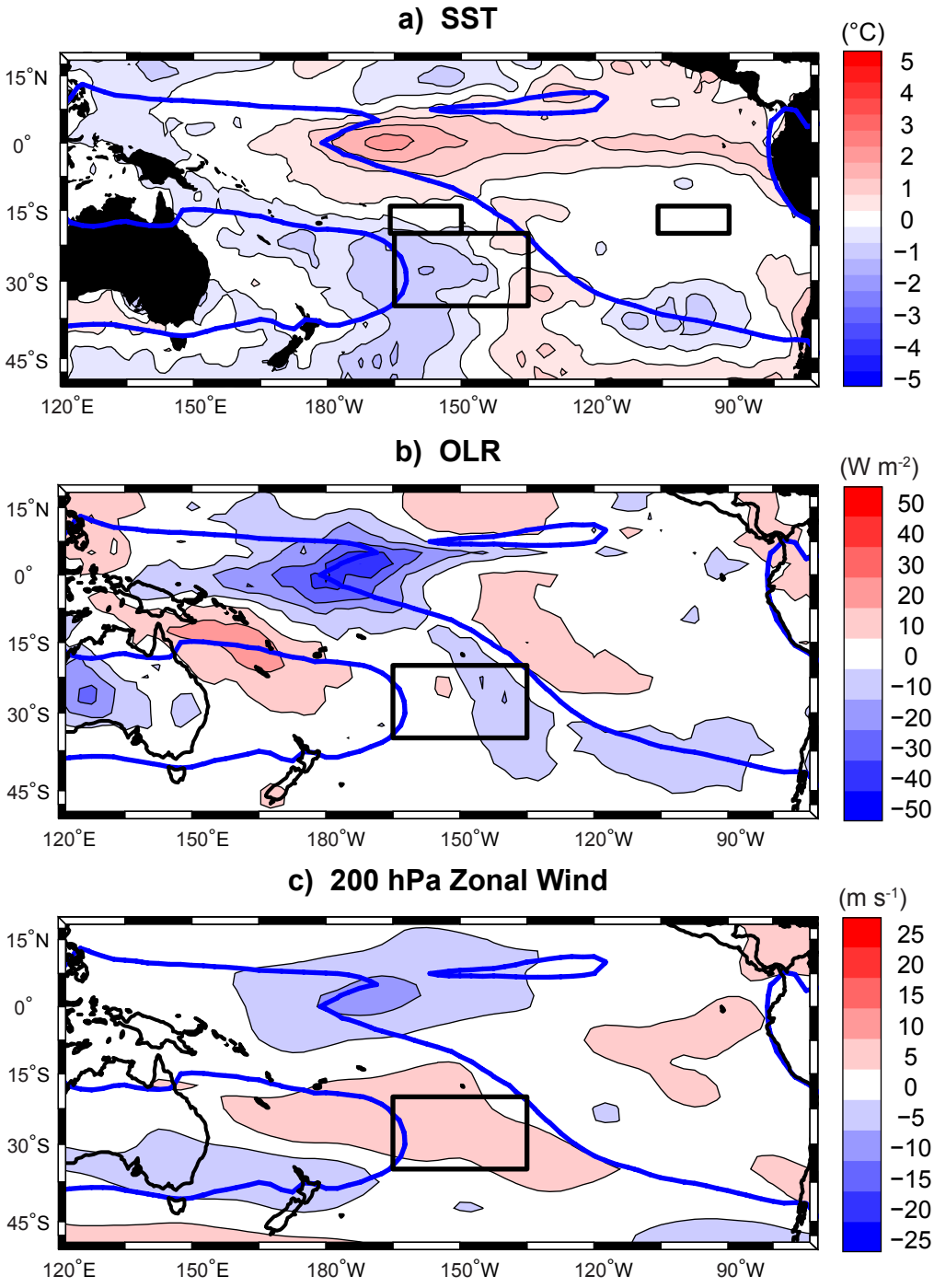

Figure 5.13: Same as Figure 5.12, but for a central Pacific warm event (1994/95 El Niño).

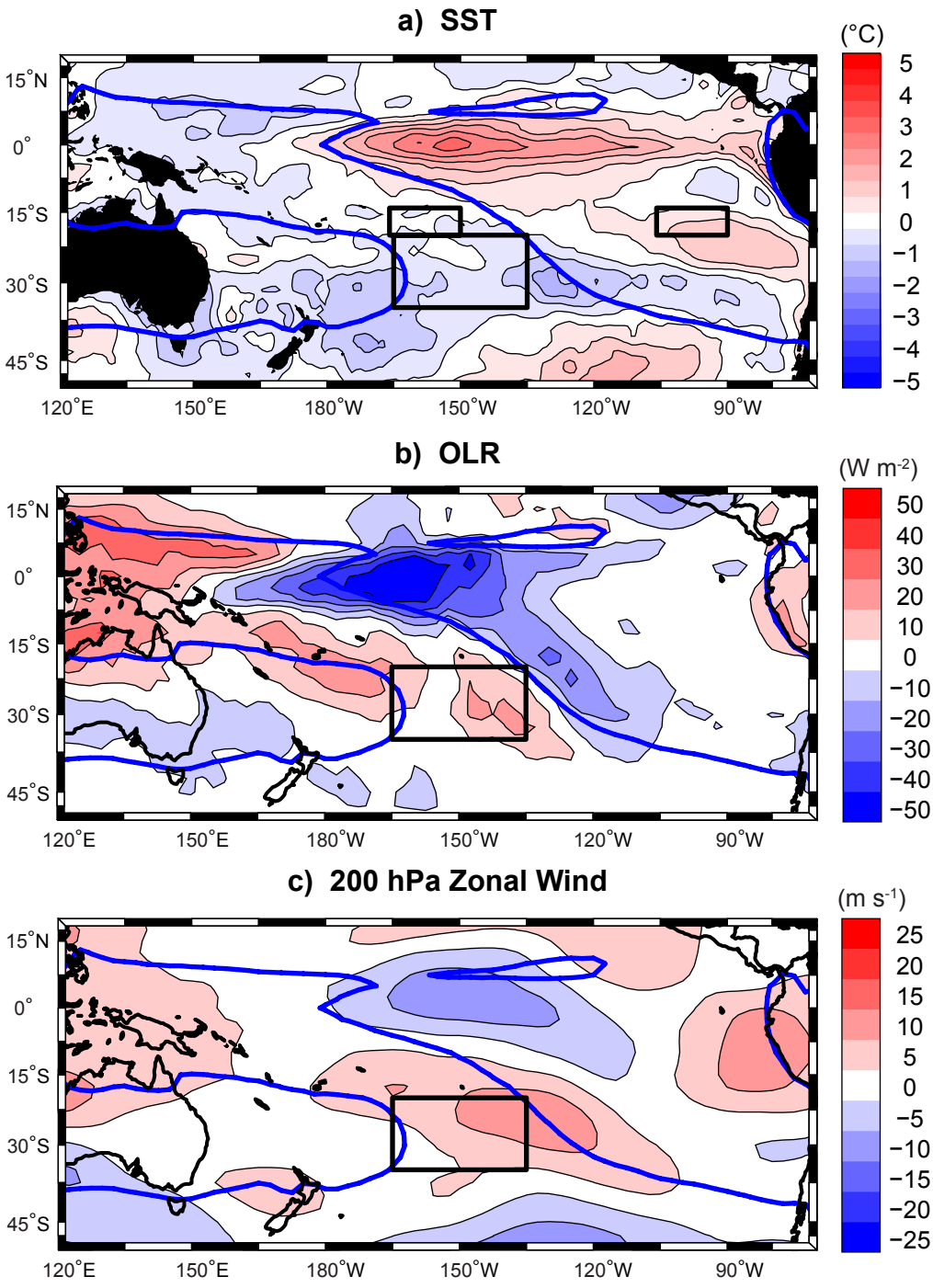

Figure 5.14: Same as Figure 5.12, but for an eastern and central Pacific "mixed" warm event (1991/92 El Niño).

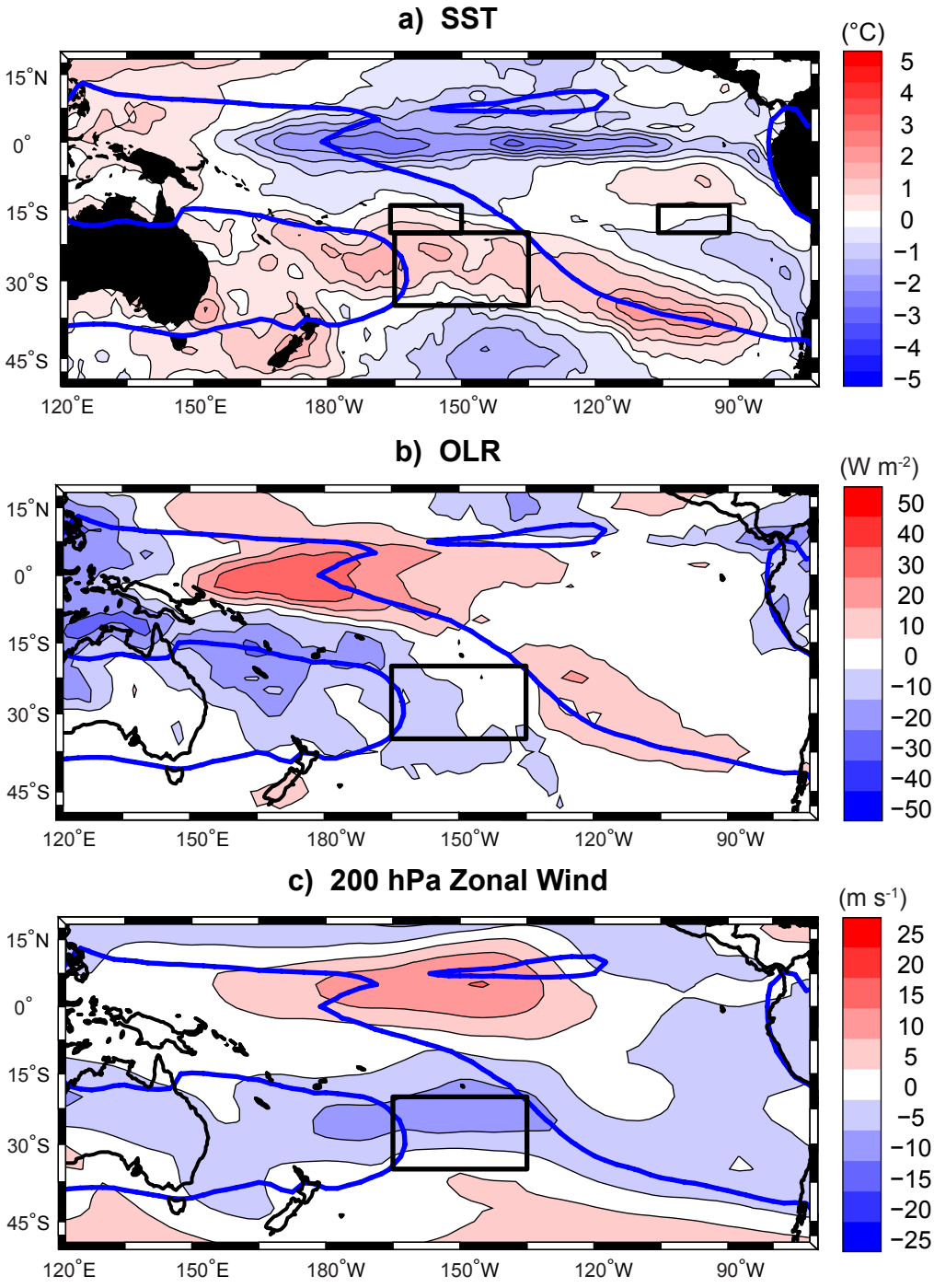

Figure 5.15: Same as Figure 5.12, but for a "mixed" Pacific cool event (1998/99 La Niña).

reveal a more complex SST and OLR relationship in the subtropics, especially near the SPCZ. During the 1997/98 eastern Pacific warm event (Figure 5.12), the ocean surface cooled throughout most of the SPCZ and in the East Pacific, away from the equator. Convection decreased in the SPCZ region enclosed by the 240 W m^{-2} OLR climatology, yet OLR values decreased over both the warmer equatorial waters and the anomalously cool subtropical East Pacific. The northeastward shift of convection is the canonical SPCZ response to El Niño. A similar OLR pattern is noted when equatorial warming extends from the East Pacific towards the Dateline ("mixed" warm event: Figure 5.14), while SST and OLR patterns are basically inversed during La Niña (Figure 5.15). During the 1998/99 La Niña, convection decreases along the eastern boundary of the SPCZ, even in the subtropics where SSTs warmed by over 1°C.

Analysis of the central Pacific warm event (Figure 5.13) further suggests complexities in the ENSO-SPCZ relationship. During the 1994/95 El Niño, SSTs decreased throughout most of the diagonal SPCZ except along the eastern boundary where the sea surface warmed slightly. SST anomalies elsewhere in the subtropics were negligible and the zonal SST gradient index (Figure 5.10a) was just slightly below average. Within most of the SPCZ poleward of 15°S, convection was similar to climatology despite cooler SSTs, while OLR decreased by about 10 W m^{-2} in the eastern half of box A. Convection in the diagonal SPCZ during the central Pacific warm event was perhaps supported by a robust zonal SST gradient, especially east of 150°W, and associated long wave circulation.

Numerous previous studies (e.g., Trenberth 1997) have noted easterly wind anomalies in the upper troposphere during El Niño, collocated with enhanced equatorial convection. The 200 hPa westerly wind duct weakens or dissipates completely during these periods. Each warming case study (Figures 5.12-5.14) shows a weakening of the westerly wind duct, while the La Niña case (Figure 5.15) shows anomalously strong equatorial westerlies. The opposite sign of zonal wind anomalies is apparent in the subtropics. During El Niño, the subtropical jet becomes stronger and shifts equatorward (a weaker jet is noted during

La Niña); however, westerly wind anomalies are not uniform across the South Pacific. In general, the greatest enhancement of the subtropical jet occurs at the same longitude of maximum equatorial heating and convection.

Placement of westerly wind anomalies in the subtropics has important consequences for the orientation and strength of the SPCZ. For example, increased westerlies in box A result in less negative zonal stretching deformation at that location, but stretching deformation remains negative to the east. During the East Pacific warming event (Figure 5.12), the jet stream strengthened in the diagonal section of the SPCZ and convection decreased. OLR decreased just to the east of that region, where $\partial\overline{U}\big/\partial x$ was more negative. As noted above, convection in the SPCZ strengthened during the 1994/95 El Niño (Figure 5.13). Westerly wind anomalies during 1994/95 were atypically far west for a warming event, with convection most concentrated just east of the westerly wind anomalies. During La Niña, the subtropical jet weakens in the SPCZ and convection increases there and to the west, where $\partial\overline{U}\big/\partial x$ is the most negative.

To summarize the observed relationship of the SPCZ with ENSO, convection is closely correlated with local SST anomalies in the tropics but, in the higher latitudes, convection is more related to large-scale circulation changes. For each case study, OLR in the diagonal region of the SPCZ is dependent on the strength and location of the subtropical jet stream which influences where negative zonal stretching deformation, and hence convection, occurs.

5.2.2 Numerical experiments

The SST anomaly patterns shown in Figures 5.12-5.15 are each associated with a different type of ENSO event, and each pattern consists of a complex structure of latitudinal and longitudinal temperature variations. SST anomalies vary longitudinally across the SPCZ and across the entire Pacific. Often, the sign of SST anomalies in the subtropical SPCZ are opposite the adjacent equatorial heating or cooling and together form a dipole pattern.

Complex ENSO SST patterns make it difficult to determine from case studies whether equatorial heating anomalies, rather than anomalies in the subtropics, more directly force variability of the SPCZ. Previously, we examined the SPCZ response to removal of the zonal SST gradient over the entire Pacific basin (61°N-61°S), but here we examine a series of numerical experiments with surface heating anomalies restricted to near the equator.

Table 3 lists four experiments ("EPAC Warming", "CPAC Warming", "MIXED Warming", and "EPAC Cooling") designed to simulate each type of ENSO event identified in the previous observational case studies. Imposed equatorial heating anomalies ranging from +3°C to -3°C, chosen to approximate strong to weak El Niños or La Niña conditions, are added to the observed monthly varying annual cycle of SSTs. Each experiment is configured, initialized, and integrated for 26 years (of which a spin up period of 2 years is discarded) according to the methodology used to obtain a climatology of the Control simulation (Chapter 3.2) and the idealized numerical experiments discussed previously (Table 1). Departures from the Control simulation during DJF are shown in Figures 5.16-5.19.

Table 3: Description of controlled ENSO experiments using the ICTP AGCM. SST heating anomalies are applied to various locations of the equatorial Pacific to simulate different types of ENSO events. Heating anomalies are tapered by half (temperatures in parentheses) in a buffer extending to 9.25°N/S and an additional 3.75°E/W.

Experiment	Location	Heating Anomaly
EPAC Warming	Niño 3 (5.5°N-5.5°S, 150°W-93.75°W)	+3°C (+1.5°C)
CPAC Warming	Niño 4 (5.5°N-5.5°S, 157.5°E-153.75°W)	+1°C (+0.5°C)
MIXED Warming	Niño 3+4 (5.5°N-5.5°S, 157.5°E-93.75°W)	+1.5°C (+0.75°C)
EPAC Cooling	Niño 3 (5.5°N-5.5°S, 150°W-93.75°W)	-3°C (-1.5°C)

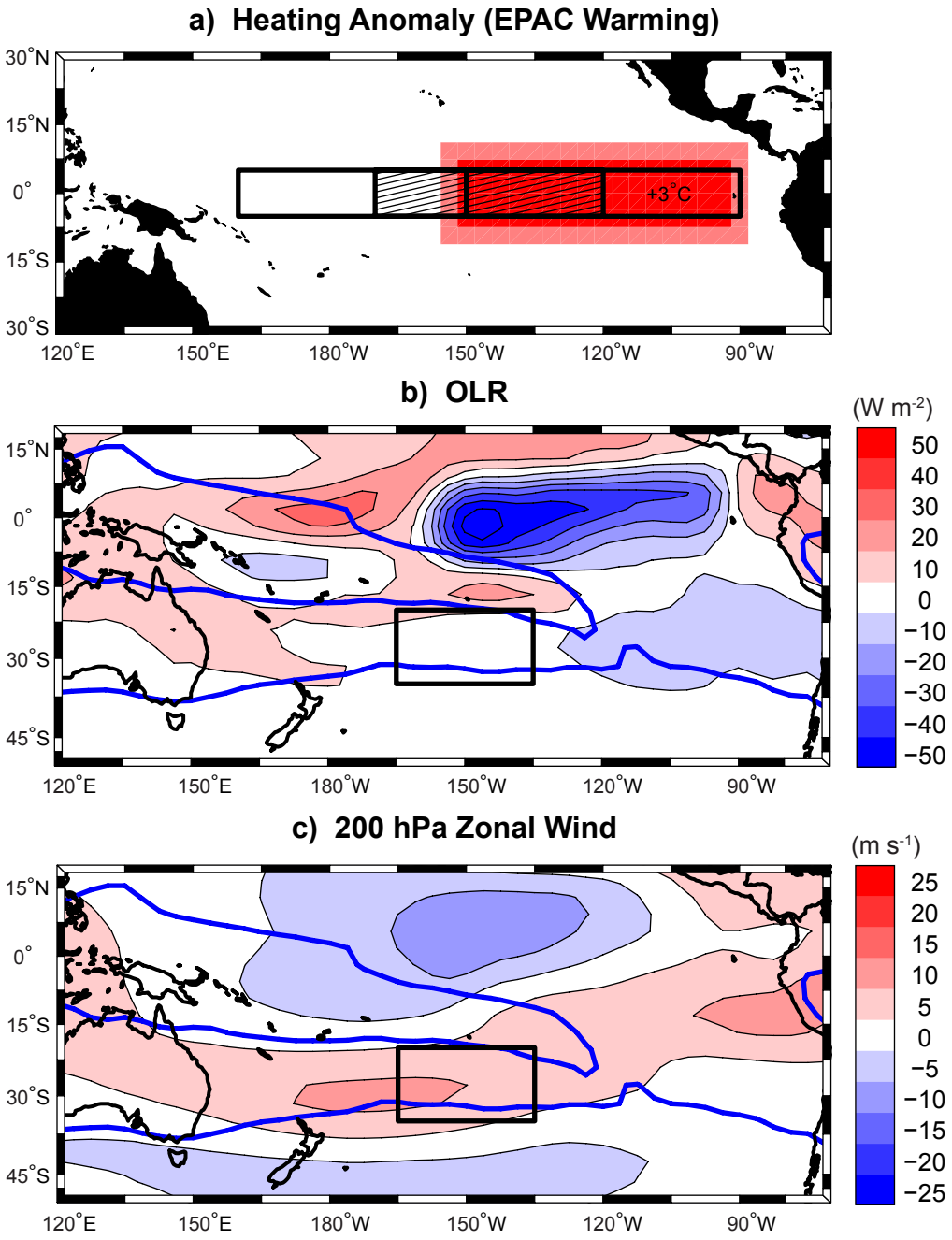

Figure 5.16: EPAC Warming Experiment: (a) Heating anomaly (°C) as described in Table 3. Right, middle hatching, and left boxes enclose the Niño 3, 3.4, and 4 averaging regions. (b and c) DJF climatology (24 seasons) of simulated OLR (W m^{-2}) and 200 hPa zonal wind (m s^{-1}), respectively. Departures from the Control simulation are shown. Black boxes correspond to the OLR averaging box A described in Chapter 2. The 240 W m^{-2} OLR contour from the Control experiment is outlined by blue lines in each panel.

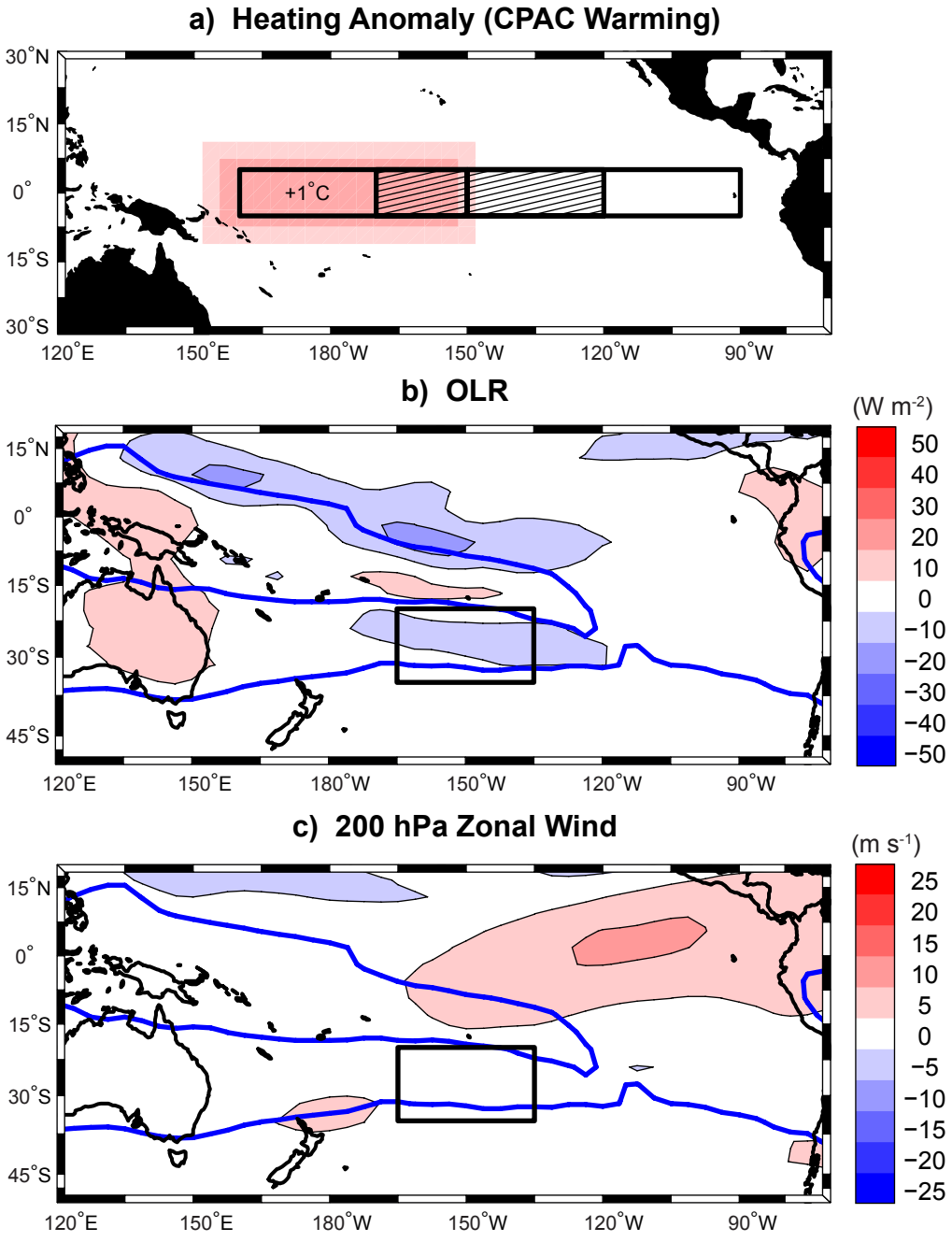

Figure 5.17: Same as Figure 5.16, but for the central Pacific warming experiment.

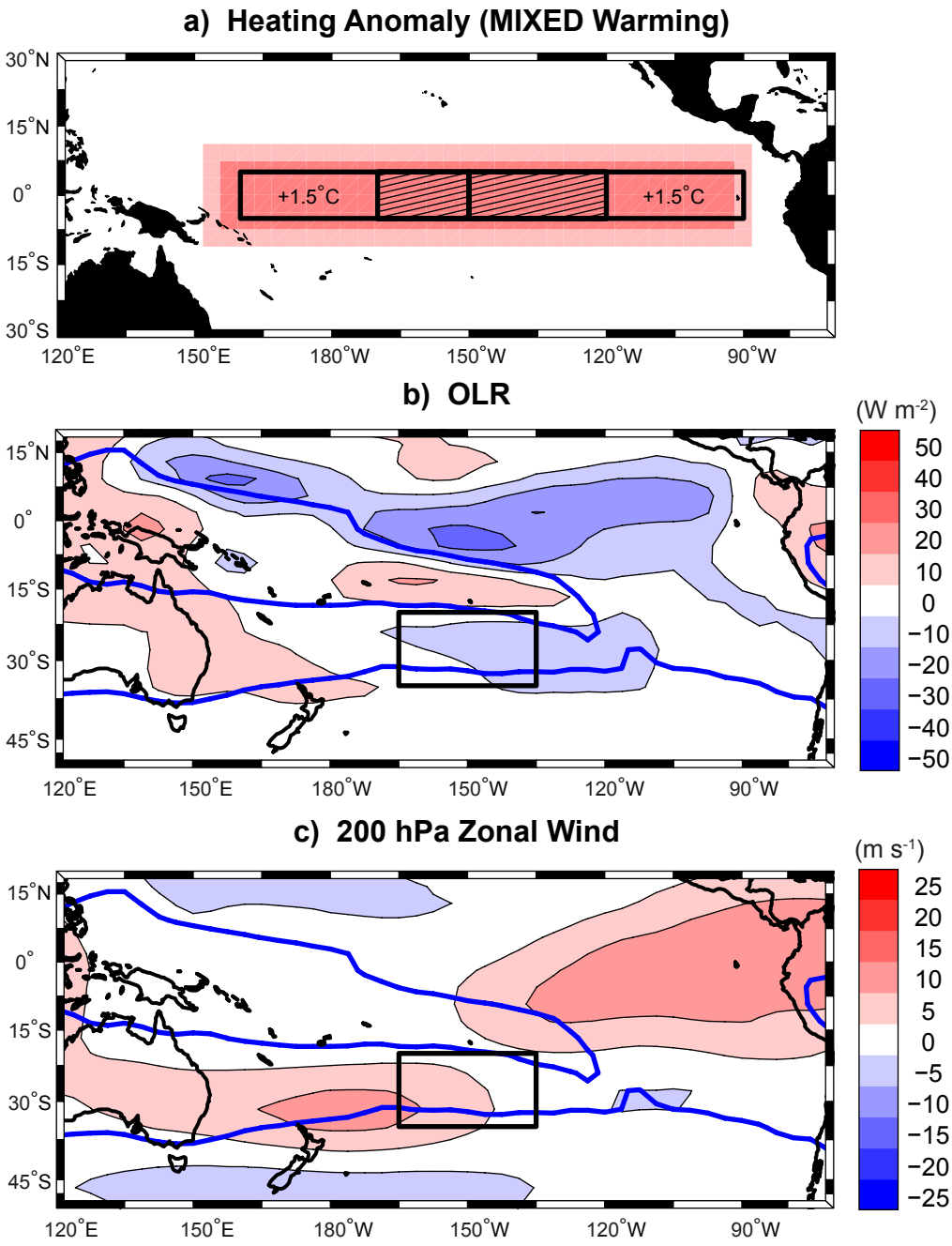

Figure 5.18: Same as Figure 5.16, but for the eastern and central Pacific "mixed" warming experiment.

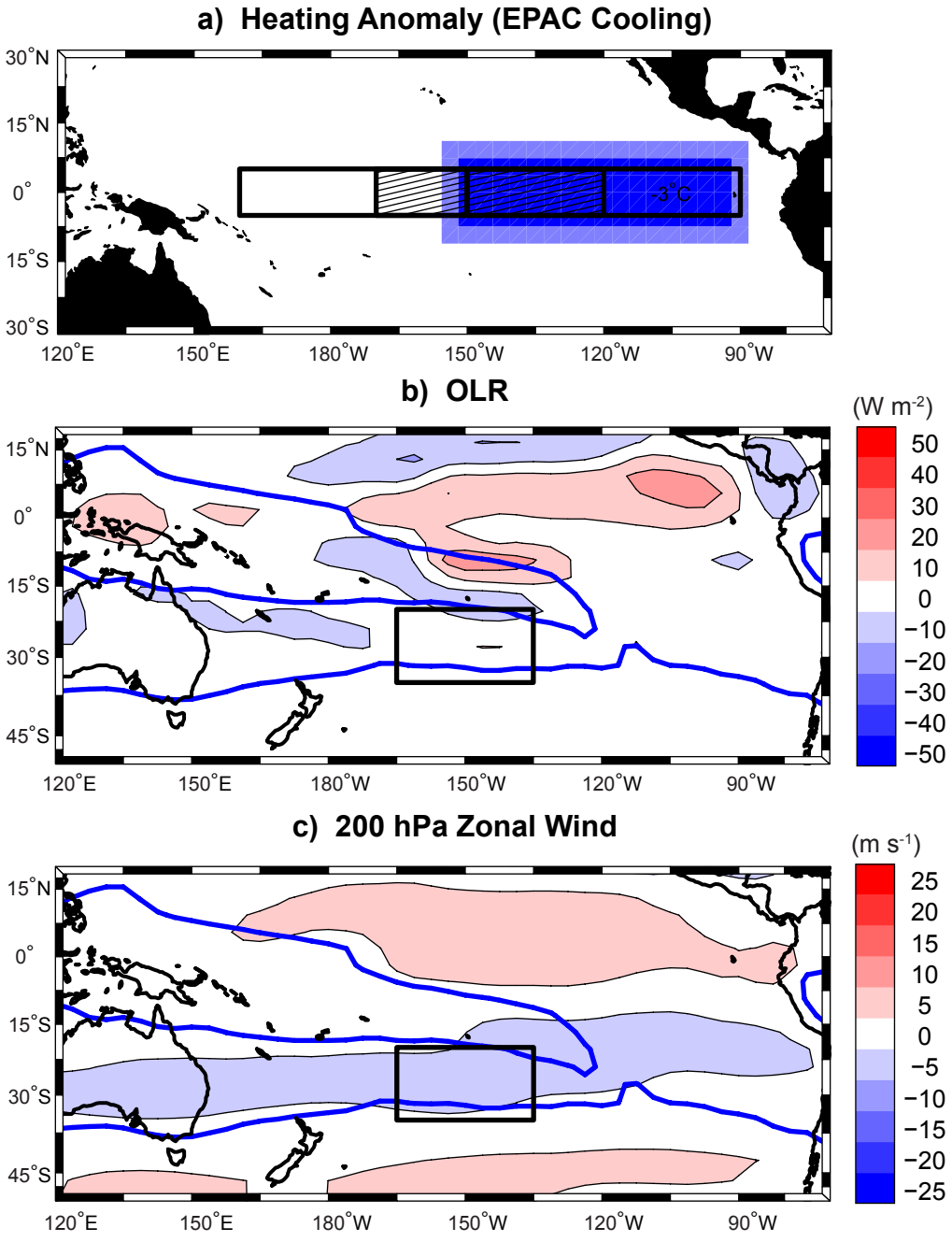

Figure 5.19: Same as Figure 5.16, but for the eastern Pacific cooling experiment.

Examining the four ENSO-like simulations (Figures 5.12-5.14), we see that OLR in the tropics responds to equatorial SST anomalies in a manner similar to observations. Near the location of heating or cooling, convection increases in every El Niño simulation but decreases in the La Niña experiment. Simulated 200 hPa zonal wind anomalies near the equator also are similar to case study observations; however, westerly wind anomalies associated with the subtropical jet extend too far into the tropics. While in the subtropics, OLR and zonal wind anomalies are much smaller than observed ENSO composites. Subtropical anomalies are especially small for the CPAC Warming and EPAC Cooling experiments (Figures 5.17 and 5.19, respectively). In the EPAC and MIXED Warming experiments (Figures 5.16 and 5.18, respectively) subtropical OLR anomalies are also small, but typically negative downstream of westerly wind anomalies. Convection tends to increase in regions where $\partial\overline{U}\big/\partial x$ becomes more negative, such as box A in the MIXED Warming experiment. Interestingly, $\overline{U}$ anomalies during the EPAC and MIXED Warming simulations have a westward bias, compared to their respective case studies, and are instead similar to observations during central Pacific warming events (e.g., the 1994/95 El Niño).

Previously, we saw from Figure 5.4d that the simulated SPCZ disappears completely when the Pacific zonal SST gradient is removed. In that idealized experiment, regions of $\partial\overline{U}\big/\partial x < 0$ are mostly eliminated in the South Pacific between 20°S-35°S (Figure 5.7c). The SPCZ response is weaker in the ENSO experiments, where SST anomalies are restricted to near the equator. While the equatorial heating anomalies clearly force substantial differences in the tropics, more subtle forcings exist in the subtropics. Figure 5.20 provides a comparison of meridionally averaged (20°S-35°S) OLR and $\partial\overline{U}\big/\partial x$ for each ENSO experiment with the Control simulation. A region of $\partial\overline{U}\big/\partial x < 0$ (gray shading) and low OLR is maintained in the central South Pacific for every ENSO experiment. In fact, the subtropical SPCZ hardly responds to the EPAC Cooling experiment, while regions of negative zonal stretching deformation and low OLR only shift slightly east in the warming experiments.

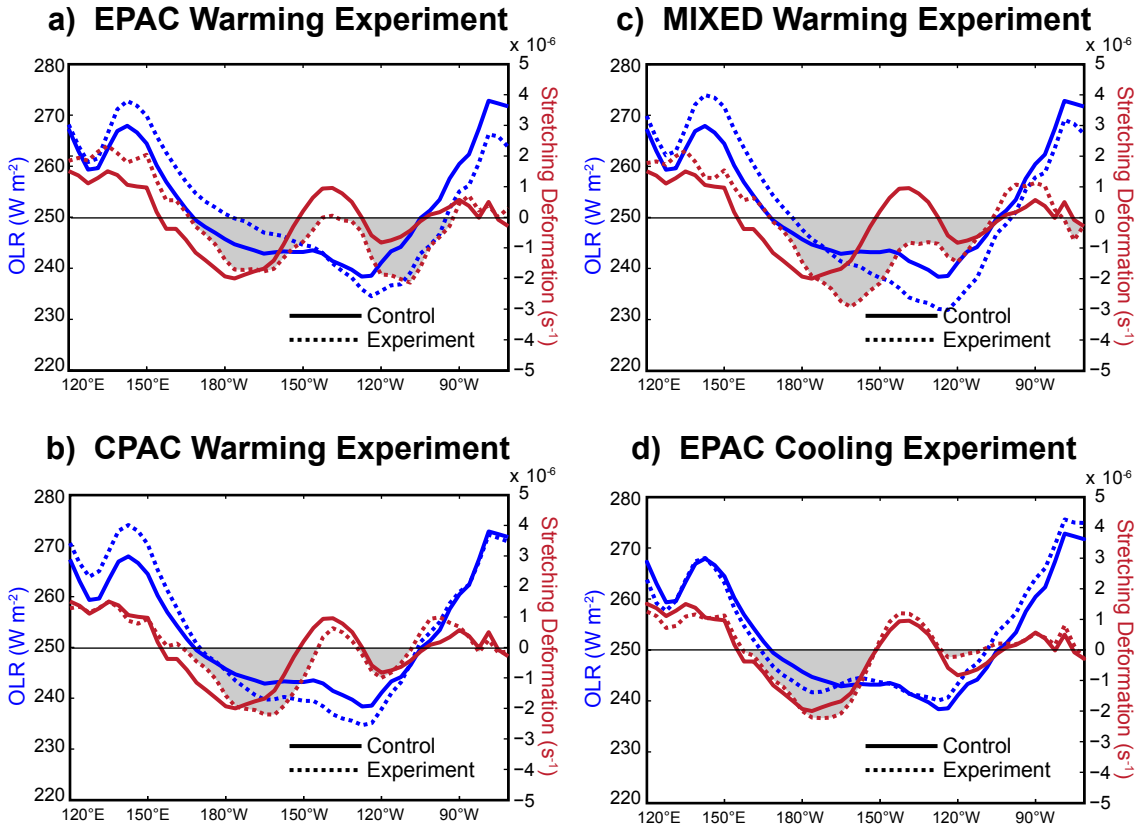

Figure 5.20: DJF climatology (24 seasons) of simulated OLR (blue) and 200 hPa zonal stretching deformation (red) for the (a) EPAC Warming, (b) CPAC Warming, (c) MIXED Warming, and (d) EPAC Cooling experiments. Solid lines indicate values from the Control experiment. Averaging is done over a 15° latitude band (20°S-35°S). Gray shading depicts regions of negative zonal stretching deformation from each respective experiment.

Results of the ENSO experiments vary from the observational case studies in the subtropics. Comparison of the modeling experiments with observations suggests that features of the large-scale circulation forced by ENSO, such as the longitudinal location of maximum zonal winds in the subtropics, are governed partly by off-equatorial heating patterns. SST anomalies poleward of 5.5°N/S were deliberately tapered to zero in the numerical simulations. For each experiment and case study, however, OLR decreased in the subtropics in regions where $\partial\overline{U}\big/\partial x$ became more negative. In summary, the coherent interannual changes in the SST, the resultant influence on the background circulation, and the consequent migration of the SPCZ in observations and simulations offer support for the hypothesis that these three processes are related.

5.3 Synoptic and composite analyses

From the longitude-time case study of meridionally averaged OLR (Figure 5.1) at the beginning of this chapter, we noted that convection is frequent in the subtropics over each of the Southern Hemisphere oceans at certain longitudes. The lowest OLR occurs in the South Pacific where $\partial\overline{U}\big/\partial x$ is also the most negative. A similar relationship between convection and negative zonal stretching deformation is evident in the AGCM experiments.

We now use OLR temporal filtering methods to more clearly track the synoptic disturbances which were shown in Figure 2.2d to significantly influence the diagonal region of the SPCZ. The entire 1982-2008 observed OLR time series is passed through a 3-6 day Lanczos filter with 241 weights (Duchon 1979); however, just the 2005-2006 DJF season is shown in Figure 5.21. Meridional averaging is again done over the 20°S-35°S latitude band. From Figure 5.21 we see that synoptic disturbances mostly propagate from west to east, but with varying phase speeds. Disturbances occasionally slow, but rarely propagate westward. We also clearly see amplified OLR anomalies organized in three bands, corresponding with the climatological locations of the three Southern Hemisphere convergence zones. Away from these longitudes, convective anomalies are smaller and disturbances

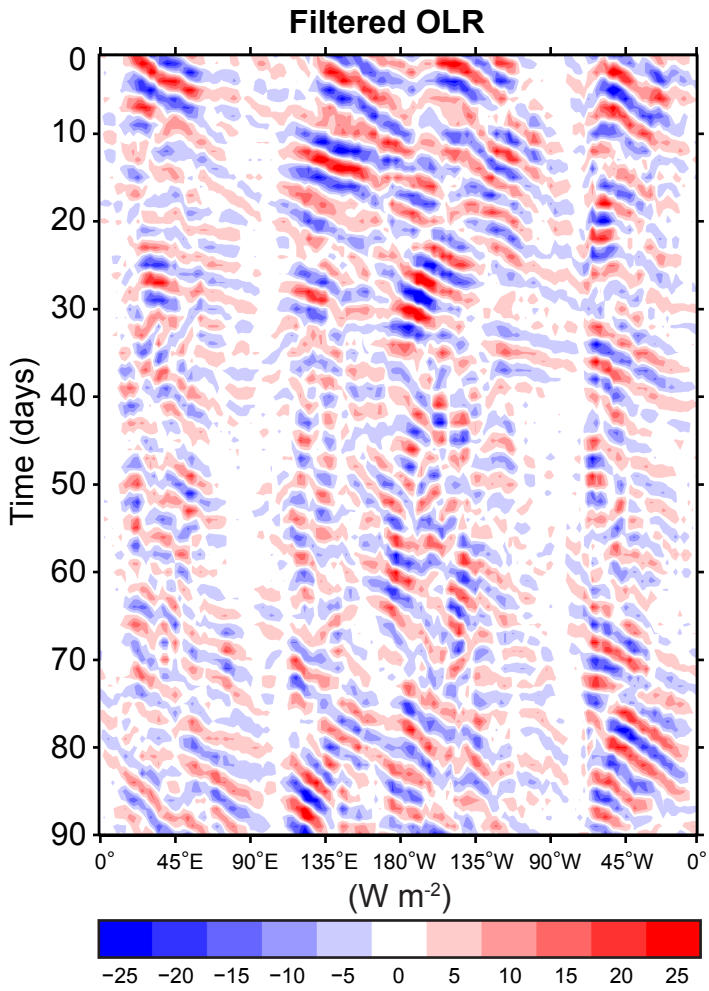

Figure 5.21: Hovmoller (longitude-time) of observed 3-6 day filtered OLR (W m^{-2}) during 1 December 2005 to 28 February 2006. Averaging is done over a 15° latitude band (20°S-35°S).

often propagate more quickly, at least during this case study.

Figure 5.22 presents a comparison of disturbances which pass through the eastern boundary of mean deep convection in the diagonal SPCZ (30°S, 135°W) with wave characteristics in the adjacent Southeast Indian (30°S, 105°E) and Southeast Pacific (30°S, 90°W) basins. The latter two regions are characterized by minimal convection and positive zonal stretching deformation according to climatology (Figure 5.1b) and are located away from the Southern Hemisphere convergence zones. OLR time series from each basin are passed

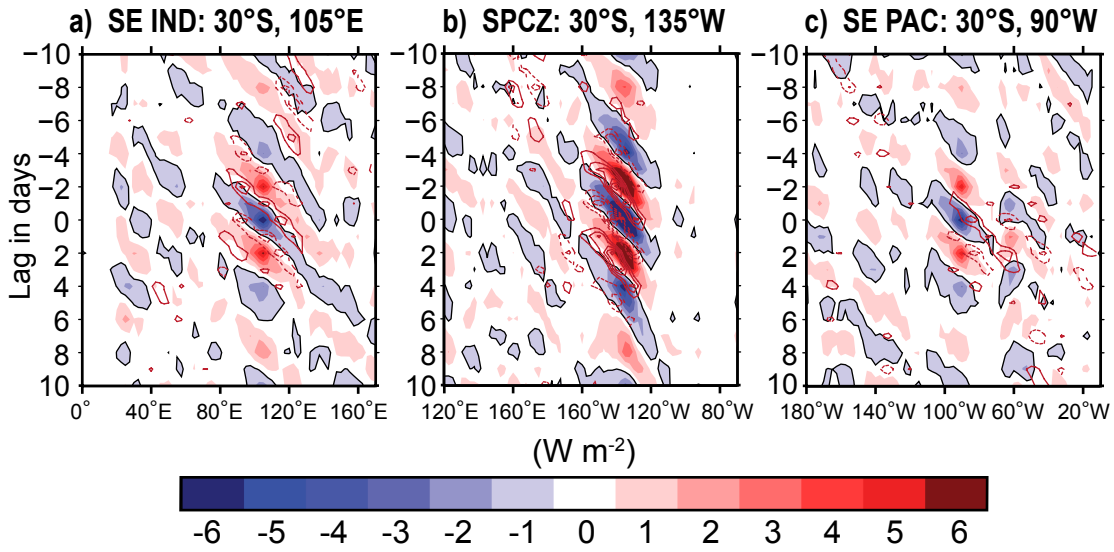

Figure 5.22: (a) Hovmoller (longitude-lag) of OLR (W m^{-2}, shading, -1 W m^{-2} contour outlined) and 200 hPa zonal stretching deformation (s^{-1}, contours) regressions at 30°S for a 3-6 day filtered OLR base point at 30°S, 105°E (Southeast Indian basin). Zonal stretching deformation contour interval: $2x10^{-7}$ s^{-1}; starting at $\pm 4x10^{-7}$ s^{-1}. Solid (dashed) lines depict negative (positive) anomalies. (b and c) Same as (a) but for base points at 30°S, 135°W (SPCZ) and 30°S, 90°W (Southeast Pacific basin), respectively.

through the same 3-6 day Lanczos filter described above and then scaled by the standard deviation of the respective time series to compute OLR and $\partial\overline{U}/\partial x$ linear regressions. These regressions track synoptic-scale Rossby waves more clearly than the longitude-time diagram of unfiltered data (Figure 5.1a) and are statistically more robust than the longitude-time case study of one season of filtered data (Figure 5.21).

Table 4 provides a comparison of wavelength (km), phase speed (m s^{-1}), and period (days) of synoptic wave characteristics derived from OLR regression anomalies in the SPCZ with those over the adjacent Southeast Indian and Southeast Pacific basins. Each regression depicts a period of 4-5 days, as expected when applying a synoptic (3-6 day) filtering method to subtropical OLR time series. Different phase speeds and spatial scales are observed with disturbances near the SPCZ being noticeably slower, and having shorter

wavelengths, than those over neighboring basins. From Figure 5.22a, "fast" waves are observed over the Southeast Indian Ocean with phase speeds of about 10.8 m s^{-1} and wavelengths of about 4,000 km. Regressions from the SPCZ base point depict "slow" waves with phase speeds and wavelengths of about 7.8 m s^{-1} and 3,000 km, respectively. OLR anomalies do not propagate east of 120°W often; however, regressions over the Southeast Pacific show sporadic convective anomalies with "fast" phase speeds (10.0 m s^{-1}) and "long" wavelengths (3,700 km) similar to those over the Southeast Indian Ocean. Results suggest that eastward phase speeds are typically divided between "fast regimes" in regions absent of deep convection (i.e., OLR > 240 W m^{-2}) and "slow regimes" in convective areas shaded in Figure 5.1a. Slowly propagating disturbances also have shorter wavelengths, while the periods of variability are similar in each region. This is not surprising as the frequency of the waves is conserved (Chapter 4).

Table 4: Synoptic-wave characteristics for Southeast Indian (30°S, 105°E), SPCZ (30°S, 135°W), and Southeast Pacific (30°S, 90°W) 3-6 day filtered OLR base points. Characteristics are derived from OLR regression anomalies in Figure 5.22.

Base Point	**Phase Speed (m s^{-1})**	**Wavelength (km)**	**Period (days)**
30°S, 105°E	10.8	4,000	4.3
30°S, 135°W	7.8	3,000	4.4
30°S, 90°W	10.0	3,700	4.3

Composite analyses, following the methodology of Serra et al. (2008), are constructed in order to examine more closely changes in the scale and propagation characteristics of waves moving into the diagonal SPCZ region. The regressions use the same 27 DJF seasons of daily data as used to construct the climatology in Chapter 2. Figure 5.23a shows a regression of unfiltered OLR (shading) and $\partial\overline{U}/\partial x$ (contours) between 120°E and 70°W based on a -20 W m^{-2} anomaly in 3-6 day filtered OLR at 30°S, 135°W for lags -10 to

10 days. Here, the longitude-lag regression is again performed for a base point at 30°S to optimize observations of OLR anomalies which propagate into the diagonal SPCZ region. Figure 5.23b-d shows longitude-latitude maps of the OLR and $\partial\overline{U}\big/\partial x$ regression for lags -2, 0, and 2 days.

The 135°W regressions (Figure 5.23a) show convective anomalies every three to five days, confirming that the Lanczos filtering method retains the correct time scale of synoptic modes of variability in the SPCZ. Set in a background climatological negative zonal stretching deformation region (Figure 5.1b), $\partial\overline{U}\big/\partial x < 0$ anomalies (solid contours) are observed to lead most of the OLR negative anomalies by about one day, or 5° of longitude. Trenberth (1991), in an analysis of Southern Hemisphere storm track activity, notes similar zonal wind anomalies around 30°S and ahead of vertical motion perturbations. By tracking the negative OLR signal westward from the base point (lag 0 days), anomalies exceeding -1 W m^{-2} (black contours) are observed to 170°W (lag -5 days). The same anomalous OLR continues eastward from the base point for about another five days, although only reaching 120°W. The composite disturbance propagates 35° of longitude during the first five days, then slows and amplifies around 135°W, and finally dissipates near the eastern SPCZ boundary.

Phase speeds become increasingly slower as disturbances propagate eastward through the SPCZ, perhaps responding to the background location of negative zonal stretching deformation. Table 5 provides a comparison of wave characteristics (indicated by $\partial\overline{U}\big/\partial x$ anomalies in Figure 5.23b-d) at different lags within the SPCZ. At lag 0 days, wavelength and phase speed are comparable to those derived from OLR anomalies in Figure 5.22b (Table 4). Table 5 confirms that wave characteristics change as disturbances propagate through the SPCZ. Wavelength shrinks from about 5,800 km to 1,300 km, while the phase speed decreases from 15.2 m s^{-1} to 3.5 m s^{-1}, between lags -2 and 2 days.

Assuming that propagation of OLR minima is representative of the group velocity (C_{gd}), Equation 11 can be used to predict a slowdown of C_{gd} where there is negative stretching

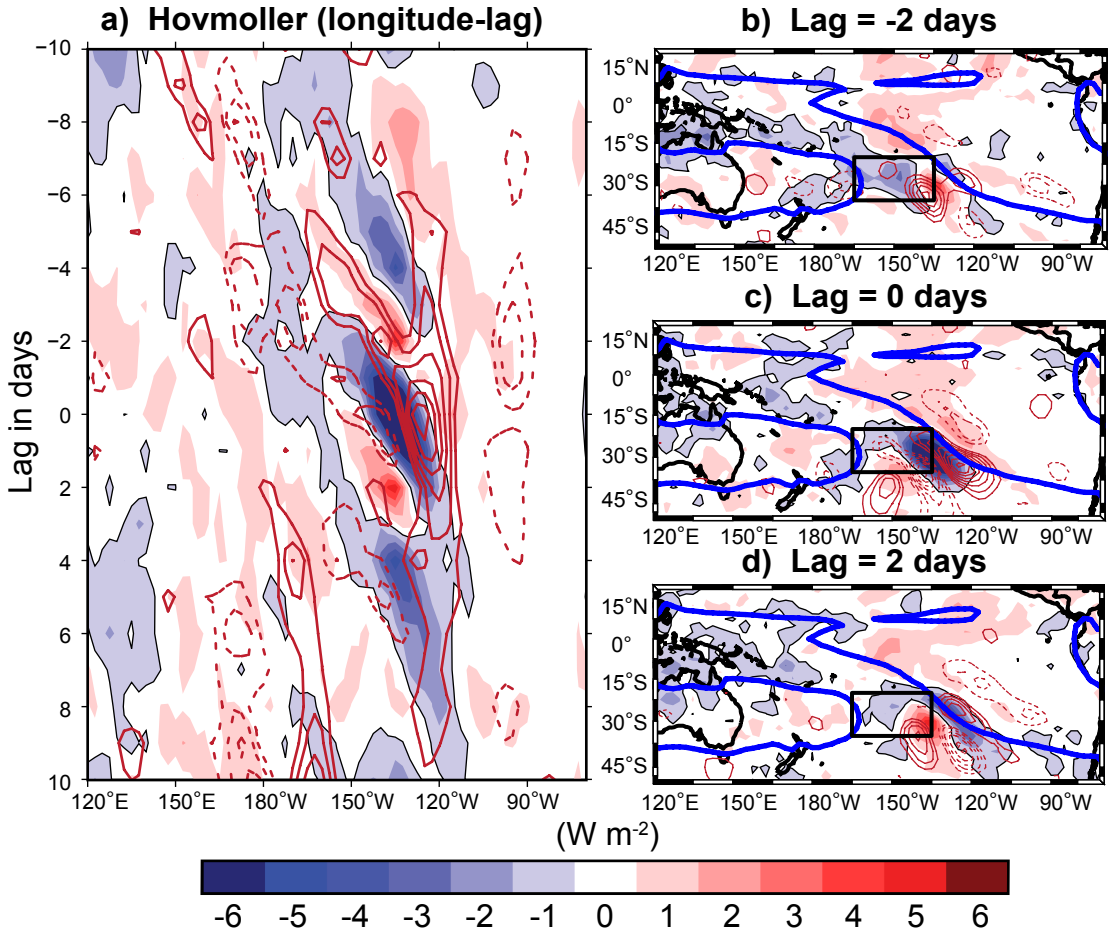

Figure 5.23: (a) Hovmoller (longitude-lag) of OLR (W m^{-2}, shading, -1 W m^{-2} contour outlined) and 200 hPa zonal stretching deformation (s^{-1}, contours) regressions at 30°S for a 3-6 day filtered base point (-20 W m^{-2} threshold) at 30°S, 135°W. Zonal stretching deformation contour interval: $2x10^{-7}$ s^{-1}; starting at $\pm 4x10^{-7}$ s^{-1}. Solid (dashed) lines depict negative (positive) anomalies. (b, c, and d) Same as (a) but for longitude-latitude regressions at Lags -2, 0, and 2 days, respectively. 240 W m^{-2} OLR contour (DJF climatology) outlined by blue lines.

Table 5: Synoptic-wave characteristics for a disturbance propagating through the SPCZ at Lags -2, 0, and 2 days. Characteristics are derived from $\partial\overline{U}/\partial x$ regression anomalies (Figure 5.23b-c) using the period of OLR variability at 30°S, 135°W (Table 4).

Base Point	Phase Speed ($m\ s^{-1}$)	Wavelength (km)	Period (days)
Lag = -2 days	15.2	5,800	4.4
Lag = 0 days	7.0	2,700	4.4
Lag = +2 days	3.5	1,300	4.4

deformation of the zonal flow. Observations presented in Figure 5.1b confirm that longitude bands of slow wave propagation (i.e., low OLR) are correlated spatially (r = 0.57) with the climatological locations of $\partial\overline{U}\big/\partial x < 0$. Equation 10 shows that wave energy density (ξ) can grow exponentially in regions where $\partial\overline{U}\big/\partial x < 0$. In fact, the magnitude of OLR anomalies show a tendency to become more enhanced as C_{gd} slows. Regression anomalies exceeding -6 W m^{-2} are more common with the slower and shorter synoptic disturbances in the subtropical SPCZ compared to over the Southeast Indian or Pacific regions (Figure 5.22 and Table 4).

5.4 Vertical structure of modes propagating into $\partial\overline{U}/\partial x < 0$ zones

We compute **Q** vectors in order to examine synoptic wave evolution in regions of negative zonal stretching deformation. Following Holton (2004), we can write the quasi-geostrophic omega equation:

$$\sigma\nabla^2\omega + f_0^2\frac{\partial^2\omega}{\partial p^2} = -2\nabla \bullet \mathbf{Q} + f_0\beta\frac{\partial v_g}{\partial p} - \frac{\kappa}{p}\nabla^2 J \tag{14}$$

where

$$\mathbf{Q} \equiv (Q_1, Q_2) = \left(-\frac{R}{p}\frac{\partial V_g}{\partial x} \bullet \nabla T,\ -\frac{R}{p}\frac{\partial V_g}{\partial y} \bullet \nabla T\right) \tag{15}$$

The equation is simplified by setting the diabatic heating term, J, equal to zero for

adiabatic motions and noting that the second term on the right-hand side, related to the β effect, is small for synoptic-scale motions. As $\nabla^2\omega$ goes as $-\omega$, then Equation 14 states that the vertical velocity field is given by the divergence of **Q**. Specifically, rising motion occurs where **Q** vectors are convergent ($\nabla \bullet \mathbf{Q} < 0$). Holton (2004) notes that "*because such rising motion must imply vorticity stretching in the column below, cyclonic vorticity will tend to increase below a region of upper level convergent* **Q** *vectors*". Thus, a test of our hypothesis is to determine whether there is an increase in the convergence of **Q** (increase in vertical velocity and vortex tube stretching) coupled with an increase of convection (measured by decreasing OLR) as a wave moves into a negative zonal stretching deformation region.

The unfiltered **Q** vector divergence and vertical pressure velocity ($-\omega$) are regressed onto the 3-6 day filtered OLR base point described in Figure 5.23. **Q** vectors are calculated from Equation 15 using geostrophic winds, derived from geopotential height fields, and atmospheric temperature for the 27 DJF seasons using NCEP-NCAR reanalysis data between 1000-100 hPa. Daily unfiltered anomalies are averaged over a 5° latitude band which is oriented diagonally and centered along a line extending from 50°S, 155°W to 10°S, 115°W that passes through the base point located at the eastern boundary of the SPCZ (30°S, 135°W). The diagonal cross section corresponds to the maximum OLR regression anomalies, or Rossby wave propagation, observed in Figure 5.23b-d. **Q** vector regression anomalies (shading) are displayed in space-log pressure coordinates for lags of -2, -1, 0, 1, and 2 days (Figure 5.24a-e, respectively). Solid (dashed) lines depict rising (sinking) velocity anomalies, with prominent regions of rising motion labeled "I", "II", or "III". Figure 5.23f shows the location of the averaging region in relation to the SPCZ.

Each lag period in Figure 5.24 shows a clear pattern of alternating positive and negative $\nabla \bullet \mathbf{Q}$ anomalies. The $\nabla \bullet \mathbf{Q}$ pattern above 200 hPa is out of phase with the anomalies below, which is evidence of convergence-divergence coupling centered along the tropopause, as is often observed with mid-latitude disturbances (e.g., Hoskins et al. 1978). Focusing on the troposphere, maximum $\nabla \bullet \mathbf{Q}$ anomalies are typically found between 300 hPa and 400 hPa,

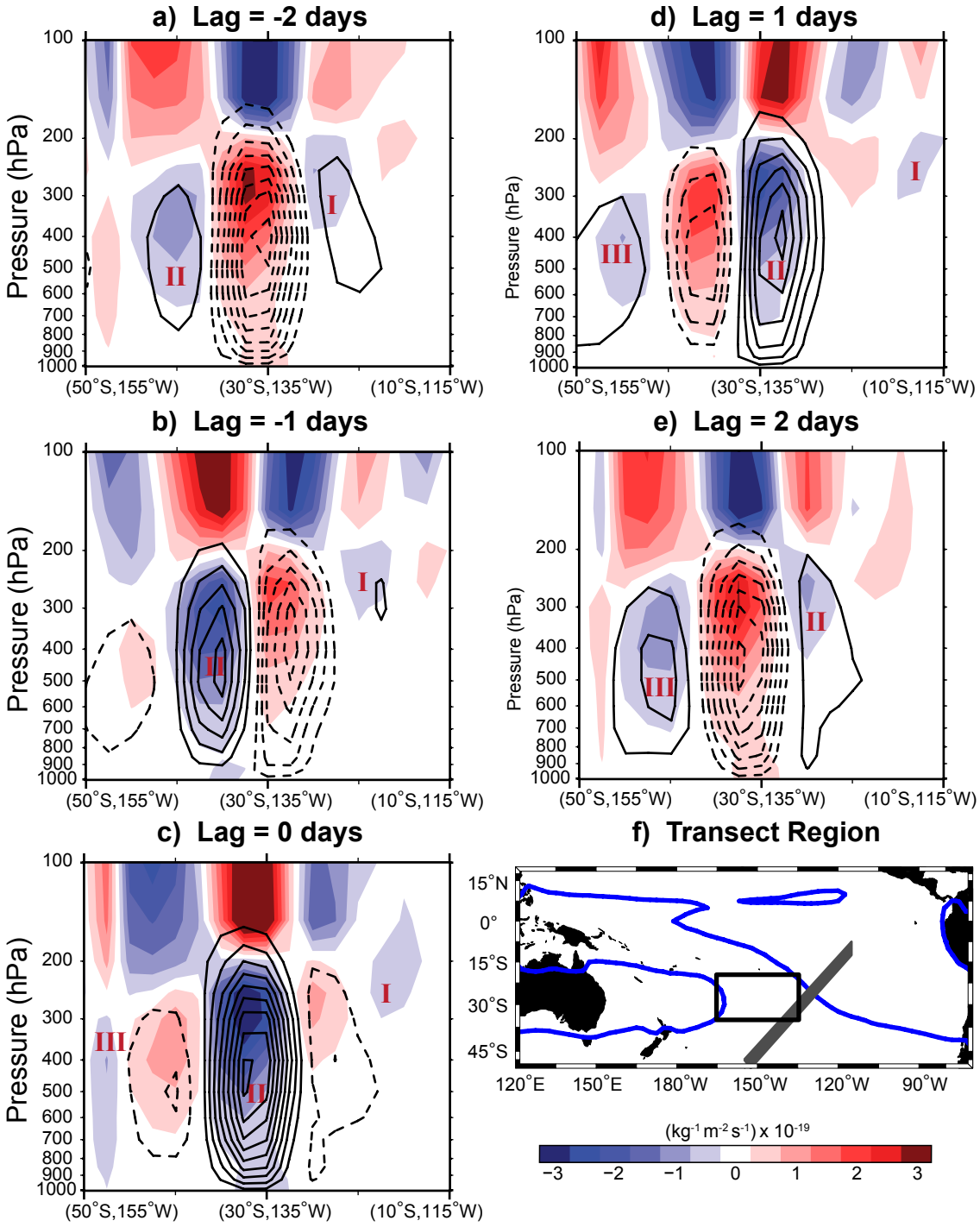

Figure 5.24: Vertical regression fields of **Q** vector divergence (kg^{-1} m^{-2} s^{-1}, shading) and vertical pressure velocity ($-\omega$ contour interval: $2x10^{-3}$ Pa s^{-1}; starting at $\pm 2x10^{-3}$ Pa s^{-1}) averaged over a 5° latitude band centered along a line from 50°S, 155°W to 10°S, 115°W which passes through the base point used in Figure 5.23. Solid (dashed) lines depict rising (sinking) velocity anomalies. Regions of rising motion discussed in the text are labeled "I", "II", or "III". (a, b, c, d, and e) Regressions at Lags -2, -1, 0, 1, and 2 days, respectively. (f) Map of the averaging region (gray shading) and 240 W m^{-2} OLR contour (DJF climatology) outlined by blue lines.

while vertical motions are strongest around 500 hPa. Strong subsidence is observed in the eastern SPCZ (30°S, 135°W) two days before maximum convection reaches the base point (Figure 5.24a). Rising motion (disturbance II) is centered near 40°S, 145°W and corresponds to minimum OLR observed in Figure 5.23b southwest of the base point at this time. Weaker rising motion (I) is also observed northeast of the SPCZ and is perhaps associated with the previous synoptic disturbance to track through the base point. Figure 5.24c shows clearly that the strong rising motion associated with disturbance II has reached the SPCZ base point when maximum convection occurs at lag 0 days. Subsidence exists on both sides of the convection. Evidence of weak rising motion ($\nabla \bullet \mathbf{Q} < 0$) associated with I is still observed over the tropical central Pacific. We also begin to see the next disturbance (III) enter the region near 50°S. During the next two days (Figure 5.24d and e), II propagates northeast and weakens while the vertical circulation associated with III amplifies, expands vertically, and approaches the SPCZ from the southwest.

Regressions of $\nabla \bullet \mathbf{Q}$ and $-\omega$ anomalies onto the filtered OLR time series provide evidence that vertical circulations, extending from the surface to the upper troposphere, are correlated with convective anomalies in the SPCZ. From the quasi-geostrophic omega equation (14), we note that vertical ascent is forced by **Q** vector convergence. Mid-latitude synoptic wave propagation was shown previously (Figures 5.22 and 5.23) to slow and become more energetic in the upper tropospheric region of $\partial\overline{U}/\partial x < 0$ observed in the diagonal SPCZ. Figure 5.24 shows that vertical motions intensify as mid-latitude disturbances propagate into the SPCZ, slow, and increase wave energy density according to Equation 10. Pronounced weakening of the vertical circulation (e.g., II at lag 2 days) occurs subsequently once a disturbance tracks east of the SPCZ and speeds up in the climatological region of positive zonal stretching deformation over the Southeast Pacific.

CHAPTER VI

APPLICATIONS TO OTHER SOUTHERN HEMISPHERE CONVERGENCE ZONES

All three of the diagonal cloud bands in the Southern Hemisphere are collocated with a region of negative zonal stretching deformation in the subtropics (Figure 5.1b). In the South Pacific, convection extends poleward from the warm pool and is oriented southwest of the maximum zonal SST gradient. Within the diagonal region of the SPCZ, the subtropical jet stream decelerates and in Chapter 5 we tested the hypothesis that in regions of $\partial\overline{U}\big/\partial x < 0$, synoptic disturbances slow as the wavelength shrinks. Wave energy density subsequently increases and convection becomes more intense in the SPCZ. Considering that the upper-troposphere zonal flow where cloud bands veer poleward in the South Atlantic and Indian basins is similar to the $\partial\overline{U}\big/\partial x < 0$ pattern in the Pacific, but noting that convection is oriented near continents and positioned over smaller ocean basins, we consider now whether the wave energy accumulation hypothesis is applicable to the SACZ and SICZ.

Numerous studies have examined the climatology of the SACZ (e.g., Lenters and Cook 1997; Liebmann et al. 1999; Carvalho et al. 2002; Cook 2009) especially, but also the SICZ (e.g., Cook 2000; Ninomiya 2008). Liebmann et al. (1999), for example, describes the SACZ as the dominant cloud band in the Atlantic extending southeastward from Amazon convection, but they note that convection rarely persists longer than 10 days. The SICZ is also diagonally oriented, but convection there is the most intermittent of the Southern Hemisphere convergence zones (Cook 2000). Some studies have also compared the SACZ with the SPCZ (Kodama 1992), or with the SICZ (Kodama 1993; Ninomiya 2007), and noted common features of the large-scale circulation associated with each cloud band. It

also seems likely that the three Southern Hemisphere convergence zones interact on interannual timescales (Lenters and Cook 1999; Robertson and Mechoso 2000) via long wave teleconnections triggered by ENSO (Cook 2001) and perhaps the varying position of the SPCZ (Grimm and Ambrizzi 2009). However, questions remain about the influence of Pacific SST anomalies on the SACZ and SICZ and it may be that Atlantic and Indian SST anomalies have a stronger influence on the local cloud bands (Nicholson 2003).

Fewer studies have examined the dynamical processes explaining why convection forms in the SACZ or SICZ, but Garreaud (2000), Rickenbach et al. (2002), and Carvalho et al. (2004) show evidence of baroclinic disturbances interacting with the cloud bands on synoptic timescales. More specifically, Fernandes (2009) and Nieto-Ferreira et al. (2010, manuscript submitted to *Quart. J. Roy. Meteor. Soc.*) examined the relationship between the onset of the South American monsoon and equatorward propagation of cold fronts. Nieto-Ferreira et al. (2010) found that cold fronts suddenly become stationary along the SACZ at the time of monsoon onset and identified enhanced meridional shear on the equatorward side of the upper-level jet during formation of cut-off cylcones. However, an exact physical mechanism explaining why fronts abruptly slow in only certain regions of the South Atlantic or South Indian basins remains uncertain. In this chapter, we briefly describe the convective patterns associated with the SACZ and SICZ and then compare features of the long wave circulation associated with these land-based convergence zones (Cook 2000; Ninomiya 2008) with similar features in the South Pacific. Particular attention is applied to examining the relationship between longitudinally varying zonal flow in the upper-troposphere and the location of convection in the South Atlantic and South Indian basins.

Comparison of the seasonal cycle of OLR for the Atlantic and Indian basins (Figures 6.1 and 6.2, respectively), shows evidence of diagonal cloud bands only during certain seasons. In the Atlantic, during all seasons except JJA, low OLR extends from Amazon convection in a southeastward direction towards the Southern Hemisphere mid-latitudes. Overlaid on

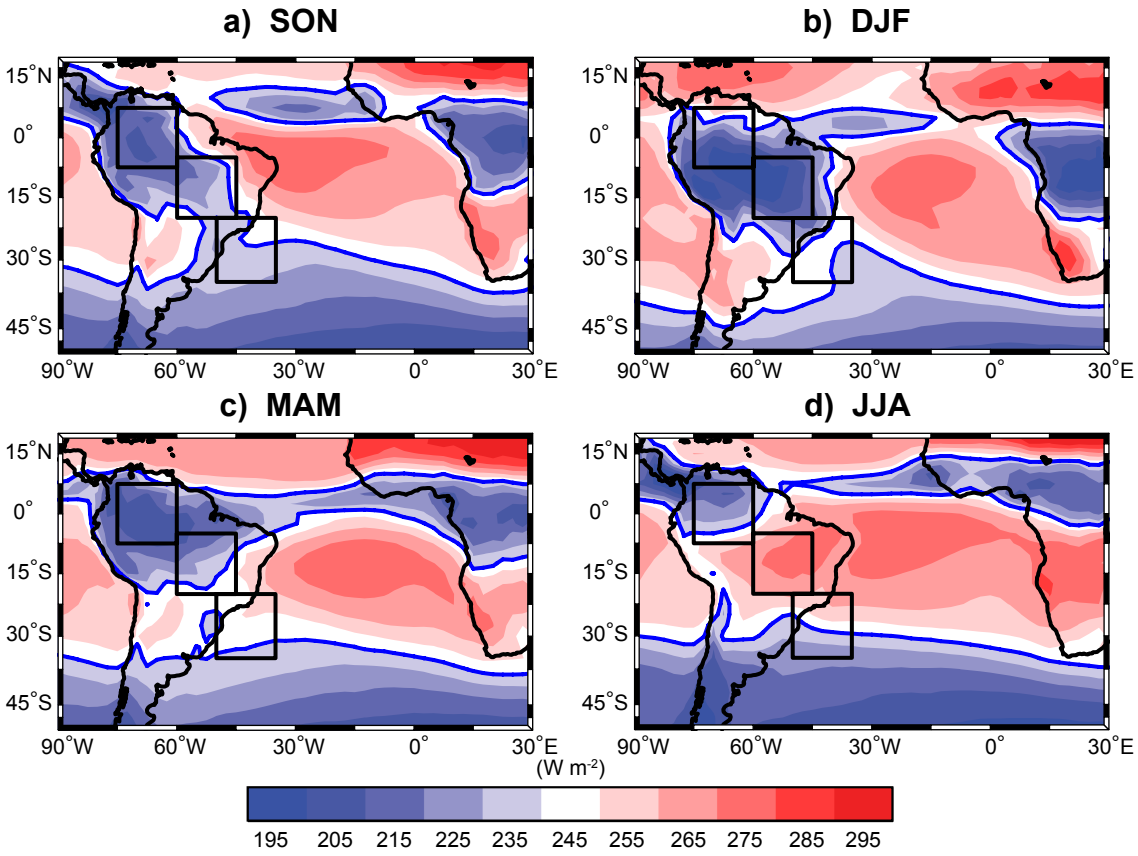

Figure 6.1: Seasonal climatology (1982-2008) of OLR (W m^{-2}) during (a) SON, (b) DJF, (c) MAM, and (d) JJA. Black boxes represent the "Equatorial" (7.5°N-7.5°S, 75°W-60°W), "Tropical" (5°S-20°S, 60°W-45°W), and "Subtropical" (20°S-35°S, 50°W-35°W) SACZ regions referred to in the text. 240 W m^{-2} OLR contour outlined by blue lines.

the OLR maps are black boxes denoting the equatorial, tropical, and subtropical regions of the SACZ and SICZ. Previous studies of precipitation patterns (summarized by Cook 2009) found the SACZ, essentially convection in the subtropical box of Figure 6.1, to become established during October and persist until March. In the Indian basin (Figure 6.2), convection veers poleward from equatorial Africa only during DJF. OLR values are typically higher in the SICZ (i.e., convection is weaker and more sporadic) and for clarity we include the 250 W m^{-2} OLR contour (dashed lines) in all analyses of the Indian basin. For consistency, we focus on the DJF climatology, the period of peak intensity of all three Southern Hemisphere convergence zones.

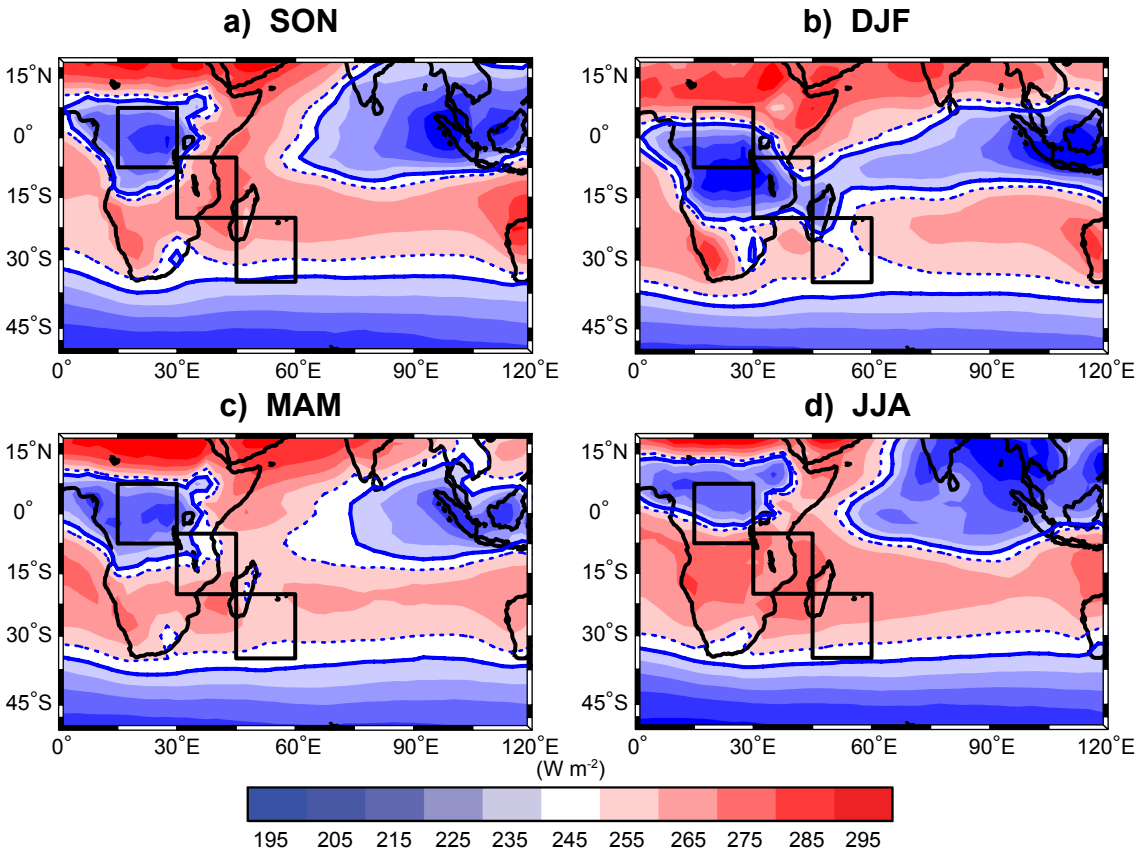

Figure 6.2: Same as Figure 6.1, but for the Indian basin. Black boxes represent the "Equatorial" (7.5°N-7.5°S, 15°E-30°E), "Tropical" (5°S-20°S, 30°E-45°E), and "Subtropical" (20°S-35°S, 45°E-60°E) SICZ regions referred to in the text. 240 W m^{-2} (solid) and 250 W m^{-2} (dashed) OLR contours outlined by blue lines.

Convection in the subtropical SACZ (Figure 6.1) is stronger and broader than the equivalent region of the SICZ (Figure 6.2), but weaker and narrower than in the SPCZ (Figure 2.1). However, each convergence zone extends diagonally from an extensive region of convection near the equator. In the South Atlantic basin (Figure 6.1), deepest convection is positioned over the Amazon basin most of the year, but shifts furthest south during DJF. Nieto-Ferreira et al. (2010) recently noted that convection in the southern Amazon may be enhanced by cold fronts propagating through the SACZ. Other studies (e.g., Lenters and Cook 1997) suggest latent heat release from tropical convection forces the long wave circulation which seems to influence the SACZ to the south. Northeast of the SACZ, a narrow equatorial strip of low OLR is also apparent and associated with the relatively weak boreal winter ITCZ positioned in the Northern Hemisphere. A similar region of low OLR is observed in the central Pacific northeast of the SPCZ. To the east of the SACZ, OLR values increase indicating minimum convection and subsidence associated with the Atlantic subtropical high pressure system.

Convection in the SICZ is the weakest of the three diagonal cloud bands in the Southern Hemisphere, but shares several common traits with the SACZ. During DJF, the lowest OLR in Figure 6.2 is observed around 15°S, 30°E and is associated with the African monsoon (Cook 2000). North of equatorial Africa is the Sahara desert and the highest OLR anywhere on the planet. Extending poleward from the monsoon convection are two narrow bands of low OLR (enclosed by the 250 W m^{-2} OLR contour) which are only slightly lower than the zonal mean OLR in the subtropics. These convective bands are located over southeastern Africa and south of Madagascar. Elsewhere, the ITCZ over the Indian Ocean is more pronounced than in other basins during DJF. High OLR values are observed over the Southeast Indian Ocean where surface pressures are also high, but the pattern is narrower and more zonally elongated than in the Pacific or Atlantic basins.

Poleward veering cloud bands in the South Atlantic and South Indian basins extend from equatorial convection over the South American and African continents, respectively.

Cook (2000) classifies the SACZ and SICZ as land-based convergence zones to distinguish them from the SPCZ, which extends from convection over the equatorial warm pool towards the higher latitude South Pacific. Proximity of the SACZ and SICZ to continents merits consideration of land boundary conditions, such as topography and surface heating, in addition to SST patterns. Figure 6.3 shows the land surface elevation (m, shading) of South America and Africa according to the NCEP-NCAR reanalysis (2.5° latitude-longitude resolution, Appendix A.3). Over South America, the Andes mountain range (elevations greater than 3,000 m) extends meridionally throughout the domain, but extends no more than 15° in the zonal direction. The Andes form the western border of Amazon convection. The East African highlands are also meridionally oriented, but elevated surfaces extend zonally across most of the southern half of the continent. Elevations are generally about 1,000 m in the highlands, but exceed 1,500 m in regions of southeastern Africa and east of the Sahara. Diagonal cloud bands, in both the Atlantic and Indian basin, veer poleward from equatorial convection in regions collocated with elevated land surfaces: The tropical region of the SACZ is positioned over the Brazilian highlands (elevations mostly between 500 m-1000 m) and a portion of low OLR associated with the SICZ is collocated with the southernmost region of the East African highlands. However, Kodama (1999) demonstrated in an aqua-planet GCM study that the SACZ, for example, could be simulated without influence of land, but only if a monsoon-like heat source was prescribed in the tropics.

Over the ocean, contours in Figure 6.3 represent the SST during DJF (red shading indicates tropical warm pools where the temperature is greater than 27°C). Comparison of the SST field in the three Southern Hemisphere basins (see also Figure 2.8 and the discussion in Chapter 2.3) yields several striking differences. In the Atlantic, the warm pool is narrower meridionally than in the Indian or West Pacific oceans, but extends longitudinally across the entire basin. South of the Atlantic warm pool is a region of zonal SST gradients

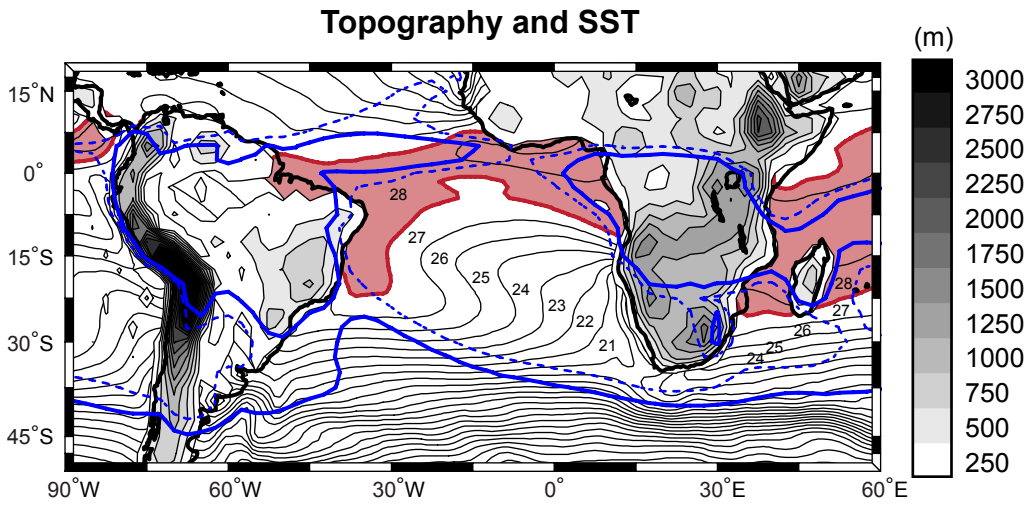

Figure 6.3: Land surface elevation (m, shading) and SST during DJF (1°C interval, red shading indicates temperatures above 27°C). OLR climatology for DJF indicated by blue contours: 240 W m^{-2} (solid) and 250 W m^{-2} (dashed).

much larger than the Indian zonal SST gradient, but smaller than the Pacific zonal gradient located northeast of the SPCZ. Poleward of 20°S, large meridional SST gradients are observed in the Atlantic, Indian, and Pacific oceans. Interactions between surface heating features with the SACZ and SICZ will be explored in more detail, subsequently.

For the remainder of this chapter, we explore whether the subtropical regions of the SACZ and SICZ are forced by dynamical processes similar to those which influence the diagonal region of the SPCZ. We first present a concise climatology of the SACZ and compare features of the Atlantic basic state circulation to observations of the South Pacific. Attention is applied towards comparing modes of variability within different latitude regions of each convergence zone. Similar analysis is done for the SICZ. We then test, using the AGCM from ICTP, the importance of the Atlantic and Indian basin zonal SST gradients in forcing the large-scale circulation and convective zones in either basin. Results are compared with experiments from Chapter 5.1 where topographic and continental configurations were altered in a global channel. Finally, we use composite analyses to address whether disturbances propagating into the negative zonal stretching deformation regions of the South Atlantic and South Indian basins are modified according to the wave energy

accumulation hypothesis presented in Chapter 4 (Equations 9 and 10).

6.1 Observed climatology of the SACZ and SICZ

We examine in detail the 1982-2008 period within the region enclosed by 20°N-50°S for the Atlantic (90°W-30°E) and Indian basins (0°-120°E), following the methodology of Chapter 2. First for the SACZ and then the SICZ, significant modes of convective variability in the equatorial, tropical, and subtropical regions are compared. We then discuss lower and upper tropospheric basic state circulations for each basin in the context of surface boundary temperature forcing from land and oceans. Data sets used to depict the observed climatology are the same as in Chapter 2 and described in the Appendix (OLR: A.1, NCEP-NCAR reanalysis: A.3, and SST: A.4).

6.1.1 SACZ

Maximum OLR variability over South America and the Atlantic is generally collocated with regions of deep convection in a pattern similar to the South Pacific. Figure 6.4a shows the OLR standard deviation for the Atlantic basin during the NDJFM period. The 240 W m^{-2} mean OLR contour (indicated by gray lines) for the same extended summer season clearly encloses convection associated with the ITCZ, Amazon basin, and portions of the SACZ. OLR standard deviations exceed 20 W m^{-2} in all of these regions, but are largest (greater than 30 W m^{-2}) near where the tropical and subtropical grid boxes intersect. Elsewhere, OLR variance is low over the Southeast Pacific and Southeast Atlantic, especially in the subtropics where surface pressures are high and convection is rare.

As was done in Chapter 2.1, normalized Fourier power spectra of OLR time series are used to compare the modes of variability for the equatorial, tropical, and subtropical SACZ regions (Figure 6.4b-d, respectively). Autocorrelations in each region of the SACZ are mostly constant; unlike the SPCZ where mean lag-1 autocorrelations decrease sharply with latitude. No significant signal associated with intraseasonal variability is evident in the equatorial region (b), but a spectral peak above the red noise curve occurs around 30 days in

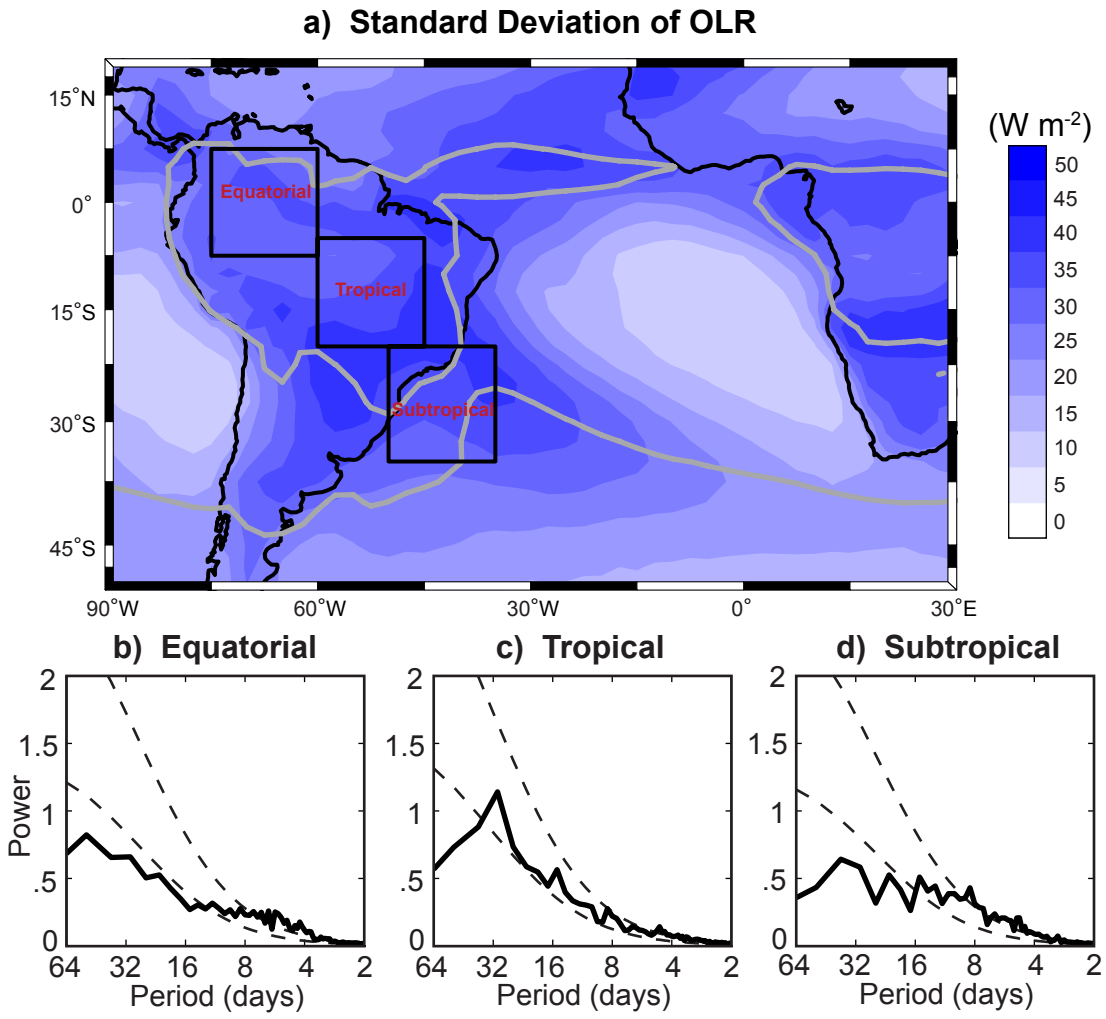

Figure 6.4: (a) Standard deviation of daily OLR (W m^{-2}) from NDJFM (1982-2008). 240 W m^{-2} OLR contour outlined by gray lines. Black boxes represent the "Equatorial" (7.5°N-7.5°S, 75°W-60°W), "Tropical" (5°S-20°S, 60°W-45°W), and "Subtropical" (20°S-35°S, 50°W-35°W) averaging regions for calculating OLR time series. (b, c, and d) Average Fourier power spectra of OLR in the equatorial, tropical, and subtropical regions of the SACZ, respectively. Lower dashed lines are the red-noise spectra for mean lag-1 autocorrelations of 0.58 (b), 0.62 (c), and 0.61 (d). Upper dashed lines are the 95% confidence spectra.

the tropics (c) which suggests that the tropical region of the SACZ varies on intraseasonal timescales. At all latitudes, variability is significant for periods shorter than 8 days, but the proportion of synoptic variability (2-8 days) is largest in the subtropics (d). Cunningham and Cavalcanti (2006) also found modes of variability on intraseasonal and synoptic timescales in OLR data from the SACZ, which they attributed to influences from the MJO and fontal systems, respectively. Poleward of 20°S, synoptic disturbances provide most of the convective variance as is observed in the SPCZ subtropical region (Figure 2.2d).

Figure 6.5a and b displays, respectively, the 850 hPa and 200 hPa geopotential height and wind in the context of the SACZ orientation. For reference, a black box (enclosing the region between 20°S-35°S and 50°W-35°W) is used to denote the subtropical SACZ, as described above. By comparing Figure 6.5 with Figure 2.5, we note that the long wave atmospheric circulation near the SACZ shares common features with the South Pacific. Figure 6.5a shows the lower tropospheric geopotential height (Φ) and wind field ($\overline{U}$ and $\overline{V}$) climatology. The highest heights of the 850 hPa pressure level are found over the cool Southeast Atlantic. Around the South Atlantic high, the circulation is anti-cyclonic with westerly winds around 40°S and easterly flow near the equator. Heights gradually decrease equatorward and the easterly trade winds are strongest over the central equatorial Atlantic. Convergence of the easterly flow occurs over the Amazon basin where convection occurs. The 200 hPa circulation associated with Amazon convection is anti-cyclonic (Figure 6.5b), but the upper tropospheric high is shifted southwest of maximum precipitation as noted previously by Lenters and Cook (1997, 1999). To the east, the 200 hPa flow is cyclonic above the South Atlantic surface high.

The 240 W m^{-2} OLR contour encloses Amazon convection and extends poleward along the western periphery of the South Atlantic high. Poleward of 40°S, 850 hPa heights decrease abruptly and winds near the surface become mostly westerly, as is common for all longitudes in the Southern Hemisphere mid-latitudes. Like in the Pacific, the 200 hPa pressure level (Figure 6.5b) is highest near the equator and decreases poleward. Meridional

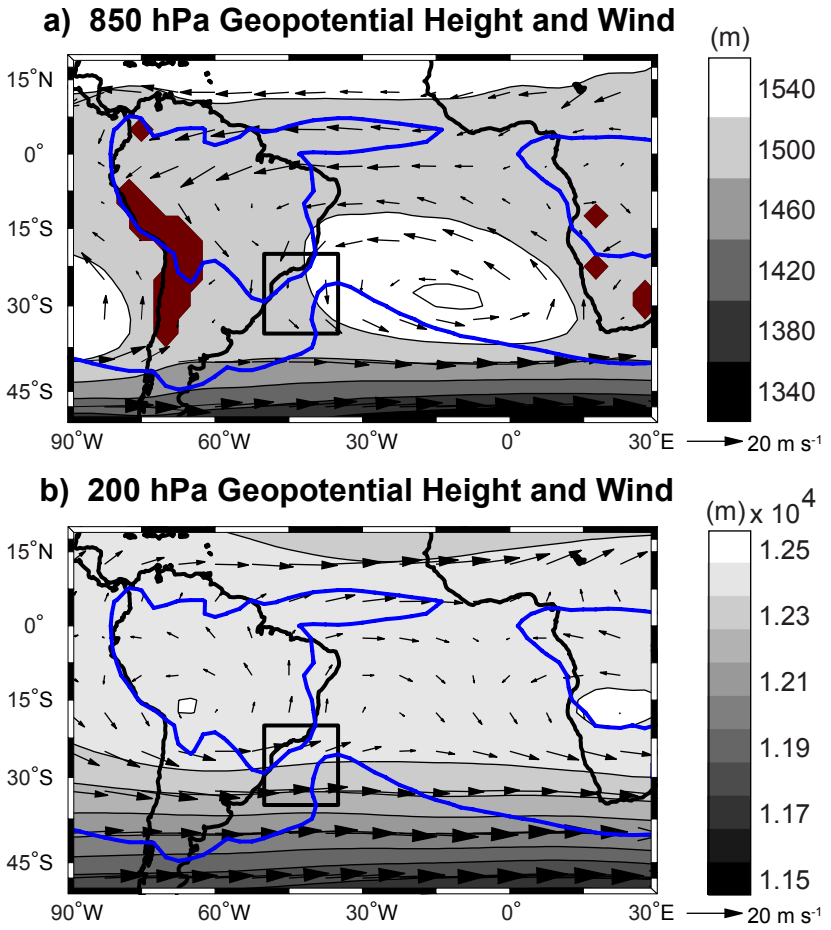

Figure 6.5: (a) DJF climatology (1982-2008) of 850 hPa geopotential height (m, shading) and winds (m s^{-1}, vectors). Regions where surface pressure is below 850 hPa are shaded brown. Black box (located at 20°S-35°S, 50°W-35°W) represents the subtropical SACZ. 240 W m^{-2} OLR contour outlined by blue lines. (b) 200 hPa geopotential height and winds.

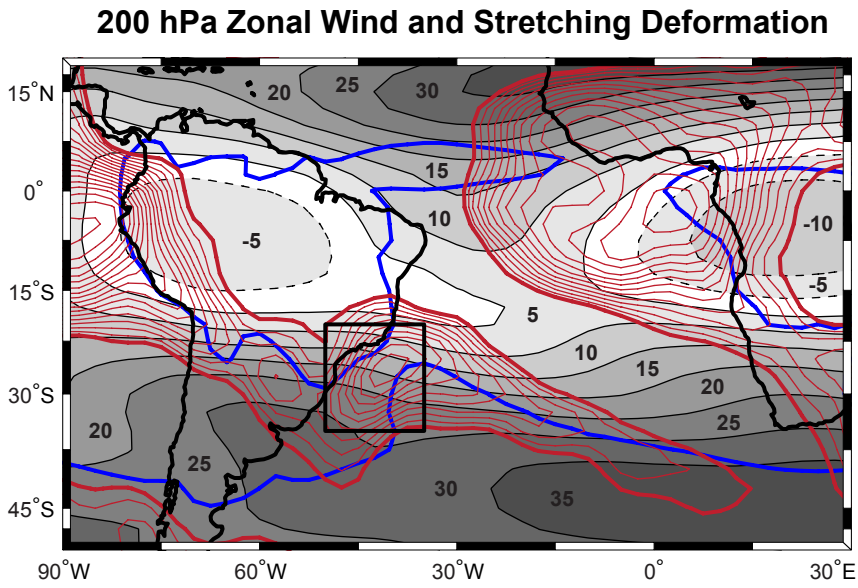

Figure 6.6: DJF climatology (1982-2008) of 200 hPa zonal winds (5 m s^{-1} shading interval, dashed lines depict negative zonal winds, zero contour omitted) and negative zonal stretching deformation (s^{-1}, red contours). Zonal stretching deformation contour interval: -5x10^{-7} s^{-1}; thick lines depict the zero contour. Black box (located at 20°S-35°S, 50°W-35°W) represents the subtropical SACZ. 240 W m^{-2} OLR contour outlined by blue lines.

height gradients are mostly uniform at all longitudes in the Atlantic, however, unlike in the Pacific where gradients are enhanced over the western and eastern parts of the basin.

Pronounced longitudinal variability of the 200 hPa zonal wind component ($\overline{U}$: Figure 6.6) is evident in the Atlantic basin, in contrast with the 200 hPa geopotential height pattern which is mostly uniform from west to east. Westerly winds are strongest in subtropical jets that extend across the basin in both hemispheres. Contours of $\partial\overline{U}/\partial x < 0$ clearly indicate where the Southern Hemisphere jet decelerates or shifts poleward. Within the subtropical SACZ, $\partial\overline{U}/\partial x = -4.5 \times 10^{-6} s^{-1}$ ($\partial\overline{U}/\partial x = -3.5 \times 10^{-6} s^{-1}$ within the SPCZ); however, the area of negative zonal stretching deformation in the subtropical Atlantic is smaller than in the SPCZ region. To the northeast of the SACZ, westerlies extend from the Northern Hemisphere jet into the central South Atlantic, but the longitudinal extent of the westerly duct is narrower than in the Pacific. Weak 200 hPa easterlies are observed over the Amazon, where equatorial convection is strongest.

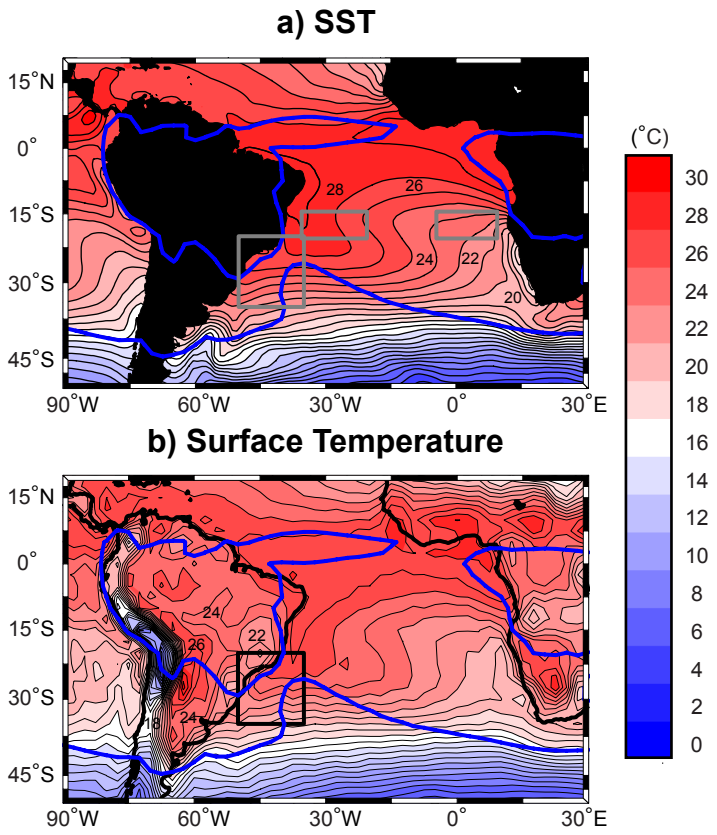

Figure 6.7: DJF climatology (1982-2008) of (a) SST and (b) near-surface air temperature (1°C interval). Large box (located at 20°S-35°S, 50°W-35°W) represents the subtropical SACZ. Small gray boxes (located at 14.5°S-20.5°S, 35.5°W-20.5°W and 14.5°S-20.5°S, 4.5°W-9.5°E) denote regions used to calculate the SST index. 240 W m^{-2} OLR contour outlined by blue lines.

The corresponding climatologies of SST and near-surface air temperature are shown in Figure 6.7a and b, respectively. The large box extends from 20°S-35°S and denotes the subtropical SACZ region. Northeast of the SACZ are two smaller gray boxes (shown in panel a: 35.5°W-20.5°W and 4.5°W-9.5°E) located at the latitude where the basin-scale zonal SST gradient is largest (about 5°C at 14.5°S-20.5°S). The zonal SST gradient is small poleward of the gray boxes, where the meridional surface temperature gradient is large. Near the equator, the warm pool extends across the basin and the zonal SST gradient is also small.

Near-surface air temperatures (Figure 6.7b) over the ocean are similar to SSTs, but over

land, reveal a complex surface heating pattern near the subtropical SACZ. A narrow strip of cool land surface temperatures (below 15°C) extends meridionally along the Andes. Surface temperatures are generally uniform throughout the Amazon and only slightly cooler than the adjacent Atlantic warm pool. South of the Amazon, warm land surface temperatures extend poleward along the eastern slope of the Andes and a narrow region of cooler land temperatures extends equatorward near the coast. Chou and Neelin (2001) noted that soil moisture variations in these regions (which are related to surface temperature patterns), together with variability of the subtropical jet stream, affects the positioning of the SACZ.

Interestingly, the seasonal mean near-surface temperature over subtropical South America (20°S-35°S, 65°W-50°W) is positively correlated with 200 hPa zonal stretching deformation (r= 0.64) and OLR (r = 0.30) in the adjacent SACZ region (20°S-35°S, 50°W-35°W). The correlations suggest that $\partial\overline{U}\big/\partial x$ becomes more negative and convection increases in the subtropical SACZ when South American land temperatures are cooler than normal. Strong seasonal correlations also exist between the 200 hPa geopotential height zonal gradient and the subtropical SACZ. The zonal height gradient is defined as the difference between mean heights over the Amazon (5°S-20°S, 60°W-45°W) and eastern Atlantic (5°S-20°S, 30°W-15°W). In this case, $\partial\overline{U}\big/\partial x$ and OLR become more negative (r = -0.35 and r = -0.52, respectively) when the zonal height gradient increases between South America and the Atlantic. These $\partial\overline{U}\big/\partial x$ and OLR correlations with 200 hPa height patterns are perhaps a manifestation of either varying land-ocean temperature gradients, or Amazon convection, on the upper troposphere long wave circulation and storm track, but further study is warranted. No robust seasonal correlations are observed between the zonal SST gradient (defined by the gray boxes in Figure 6.7a) and zonal wind or convective characteristics of the subtropical SACZ; however, De Almeida et al. (2007) noted an SACZ–SST negative feedback mechanism which operates on timescales shorter than those resolved by the seasonally averaged indices analyzed here.

6.1.2 SICZ

From the DJF climatology of OLR in Figure 6.2b, it is apparent that the SICZ is the least pronounced of the Southern Hemisphere convergence zones, especially in the subtropics. Analyses of the convective variability, long wave circulation, upper-troposphere zonal winds, and surface temperature boundary conditions associated with the SICZ are shown in Figures 6.8-6.11. Some of the large-scale climate features in the South Indian basin are similar to the South Atlantic basin. Here, we list four notable climate characteristics which distinguish the SICZ from either the SACZ or SPCZ:

(i) Power spectra of the SICZ reveal only a subtle shift with increasing latitude towards mostly synoptic variability (Figure 6.8b-d).

(ii) The South Indian surface high is weaker and more elongated in the zonal direction (Figure 6.9a), compared to the South Atlantic or South Pacific anticyclones.

(iii) Two diagonal bands of low OLR (less than 250 W m^{-2}) extend southeastward from Africa, but only the western cloud band is collocated with negative zonal stretching deformation (Figure 6.10).

(iv) And, the zonal SST gradient across the Indian basin (1°C-2°C) is the smallest of the three Southern Hemisphere oceans (Figure 6.11).

6.2 Numerical experiments

The idealized numerical experiments examined in Chapter 5.1 demonstrate that the uncoupled ICTP model simulates three bands of lower OLR which extend diagonally from regions of equatorial convection to the higher latitudes (Figure 5.4a). The bands of low OLR in the South Atlantic and South Indian basins share features with the observed SACZ and SICZ, respectively. Realistic simulations of the Southern Hemisphere cloud bands occur despite coarse model resolution of dynamical processes and surface boundary conditions,

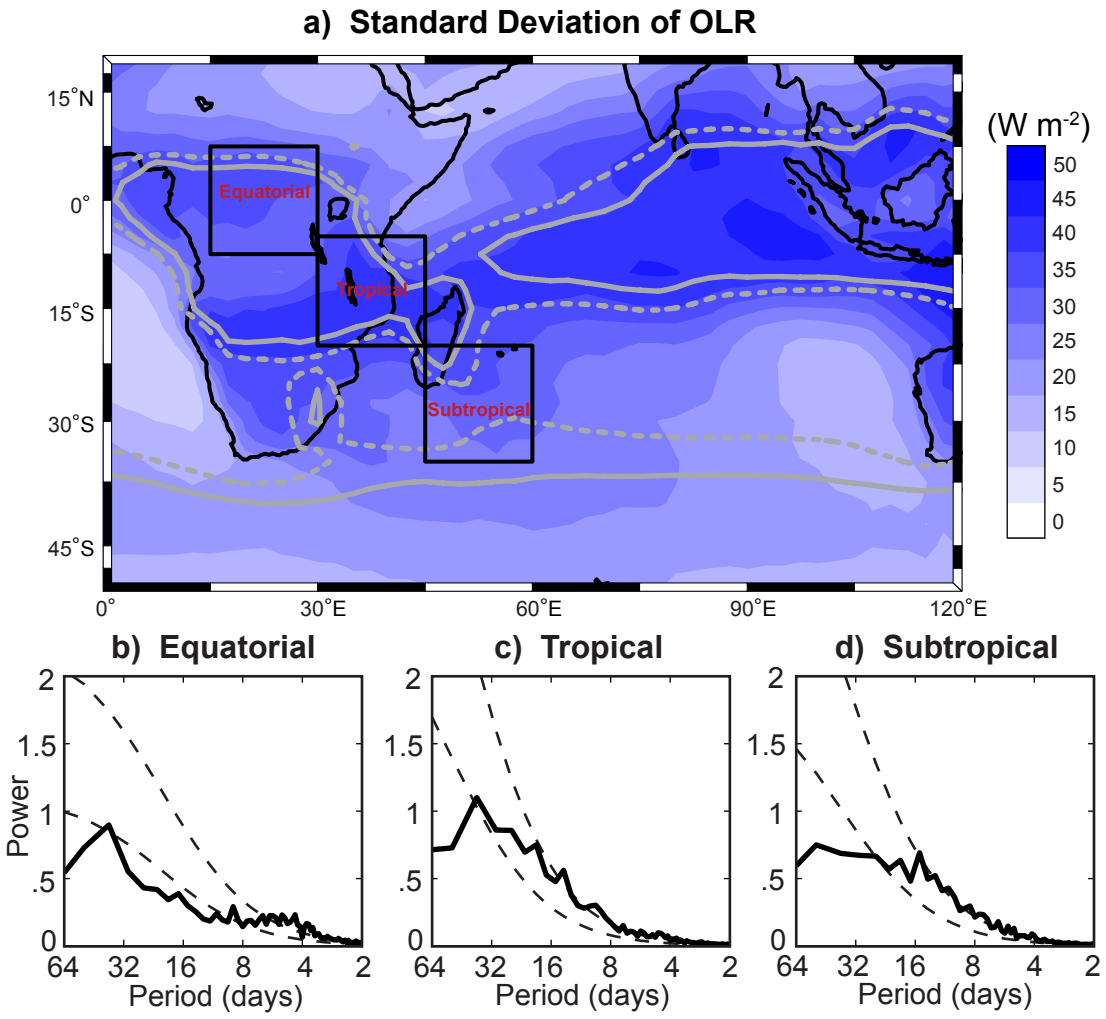

Figure 6.8: (a) Standard deviation of daily OLR (W m^{-2}) from NDJFM (1982-2008). 240 W m^{-2} (solid) and 250 W m^{-2} (dashed) OLR contours outlined by gray lines. Black boxes represent the "Equatorial" (7.5°N-7.5°S, 15°E-30°E), "Tropical" (5°S-20°S, 30°E-45°E), and "Subtropical" (20°S-35°S, 45°E-60°E) averaging regions for calculating OLR time series. (b, c, and d) Average Fourier power spectra of OLR in the equatorial, tropical, and subtropical regions of the SICZ, respectively. Lower dashed lines are the red-noise spectra for mean lag-1 autocorrelations of 0.44 (b), 0.76 (c), and 0.75 (d). Upper dashed lines are the 95% confidence spectra.

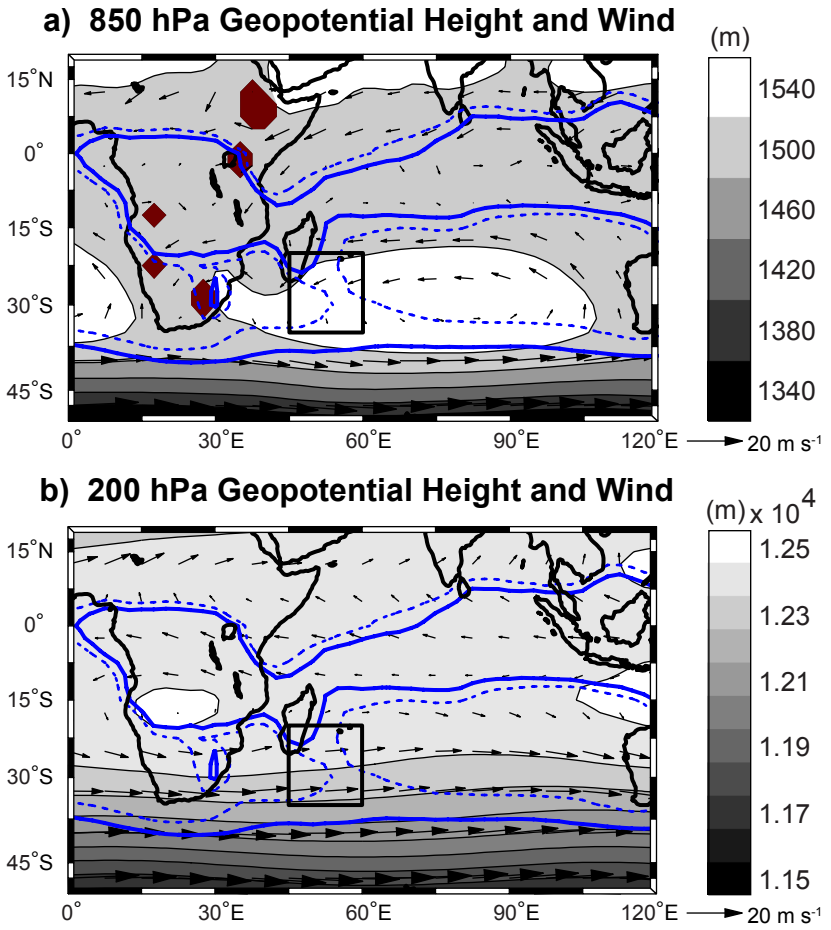

Figure 6.9: (a) DJF climatology (1982-2008) of 850 hPa geopotential height (m, shading) and winds (m s^{-1}, vectors). Regions where surface pressure is below 850 hPa are shaded brown. Black box (located at 20°S-35°S, 45°E-60°E) represents the subtropical SICZ. 240 W m^{-2} (solid) and 250 W m^{-2} (dashed) OLR contours outlined by blue lines. (b) 200 hPa geopotential height and winds.

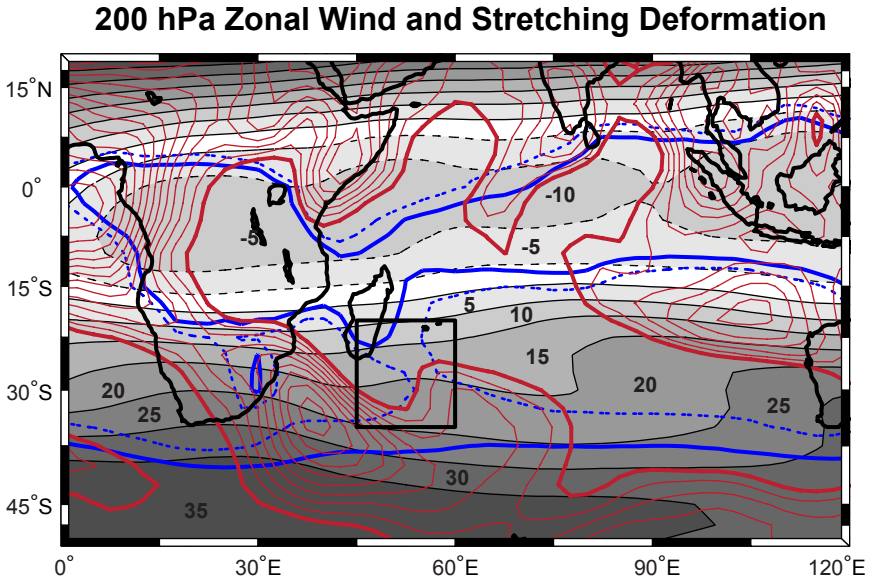

Figure 6.10: DJF climatology (1982-2008) of 200 hPa zonal winds (5 m s^{-1} shading interval, dashed lines depict negative zonal winds, zero contour omitted) and negative zonal stretching deformation (s^{-1}, red contours). Zonal stretching deformation contour interval: -5x10^{-7} s^{-1}; thick lines depict the zero contour. Black box (located at 20°S-35°S, 45°E-60°E) represents the subtropical SICZ. 240 W m^{-2} (solid) and 250 W m^{-2} (dashed) OLR contours outlined by blue lines.

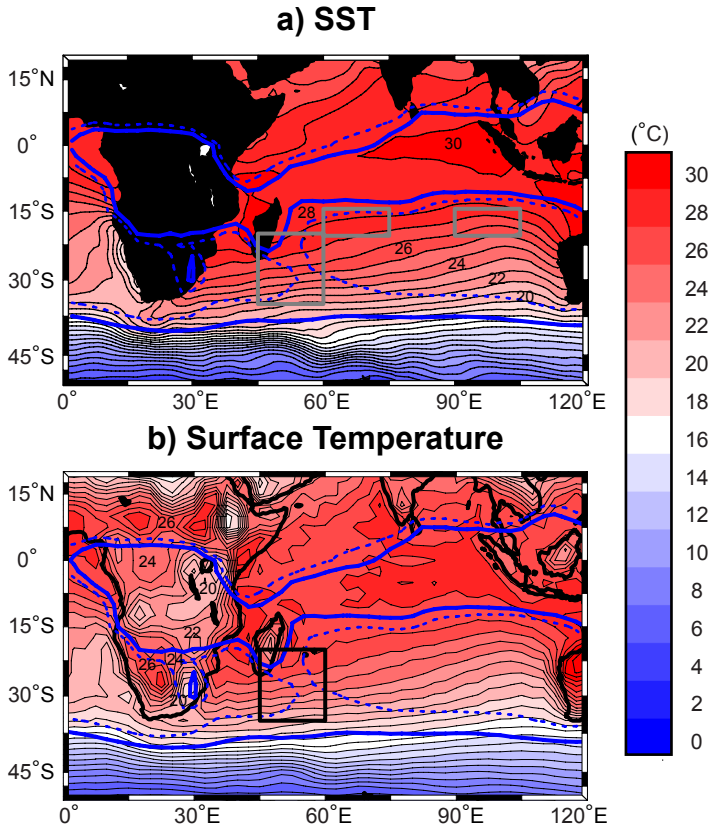

Figure 6.11: DJF climatology (1982-2008) of (a) SST and (b) near-surface air temperature (1°C interval). Large box (located at 20°S-35°S, 45°E-60°E) represents the subtropical SICZ. Small gray boxes (located at 14.5°S-20.5°S, 60.5°E-75.5°E and 14.5°S-20.5°S, 90.5°E-105.5°E) denote regions used to calculate the SST index. 240 W m^{-2} (solid) and 250 W m^{-2} (dashed) OLR contours outlined by blue lines.

such as ocean or land heating and topography. While removal of the Pacific zonal SST gradient forced convection to shift northeastward in the Pacific and the simulated SPCZ to disappear, removal of land elevation (Topography experiment), or even the continents completely (Orography experiment), did not force large convective changes in the SPCZ subtropical region (Figure 5.4b and c, respectively). Elsewhere, removal of topography or orography forced convection to decrease near the South Atlantic and South Indian cloud bands, especially near the location where land surfaces were either flattened or removed.

Following the methodology of the numerical experiments discussed in Chapter 5.1, we conduct two additional SST experiments where only the Atlantic or Indian Ocean SSTs are modified. Several previous studies utilized simple AGCM experiments to test the SACZ response to either removal of the Andes or prescribed atmospheric heating anomalies (Figueroa et al. 1995; Kodama 1999; Barreiro et al. 2002). Here, our objective is to specifically determine the importance of zonal SST gradients in forcing diagonal convective zones in the South Atlantic and South Indian basins. Each experiment is configured, initialized, and integrated for 26 years (of which a spin up period of 2 years is disregarded) using the AGCM provided by the ICTP and described in the Appendix (C.2) according to the methodology used to obtain a climatology of the Control simulation (Chapter 3.2) and the numerical experiments discussed previously (Table 1). Results are compared to the Topography and Orography experiments discussed in Chapter 5.1.

The ICTP Control simulation of OLR and 200 hPa zonal wind are examined in Figure 6.12 for the Atlantic and Indian basins. OLR values are generally higher than observed throughout the tropics and subtropics, suggesting that the model is not simulating as much convection as observed in either basin. Here, the 250 W m^{-2} (dashed) OLR contour is shown along with the 240 W m^{-2} (solid) contour to more thoroughly enclose weaker convection in the simulated SACZ and SICZ.

In the Atlantic basin, bands of low OLR extend horizontally and diagonally from Amazonian convection. The horizontal cloud band is located near the equator and is strongest

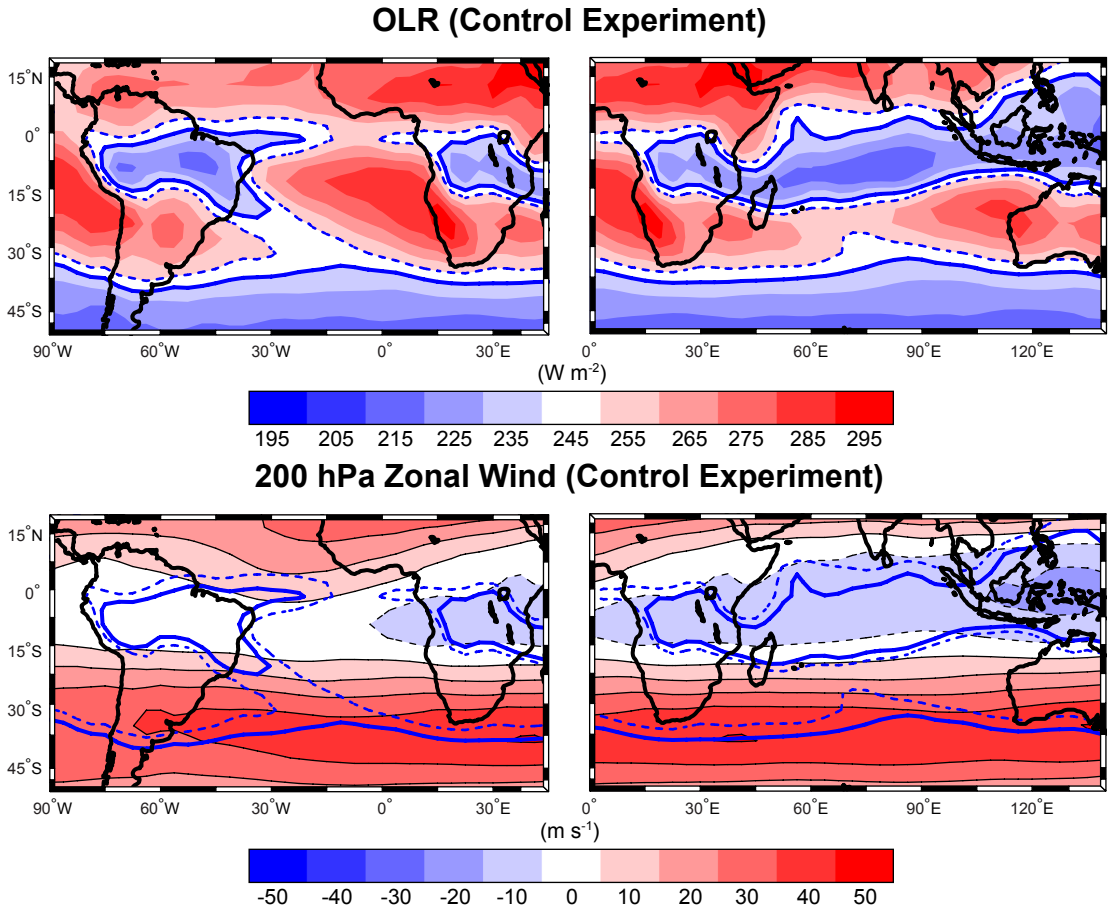

Figure 6.12: DJF climatology (24 seasons) of simulated OLR (W m^{-2}, top) and 200 hPa zonal winds (5 m s^{-1} shading interval, dashed lines depict negative zonal winds, zero contour omitted, bottom) for the Atlantic and Indian basins (left and right columns, respectively). 240 W m^{-2} (solid) and 250 W m^{-2} (dashed) OLR contours outlined by blue lines.

near the South American coast, similar to observations. Around 15°S in the eastern Amazon, convection veers poleward and merges near 35°S with low OLR associated with Southern Hemisphere baroclinic storms. The diagonal band of low OLR connecting Amazonian convection with the higher latitudes represents the simulated SACZ. Convection is weaker than observed at all latitudes and the cloud band appears narrower and shifted slightly east (i.e., a horizontal bias) in the simulation.

Convection biases in the Control experiment are even more pronounced over Africa and the Indian basin. African convection is much weaker than observed between 5°N-20°S and only a subtle region of lower OLR connects the tropics with the mid-latitudes. Convection over the Indian basin is confined to the tropics where minimum OLR, associated with the simulated ITCZ, is slightly lower than observed. Elsewhere, high OLR is simulated over the Southeast Atlantic and Indian basins, as well as the Sahara and parts of Southern Africa.

The Control simulation clearly simulates a 200 hPa westerly wind maximum in the subtropics; however, the jet stream is stronger than observed throughout most longitudes. Unlike the observed zonal flow, the simulated jet does not veer poleward near the east coasts of South America or Africa. Instead, zonal winds are mostly uniform across all longitudes. Regions of negative zonal stretching deformation are limited, but there is a slight deceleration of zonal winds near the simulated SACZ. The jet maximum is also shifted equatorward about 5° in both the Atlantic and Indian basins. In the tropics, easterly winds extend from Africa to Indonesia and a westerly wind duct is evident in the central Atlantic, but weaker than observed.

Two "SST" experiments are configured to test the importance of zonal gradients of Atlantic and Indian SSTs in forcing either the SACZ or SICZ, respectively. For each experiment, the control SST distribution of either the Atlantic (71.25°W-30°E) or Indian oceans (30°E-120°E) is replaced with the zonal average of observed values by setting $dSST/dx = 0$ for the respective basin between 61°N-61°S. Similar to the idealized Pacific SST experiment in Chapter 5.1, the zonally averaged SST maintains an annual cycle

consistent with the monthly varying climatology. Elsewhere, SSTs have the same evolving climatological annual cycle used in the Control experiment.

Figure 6.13 shows the imposed heating anomaly in the Atlantic and Indian basins during DJF. Unlike the Pacific experiment where the largest changes to the SST field were mostly confined to the tropics and subtropics, imposed anomalies in the South Atlantic and South Indian oceans are of mostly similar magnitude (but different signs) at all latitudes, except near the equator where zonal SST gradients are negligible. In the Atlantic basin, heating anomalies exceeding ±2°C are common in the tropics, subtropics, and mid-latitudes, except around 30°S where the zonal SST gradient is small. To remove the zonal gradient, SSTs are generally lowered in the western Atlantic and increased in the eastern half of the basin. The observed zonal SST gradient is small near the equator, hence negligible heating anomalies are applied. In the Northern Hemisphere Atlantic, the moderate zonal SST gradient around 15°N and a strong gradient poleward of 45°N are removed. In the Indian basin, the largest heating anomalies are applied in the Southern Hemisphere. Removing the zonal SST gradient in the South Indian Ocean requires applying heating anomalies organized in a quadrupole pattern. In the subtropics, SSTs are lowered by about 2°C near Africa and increased about the same amount near Australia. Poleward of 40°S, the sign of heating anomalies are reversed.

For each of the idealized numerical experiments, variations in the location and strength of convection, in addition to the 200 hPa zonal flow, are examined. Departures from the Control simulation during DJF are shown in Figure 6.14. There is only a subtle response of convection and 200 hPa zonal flow to removal of the Atlantic or Indian zonal SST gradients, in agreement with Kodama (1999) who noted the main formation criteria of a convergence zone such as the SACZ is a broad region of tropical convection and interaction of the long wave circulation with mid-latitude frontal systems. Over South America and Africa, limited OLR anomalies are noted. More pronounced convective anomalies are simulated

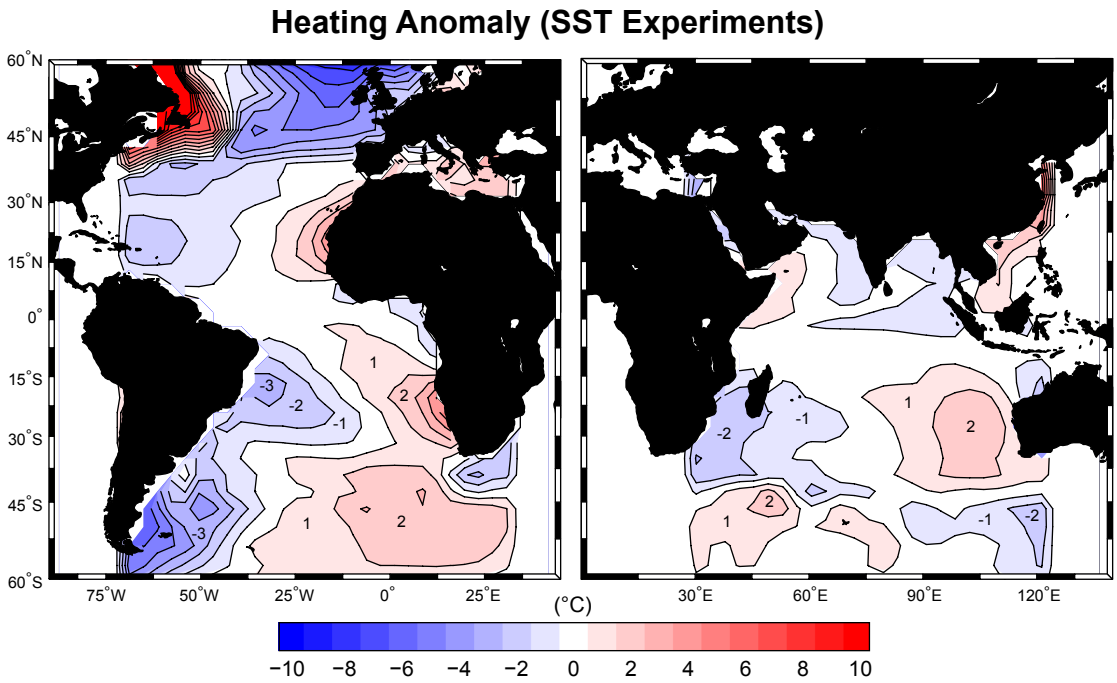

Figure 6.13: SST Experiments: Heating anomaly (°C) during DJF for the Atlantic (left) and Indian (right) basins.

over the oceans, especially in regions where heating anomalies are applied. Small upper-level zonal wind anomalies are simulated over the continents and oceans.

Removal of the Atlantic zonal SST gradient forces increased OLR in the tropical SACZ near the South American coast and decreased OLR to the northeast over the central equatorial Atlantic; however, anomalies do not exceed 20 W m^{-2} in either region. To the south of the control SACZ, OLR decreases by about 10 W m^{-2}. Away from the SACZ, OLR increases near the equatorial African coast, suggesting that the ITCZ weakens slightly in response to the prescribed heating anomalies which decrease the meridional SST gradient along the African coast.

The subtropical jet stream weakens in the Atlantic and over a small region of South America. The weaker jet stream over the Atlantic results in zonal stretching deformation becoming more negative around 30°S, 45°W. Interestingly, negative OLR anomalies are noted in the same regions where $\partial\overline{U}/\partial x$ decreased (i.e., in a horizontal band around 30°S

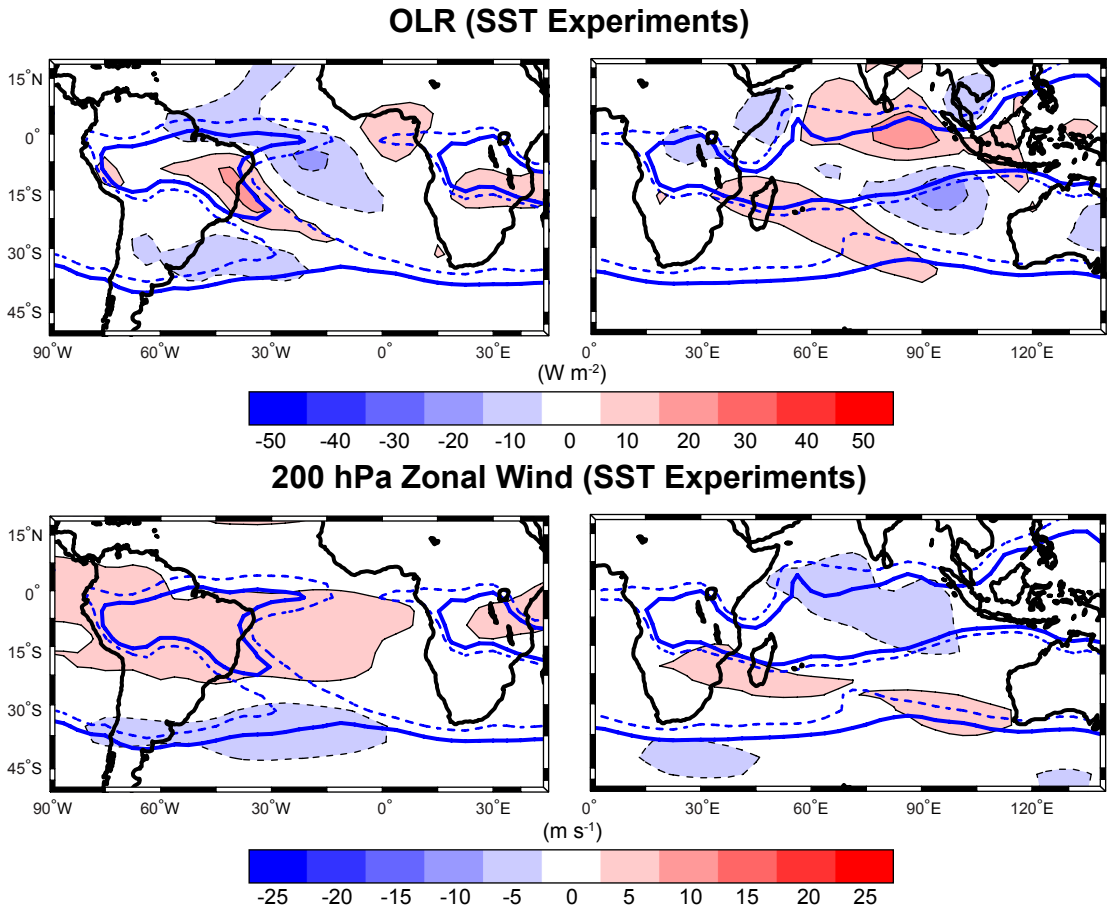

Figure 6.14: Same as Figure 6.12, but for departures from the Control simulation when the zonal SST gradients are removed in either the Atlantic (left) or Indian (right) basins.

between 60°W-30°W). Equatorward of 15°S, zonal winds are more westerly in all regions, except along the African coast where no change occurred to the easterly wind basic state. Removal of the zonal SST gradient seems to force a broader westerly wind duct in the Atlantic.

Removal of the Indian zonal SST gradient requires only small prescribed heating anomalies. As expected, the resultant OLR and 200 hPa zonal wind anomalies are also small. Positive OLR anomalies (+10 W m^{-2}) extend diagonally from the tropics to higher latitudes at longitudes where the lowest OLR in the subtropics is simulated in the Control. Essentially, removal of the zonal SST gradient forces the convection pattern to become even more uniform throughout the subtropical Indian basin. Zonal wind anomalies are small everywhere, but positive anomalies near Madagascar indicate that the subtropical jet stream shifts slightly equatorward. In the eastern Indian basin, both the warm pool and convection shift south in response to the prescribed SST anomalies. Poleward of the deepest convection, westerlies increase slightly and the zonal jet is enhanced.

Only small changes in OLR (top of Figure 6.14) and 200 hPa zonal wind patterns (bottom of Figure 6.14) are evident in the Atlantic and Indian SST experiments. Positive OLR anomalies (reduced convection) exceed 20 W m^{-2} in the tropical SACZ region (45°W-30°W). The axis of positive OLR anomalies is oriented diagonally and coincides with the location of the SACZ in the Control run. Northeast of the Control SACZ, OLR reductions of similar magnitude occur suggesting a migration of convection to the northeast. Clearly, zonal SST gradients are related to the location and orientation of the SACZ; however, the sensitivity of convection in the Atlantic to zonal SST gradients is smaller than in the Pacific. An even weaker convection response is evident in the Indian SST experiment, but caution must be exercised in evaluating this result because only a subtle diagonal cloud band exists in the Control simulation of the Indian basin.

6.3 Wave energy accumulation

In Chapter 5, we noted from the longitude-time case study of meridionally averaged observed OLR (Figure 5.1) that convection is frequent in the subtropics over each of the Southern Hemisphere oceans at certain longitudes where $\partial\overline{U}/\partial x$ is also the most negative. A similar relationship between convection and negative zonal stretching deformation, which occurs where the subtropical jet decelerates, is evident in the AGCM control experiment. While removal of the Atlantic or Indian zonal SST gradients have only small impacts on circulation patterns of the Southern Hemisphere, regions of negative zonal stretching deformation are still observed near the subtropical regions of the SACZ and SICZ. Definitively testing what factors force the long wave circulation outside of the Pacific basin is beyond the scope of this study, but it does seem probable that orientation of topography and land-based convection force upper-troposphere zonal winds favorable for formation of the SACZ and SICZ (both convergence zones are set in climatological negative zonal stretching deformation regions as shown in Figure 5.1b). Regardless of what mechanisms force $\partial\overline{U}/\partial x < 0$ in specific regions of the South Atlantic and Indian basins, we can examine whether disturbances passing though such regions are modified according to the wave energy accumulation hypothesis (i.e., Equations 9 and 10). Here, we use the methodology from Chapter 5.3, again adapted from Serra et al. (2008), to composite synoptic disturbances which pass through the SACZ and SICZ. Kinematic characteristics of the observed waves are then calculated.

Figure 6.15a shows a regression of unfiltered OLR (shading) and $\partial\overline{U}/\partial x$ (contours) between 120°W and 0° (i.e., the SACZ region and the area directly west or upstream) based on a -20 W m^{-2} anomaly in 3-6 day filtered OLR at 30°S, 45°W for lags -10 to 10 days. The longitude-lag regression is performed for a base point at 30°S to optimize observations of OLR anomalies which propagate into the diagonal region of the SACZ. Figure 6.15b-d shows longitude-latitude maps of the OLR and $\partial\overline{U}/\partial x$ regression for lags -2, 0, and 2 days. An equivalent composite analysis of disturbances passing through the SICZ (base point at

30°S, 60°E) is shown in Figure 6.16.

Both longitude-lag regressions (Figure 6.15a and 6.16a) show convective anomalies every three to five days, similar to the dominate mode of variability at 30°S in the SPCZ. In the SACZ and SICZ, $\partial\overline{U}\big/\partial x < 0$ anomalies (solid contours) are observed to lead most of the OLR negative anomalies by about one day, or 5° of longitude. At lag 0 days, when convection is most enhanced in the subtropical SACZ and SICZ (Figure 6.15c and 6.16c), oscillating positive and negative zonal stretching deformation anomalies extend from poleward of 50°S northeast to around 15°S in the Atlantic and Indian oceans. The pattern is suggestive of Rossby wave guides interacting with both convergence zones and is similar to observations of the South Pacific where synoptic waves propagate from the extratropics northeastward into the subtropics. Negative OLR signals can be tracked westward and eastward from the base points (lag 0 days) in each basin; however, anomalies in the South Atlantic and Indian basins propagate further east by lag 2 days than anomalies in the South Pacific. In the Indian basin, there is little evidence of the composite disturbance dissipating near the eastern boundary of the SICZ. Convective anomalies are also smaller and less persistent, compared to synoptic disturbances in the South Pacific or Atlantic.

Using the same wave tracking procedure as was done for the SPCZ in Chapter 5.3, the wavelength (km), phase speed (m s^{-1}), and period (days) are calculated for synoptic disturbances propagating through the South Atlantic and South Indian basins. Tables 6 and 7 show the wave characteristics for the SACZ and SICZ, respectively, at lags -2, 0, and 2 days. For comparison, the tables also show wave characteristics for base points located west and east of each convergence zone, but located within the respective ocean basin. The tables confirm that wavelengths shrink and phase speeds decrease as disturbances propagate through the SACZ and SICZ. In the Atlantic, wavelength shrinks from 4,400 km to 1,800 km and phase speed decreases from 11.9 m s^{-1} to 5.3 m s^{-1}. The decrease in wavelength and phase speed is larger for disturbances propagating through the SACZ, compared to the SICZ, but these changes are less pronounced than in the South Pacific where wavelength

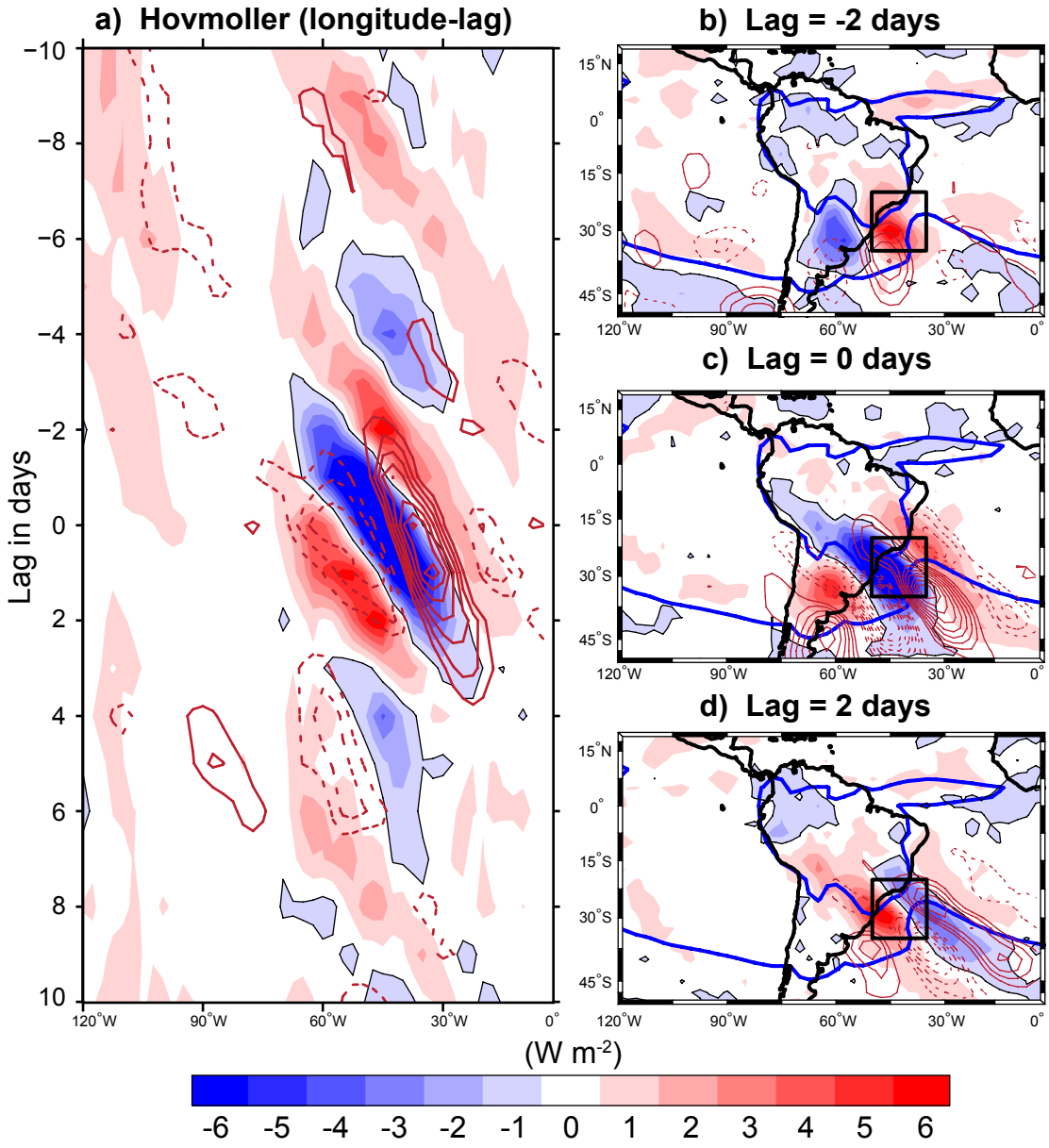

Figure 6.15: (a) Hovmoller (longitude-lag) of OLR (W m^{-2}, shading, -1 W m^{-2} contour outlined) and 200 hPa zonal stretching deformation (s^{-1}, contours) regressions at 30°S for a 3-6 day filtered base point (-20 W m^{-2} threshold) at 30°S, 45°W. Zonal stretching deformation contour interval: $2x10^{-7}$ s^{-1}; starting at $\pm 4x10^{-7}$ s^{-1}. Solid (dashed) lines depict negative (positive) anomalies. (b, c, and d) Same as (a) but for longitude-latitude regressions at Lags -2, 0, and 2 days, respectively. 240 W m^{-2} OLR contour (DJF climatology) outlined by blue lines.

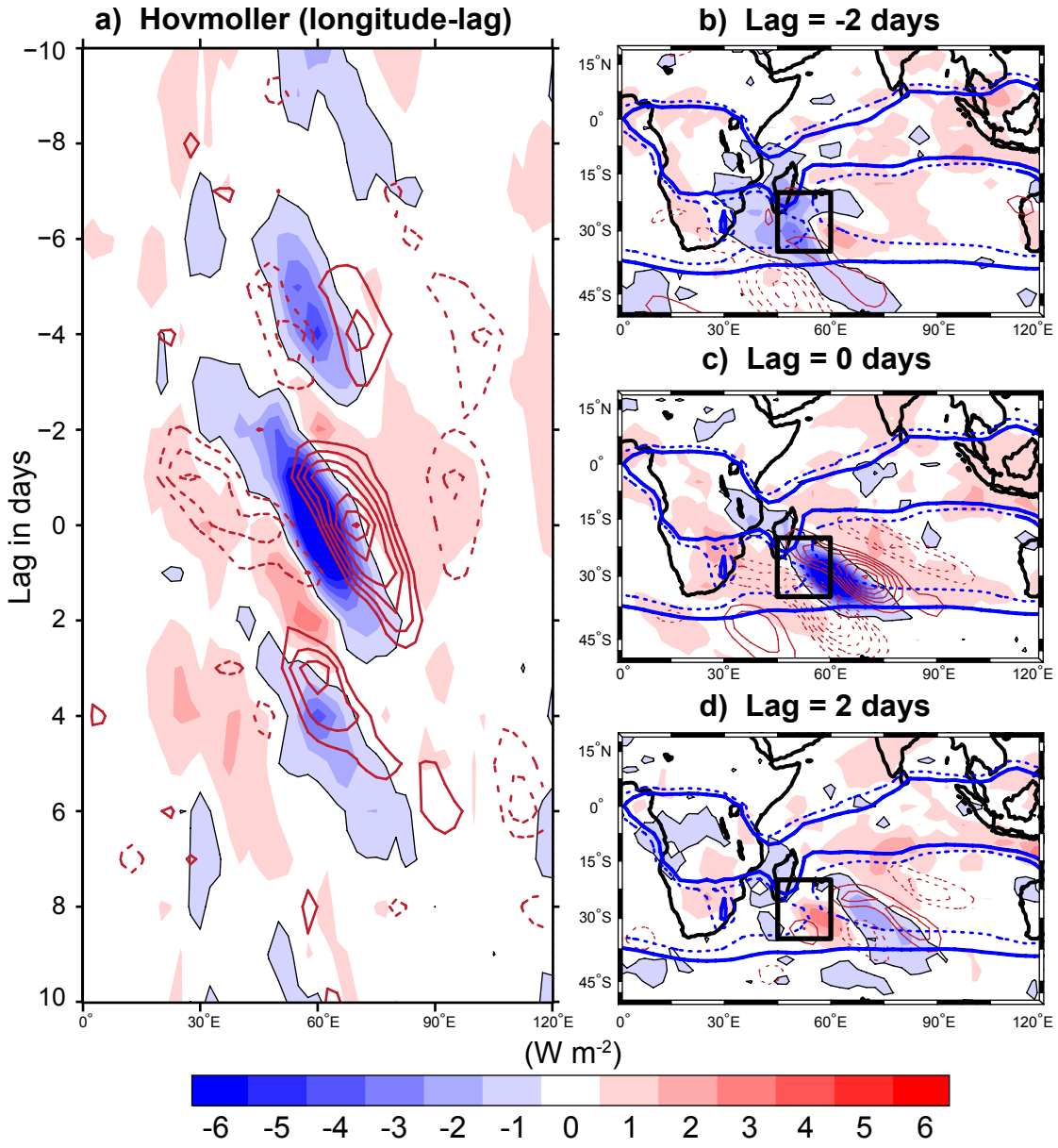

Figure 6.16: (a) Hovmoller (longitude-lag) of OLR (W m^{-2}, shading, -1 W m^{-2} contour outlined) and 200 hPa zonal stretching deformation (s^{-1}, contours) regressions at 30°S for a 3-6 day filtered base point (-20 W m^{-2} threshold) at 30°S, 60°E. Zonal stretching deformation contour interval: $2x10^{-7}$ s^{-1}; starting at $\pm 4x10^{-7}$ s^{-1}. Solid (dashed) lines depict negative (positive) anomalies. (b, c, and d) Same as (a) but for longitude-latitude regressions at Lags -2, 0, and 2 days, respectively. 240 W m^{-2} (solid) and 250 W m^{-2} (dashed) OLR contours (DJF climatology) outlined by blue lines.

shrinks to 1,300 km and disturbances propagate only about 3.5 m s^{-1} through the SPCZ (see Table 5 for comparison). In all regions, the periods of variability are similar (about 4 days) as frequency of the waves is conserved (Chapter 4).

Table 6: Synoptic-wave characteristics for Southwest Atlantic (30°S, 75°W), SACZ (30°S, 45°W), and Southeast Atlantic (30°S, 15°W) 3-6 day filtered OLR base points. Characteristics for a disturbance propagating through the SACZ are derived from $\partial\overline{U}/\partial x$ regression anomalies at Lags -2, 0, and 2 days (Figure 6.15b-c) using the observed period of OLR variability at 30°S, 45°W (4 days).

Base Point	**Phase Speed (m s^{-1})**	**Wavelength (km)**	**Period (days)**
30°S, 75°W	11.9	4,400	4.3
Lag = -2 days	9.3	3,200	4
Lag = 0 days	5.3	1,800	4
Lag = +2 days	6.3	2,200	4
30°S, 15°W	14.1	5,100	4.2

Table 7: Synoptic-wave characteristics for Southwest Indian (30°S, 30°E), SICZ (30°S, 60°E), and Southeast Indian (30°S, 105°E) 3-6 day filtered OLR base points. Characteristics for a disturbance propagating through the SICZ are derived from $\partial\overline{U}/\partial x$ regression anomalies at Lags -2, 0, and 2 days (Figure 6.16b-c) using the observed period of OLR variability at 30°S, 60°E (4 days).

Base Point	**Phase Speed (m s^{-1})**	**Wavelength (km)**	**Period (days)**
30°S, 30°E	11.9	4,300	4.2
Lag = -2 days	8.3	2,900	4
Lag = 0 days	7.4	2,500	4
Lag = +2 days	6.6	2,300	4
30°S, 105°E	10.8	4,000	4.3

CHAPTER VII

DISCUSSION AND CONCLUSIONS

Significant correlation between cloud band orientation and large-scale circulation patterns favorable for wave energy accumulation suggest a new mechanism for explaining why convection veers sharply away from the equator in three Southern Hemisphere locations. Regions of convergent zonal flow, or negative zonal stretching deformation, in the upper troposphere reduce the longitudinal scale of eastward propagating synoptic Rossby waves. Within these regions of $\partial\overline{U}\big/\partial x < 0$, the group speed is reduced and wave energy density locally increases. In addition, the vertical scale of disturbances increases and convection is enhanced. Wave accumulation occurs in the vicinity of the SPCZ where the subtropical jet decelerates, thus providing a physical basis for the diagonal orientation. While our focus has been on the SPCZ, similar long wave circulation features are present in the South Atlantic and Indian basins, although the configuration of continental heating, topography, and SST patterns vary among basins. Regardless of the variety of surface boundary conditions, the collocation of negative zonal stretching deformation and convection suggest that the three diagonal cloud bands share common physical processes.

Convection in each convergence zone varies on multiple timescales, but modes of variability are typically longer in the tropics and shorter in the higher latitudes. Poleward of 20°S, the cloud bands become more diagonally oriented and variability is dominated by periodicities shorter than two weeks. Evidence of baroclinic-type disturbances interacting with the subtropical SPCZ on synoptic timescales has been noted in numerous previous studies (e.g., Streten 1973) and similar interactions have been observed in the South Atlantic (Garreaud 2000) and Indian (Cook 2000) basins. Each of these studies note that

transient eddies interact with the quasi-stationary long wave circulation. In general, baroclinic waves propagate northeastward from the mid-latitudes into a region of negative zonal stretching deformation that occurs in three distinct subtropical locations in the Southern Hemisphere. In these regions, the westerly jet decelerates, meridional winds are divergent in the upper troposphere, and total stretching deformation is also negative. These features are collocated with the deepest convection in the subtropics and are always located near a maximum zonal SST gradient and west of a surface high pressure circulation associated with cooler surface conditions to the east.

Many global climate models do not simulate a diagonally oriented cloud band in the South Pacific at all (Lin 2007), but here we considered two GCMs that demonstrate an ability to simulate a convergence zone with similar features to the SPCZ. Both the fully coupled GFDL ocean-land-atmosphere model (Delworth et al. 2006) and the uncoupled atmospheric model provided by the ICTP (Molteni 2003) simulate the Pacific basic state circulation well, but with some notable biases. Biases of most concern to the present study are tendencies in both models to simulate a Pacific cloud band that is too zonal and also weaker than observed. Similar horizontal cloud band biases are noted elsewhere in the Southern Hemisphere for ICTP model, especially in the Indian basin where no diagonally oriented convection is simulated. Perhaps the inability to simulate the SICZ is related to coarse model resolution of the East African Highlands or other orographic features, such as surface heating, which may be important forcing mechanisms. Land features also force the SACZ, yet in the Atlantic a diagonal cloud band extending poleward from Amazonian convection is clearly simulated by the ICTP model, but convection over the ocean is weaker than observed. Questions clearly remain about the relative importance of land, ocean, and convective heating processes in forcing the long wave circulations associated with the Southern Hemisphere convergence zones. Despite these uncertainties, the ICTP model does simulate convection extending poleward in bands mostly collocated with decelerating 200 hPa westerly winds. In all experiments, the lowest OLR in the subtropics almost always

occurs where zonal stretching deformation is negative.

Specifically, it is apparent from the observational and modeling climatologies that there are certain regions of the atmosphere where synoptic disturbances develop and other regions where they tend to decelerate in their eastward propagation. In these other regions, convergence of horizontal group velocity promotes a region of increased wave energy density in accord with simple theoretical rules. These regions are referred to as "graveyards" of synoptic events by Trenberth (1976) who noted that the SPCZ in particular was a place where synoptic disturbances tended to agglomerate and also that, to the east of the SPCZ, the synoptic waves tend to be weaker. The $\partial\overline{U}\big/\partial x = 0$ contour demarks the boundary of Trenberth's graveyard, while regions where $\partial\overline{U}\big/\partial x < 0$ denote the graveyard itself. An equivalent analogy is that regions of convergent zonal flow in the upper-troposphere act as a filter (Farrell and Watterson 1985) limiting the eastward propagation of Rossby waves.

Within the construct of the wave energy accumulation hypothesis, we provide evidence of three main ingredients that define the location and orientation of the SPCZ:

(i) Baroclinic instability, associated with regional maxima of the subtropical jet stream, provides a genesis region for mid-latitude disturbances that propagate northeastward from south of Australia towards the central Pacific.

(ii) Longitudinal scale of the synoptic disturbances shrinks in regions of negative zonal stretching deformation while, at the same time, eastward propagation slows, regional wave energy density increases, and vertical circulations amplify. Such regions occur in each of the three ocean basins of the Southern Hemisphere but in particular, west of the South Pacific high.

(iii) And, to the east of the negative zonal stretching deformation regions, synoptic waves accelerate eastward as $\partial\overline{U}\big/\partial x$ becomes positive but in a weakened state.

These three processes provide a framework for understanding where the mid-latitude disturbances originate and why the SPCZ typically exhibits a pronounced eastern boundary of

deep convection.

Additionally, the SPCZ's diagonal orientation is forced by the Pacific zonal SST gradient which governs the location of $\partial\overline{U}\big/\partial x < 0$ and, hence, the accumulation of wave energy over the central South Pacific. Correlations on interannual timescales between the basin-scale zonal SST gradient, zonal stretching deformation, and OLR suggest that the interaction between ENSO and the SPCZ is governed to a large degree by how underlying SST anomalies force changes in the background basic state and, therefore, modify accumulation regions of mid-latitude synoptic disturbances. The location and intensity of negative zonal stretching deformation becomes more conducive for a diagonally oriented SPCZ when the SST gradient increases between the West Pacific warm pool and cooler Southeast Pacific, such as during La Niña events. Results from the AGCM sensitivity experiments support the hypothesis further that the Pacific zonal SST gradient forces convergence of the background zonal flow near the SPCZ; a necessary criterion for sustaining a diagonally oriented convective band.

Conclusions have been developed using satellite observations, reanalysis data, results from numerical experimentation, and kinematic theory. The kinematic behavior of waves in a longitudinally varying basic flow is based on two constructs: (1) the simple theoretical development of Webster and Chang (1997) applied to synoptic-scale Rossby waves and (2) the behavior of **Q** vectors to study wave structure changes as disturbances propagate into regions of negative zonal stretching deformation. In essence, vertical motions are correlated in space and time with convective anomalies. By focusing on the DJF period, we were able to analyze the cloud bands when they are most intense according to climatology.

While the **Q** vector analysis confirmed that vertical motions intensify as wave energy accumulates, we have only considered the wave energy accumulation hypothesis with respect to Rossby wave propagation in the zonal direction. Considering that the diagonal region of the SPCZ is characterized by strong positive vertical shear ($\partial\overline{U}\big/\partial z > 0$) associated with the velocity gradient between the subtropical jet and weaker westerlies in the

lower troposphere, vertical propagation is almost certainly important to quantifying total wave energy accumulation. Webster and Chang (1997) showed that the vertical scale of Rossby waves propagating through $\partial\overline{U}\big/\partial z > 0$ would increase, but further observational analysis is necessary to determine how vertical shear influences wave energy accumulation in the SPCZ.

Although the composites of synoptic disturbances showed wave trains extending zonally and meridionally in each basin (Figures 5.23, 6.15, and 6.16), we have not examined wave modification in the latitudinal dimension. Using ray tracing to track Rossby wave propagation along a jet, Karoly (1983) found that in regions of meridional shear of the zonal flow ($\partial\overline{U}\big/\partial y$), which is observed in much of the subtropical South Pacific, waves converge towards lower latitudes. Another dominant feature of the zonal flow in the Pacific is the 200 hPa westerly wind duct (Arkin and Webster 1985; Webster and Yang 1989) which also facilitates the refraction of extratropical waves from south of the SPCZ towards the tropics (Matthews and Kiladis 1999). Lacking from this discussion of meridional wave propagation, however, is consideration of how meridional divergence ($\partial\overline{V}\big/\partial y > 0$) impacts wave energy accumulation. Qualitatively at least, the combination of zonal convergence and meridional divergence (i.e., negative total stretching deformation is collocated with the SPCZ as shown in Figure 2.7) further support observations, and kinematic theory (Bluestein 1977), that convection increases where horizontal wave propagation slows and cloud bands become diagonally oriented where extratropical waves are allowed to arc equatorward. Questions certainly remain concerning the quantitative nature of horizontal and vertical wave propagation through the SPCZ and this preliminary discussion merely suggests the topic merits further attention.

The SPCZ, or more specifically the off-equatorial convection enhanced by accumulation of wave energy, seems to force planetary waves also and may influence climate features in other basins. Interestingly, convection in the subtropical Atlantic and Indian basins increased slightly when the Pacific zonal SST gradient was removed and the SPCZ weakened

subsequently. During the same experiment, zonal wind anomalies occurred in all basins and zonal stretching deformation became more negative over parts of the subtropical Atlantic and Indian oceans. Considering the global scale of these anomalies, important teleconnections may originate either from the Pacific zonal SST gradient or directly from convection in the SPCZ. Further understanding of teleconnections between the SPCZ and other basins may improve sub-monthly and long-range forecasts in South America or Africa, especially if the wave energy accumulation hypothesis is applicable to the SACZ or SICZ.

The results of numerical experiments in this study confirm that the Pacific zonal SST gradient forces the SPCZ more directly than topographic features, or even configuration of the continents. An important caveat to the experiment design, however, is that the atmospheric model was forced by a fixed monthly varying SST climatology. No land-ocean interactions were allowed to take place. Some previous studies have shown analytically (Rodwell and Hoskins 2001) and numerically (Takahashi and Battisti 2007a) that land surface boundary conditions, such as the Andes, influence the Pacific SST pattern. Therefore, a reasonable assumption is that replicating our idealized experiments, but with a fully coupled climate model, may show an SPCZ response to land conditions via an indirect pathway through the ocean. On more regional scales, there is a question regarding feedback mechanisms of the SPCZ onto the underlying SST pattern itself. Thus, understanding local air-sea interactions remains a challenge for future research.

There is also merit in further evaluation of why some simple GCMs, such as the ICTP model, simulate the SPCZ well, while other more complex climate models do not. Brown et al. (2010) recently evaluated the seasonal climatology of the SPCZ in 24 coupled model simulations of the 20th century (CMIP3 multi-model dataset: Meehl et al. 2007) and found that the majority of models simulate a distinct region of convection in the South Pacific; however, nearly all the cloud bands tend to be overly zonal. Absence of simulated convection in the subtropics suggests the CMIP3 models do not correctly resolve all processes important in the diagonal region of the SPCZ. A specific research focus should be directed

towards identifying causes of the zonal bias and correcting shared biases among the IPCC suite of 21st century coupled ocean-atmosphere simulations. Some studies (e.g., Wittenberg et al. 2006) suggest that signals propagating from equatorial cold tongue biases, previously identified in many coupled climate simulations including the GFDL model, may alter the Pacific large-scale atmospheric circulation and also the SPCZ. However, the ICTP atmospheric model also simulates a SPCZ that is too horizontal, even though the model is forced by observed SSTs.

Simple modeling and observational studies presented here provide an explanation of basic processes responsible for the SPCZ's diagonal orientation which could help identify biases in more complex climate forecasts. An immediate next step is to quantify, in coupled and uncoupled models, wave kinematics as it relates to interaction of synoptic disturbances with the subtropical region of the SPCZ.

The $\partial\overline{U}/\partial x$–convection relationship presents an interesting new route towards explaining how ENSO influences the South Pacific climate and, perhaps, an avenue for improving long-range prediction. Seasonal forecasting applications, especially concerning tropical cyclone and rainfall characteristics, may benefit from more specific prediction of the SPCZ response to changing background SST associated with different phases, or varieties, of ENSO. The general characteristics presented here of synoptic wave interaction with the long wave circulation, and the subsequent explanation of why the SPCZ is diagonally orientated, may also be applicable locally to forecasting offices in the South Pacific (Power 2010, manuscript submitted to *Eos, Trans. Amer. Geophys. Union*). More accurate prediction of sub-monthly processes is achievable, especially for Pacific island nations in the subtropics where rainfall is frequently associated with frontal interaction with the SPCZ. Finally, the contribution presented in this study relating to why the SPCZ is oriented diagonally away from the equator may facilitate the CLIVAR/ SPICE goal (Ganachaud et al. 2007) to develop a long-term South Pacific monitoring system capable of producing data necessary to improve the initialization and calibration of climate forecasts.

APPENDIX A

DATA SOURCES

A.1 Outgoing Longwave Radiation (OLR)

Daily averaged OLR (W m^{-2}) from the Climate Diagnostics Center (CDC) interpolated dataset (Liebmann and Smith 1996) is used as a proxy of convection in the tropics and subtropics. OLR data is collected by the National Oceanic and Atmospheric Administration (NOAA) polar orbiting satellites and interpolated onto a 2.5° latitude by 2.5° longitude global grid. We examine in detail the 1982-2008 period.

Interpolated OLR data provided by the NOAA/OAR/ESRL PSD, Boulder, Colorado, USA, from their Web site at http://www.esrl.noaa.gov/psd/data/gridded/data.interp_OLR.html

A.2 Global Precipitation Climatology Project (GPCP) Version 2.1 Combined Precipitation

Monthly averaged precipitation (mm day^{-1}) from combined satellite and station data is examined for the 1982-2008 period. The GPCP combined precipitation data were developed by the NASA/Goddard Space Flight Center's Laboratory for Atmospheres as a contribution to the GEWEX Global Precipitation Climatology Project. Version 2.1 (Adler et al. 2003) contains data from polar orbiting and geostationary satellites, as well as rain gauge analyses, interpolated onto a 2.5° latitude by 2.5° longitude global grid.

GPCP data provided by the NOAA/OAR/ESRL PSD, Boulder, Colorado, USA, from their Web site at http://www.esrl.noaa.gov/psd/data/gridded/data.gpcp.html

A.3 National Center for Environmental Prediction/ National Center for Atmospheric Research (NCEP-NCAR) Reanalysis 1

NCEP-NCAR reanalysis data (Kalnay et al. 1996; Kistler et al. 2001) representing zonal and meridional winds ($\overline{U}$ and $\overline{V}$, m s^{-1}), geopotential height (Φ, m), vertical pressure velocity (-ω, Pa s^{-1}), land surface elevation (m), and atmospheric temperature (T, K) are used. Assimilated data are archived on a 2.5° latitude by 2.5° longitude global grid and 17 vertical pressure levels. Daily averaged data are obtained for the 1982-2008 period.

NCEP Reanalysis data provided by the NOAA/OAR/ESRL PSD, Boulder, Colorado, USA, from their Web site at http://www.esrl.noaa.gov/psd/data/gridded/data.ncep.reanalysis.html

A.4 NOAA Optimum Interpolation (OI) Sea Surface Temperature (SST) V2

Monthly averaged SST data (°C: Reynolds et al. 2002) are produced at NOAA using in situ and satellite data interpolated onto a 1° latitude by 1° longitude global grid. Monthly values (obtained for the 1982-2008 period) are derived by a linear interpolation of the weekly OI version 2 fields to daily fields then averaging the daily values over a month.

SST data provided by the NOAA/OAR/ESRL PSD, Boulder, Colorado, USA, from their Web site at http://www.esrl.noaa.gov/psd/data/gridded/data.noaa.oisst.v2.html

A.5 ENSO Indices

ENSO indices are computed using NOAA Extended Reconstructed SST anomalies based on the 1971-2000 period. The Oceanic Niño Index (ONI) is the DJF running mean of SST anomalies in the Niño 3.4 region (5°N-5°S, 120°W-170°W). Niño 3 (5°N-5°S, 150°W-90°W) and Niño 4 (5°N-5°S, 160°E-150°W) indices are the seasonal average of DJF monthly SST anomalies. Figure A.1 shows the position of each index.

ENSO indices provided by the NOAA Climate Prediction Center (CPC) from their Web site at http://www.cpc.noaa.gov/data/indices/

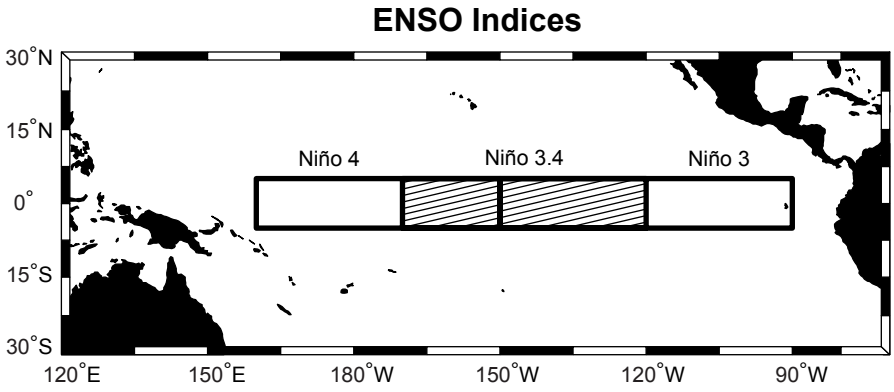

Figure A.1: Map of ENSO indices. Niño 3 and Niño 4 regions- right and left boxes, respectively. Hatching indicates the Niño 3.4 region.

APPENDIX B

THERMAL FORCING MECHANISMS OF ZONAL AND MERIDIONAL CIRCULATIONS

The Pacific Walker and Hadley circulations are depicted typically as zonal and meridional cells, respectively, of rising motions in warm air and subsidence in cooler air. Rising air is forced by surface heating and subsidence occurs gradually as the air mass cools through diabatic emission of longwave radiation ($J/C_p \approx 1$ K day^{-1}, where J is the diabatic heating rate and C_p is the specific heat at constant pressure) according to Holton (2004). A diagnostic relationship for the vertical pressure velocity ($-\omega$) within the troposphere is produced, following Holton, by scaling the Thermodynamic Energy Equation (16) for synoptic-scale motions in the tropics and subtropics where temperature advection is negligible (Equation 17).

$$\left(\frac{\partial}{\partial t} + V \bullet \nabla\right) T + \frac{\omega N^2 H}{R} = \frac{J}{C_p} \tag{16}$$

$$\frac{\omega N^2 H}{R} = \frac{J}{C_p} \tag{17}$$

Here, N is the buoyancy frequency, H is the scale height, R is the gas constant for dry air, and J and C_p are as defined above. Diabatic cooling of the troposphere through emission of longwave radiation must therefore be balanced by adiabatic warming due to slow subsidence. Horizontal winds near the surface and aloft bridge the rising and subsiding branches, completing the circulation cells. Locations of these thermally direct circulations, especially Hadley cells, oscillate seasonally as the rising branches are collocated with the warmest surface temperatures, usually just poleward of the equator in the summer hemisphere (Hartmann 1994).

Large regions of the tropical and subtropical Pacific are characterized by storminess,

adding complexity to the overturning circulation model discussed above. In addition to forcing from the warm surface boundary, much of the troposphere is also heated by moist convection. Tall cumulous clouds release latent heat into the atmosphere by the condensation process and the average heating rate per unit mass of air increases by about five times ($J/C_p \approx 5$ K day^{-1}) (Holton 2004). Equation 17 suggests that cumulous convection (i.e., low OLR values) would force columns of vigorous ascent, surrounded by larger regions of slowly subsiding motions. The location of deep convection has a strong impact on the forcing of the rising and subsiding branches of the Walker and Hadley circulations.

APPENDIX C

GENERAL CIRCULATION MODELS

C.1 NOAA's Geophysical Fluid Dynamics Laboratory (GFDL) Coupled General Circulation Model (CM2.1)

Data from the 20th century GFDL CM2.1 experiment (Delworth et al. 2006) are analyzed to determine how the SPCZ is simulated by a coupled atmosphere-land-ocean general circulation model (CGCM). Resolution of the land and atmospheric models are both 2° latitude x 2.5° longitude; with the atmospheric component having 24 vertical levels. The ocean resolution is 1° in latitude and longitude, with finer meridional resolution equatorward of 30° (1/3° at the equator), and 50 vertical levels (22 evenly distributed levels in the top 220 m). The 20th century experiment consists of 5 runs, each extending from 1861-2000. Climate change integrations of the GFDL model were previously compared with this control simulation (Solomon et al. 2007) to support the Fourth Assessment Report of the Intergovernmental Panel on Climate Change (IPCC).

The model integration period and temporal resolution allow study of climate features on a variety of timescales ranging from synoptic to interannual variability, including anthropogenic climate change. Here, we utilize data from the later period (1982-2000) of the 20th century experiment to examine the South Pacific climate in approximately steady-state conditions. Our analysis focuses mainly on run two because 10 years of daily average output is available (1991-2000), of which 9 seasonal time series are used, in addition to monthly average data for the entire period.

Model output is available for download at http://nomads.gfdl.noaa.gov

C.2 International Centre for Theoretical Physics (ICTP) Atmospheric General Circulation Model (AGCM)

A series of controlled numerical experiments are conducted using the ICTP AGCM (Molteni 2003; Bracco et al. 2004; Kucharski et al. 2006; Kucharski et al. 2009). Kucharski et al. (2009) describe the AGCM as based on a hydrostatic spectral dynamical core (Held and Suarez 1994) and governed by many parameterized processes including short- and long-wave radiation, large-scale condensation, convection, surface fluxes of momentum, heat and moisture, and vertical diffusion. Convection is parameterized by a mass-flux scheme that is activated where conditional instability is present. The idealized AGCM is configured with eight vertical (sigma) levels and with a triangular spectral truncation at total wavenumber 30 (approximately 3.75° horizontal resolution).

In all experiments, the model is initialized from an atmosphere at rest and integrated for a 26 year period. The first two years of integration are discarded and the 24 remaining years used to compile DJF seasonal averages.

The ICTP AGCM is available for download at http://users.ictp.it/ kucharsk/speedy-net.html

Bibliography

AchutaRao, K. and K. Sperber, 2002: Simulation of the El Niño Southern Oscillation: Results from the Coupled Model Intercomparison Project. *Climate Dyn.*, **19**, 191–209.

Adler, R., G. Huffman, A. Chang, and Coauthors, 2003: The Version 2.1 Global Precipitation Climatology Project (GPCP) Monly Precipitation Analysis (1979-Present). *J. Hydrometeor.*, **4**, 1147–1167.

Arkin, P. and P. Webster, 1985: Annual and interannual variability of tropical-extratropical interaction: An empirical study. *Mon. Wea. Rev.*, **113**, 1510–1523.

Ashok, K., S. Behera, S. Rao, H. Weng, and T. Yamagata, 2007: El Niño Modoki and its possible teleconnection. *J. Geophys. Res.*, **112**, doi:10.1029/2006JC003798.

Barreiro, M., P. Chang, and R. Saravanan, 2002: Variability of the South Atlantic Convergence Zone simulated by an atmospheric general circulation model. *J. Climate*, **15**, 745–763.

Bjerknes, J., L. Allison, E. Kreins, and Coauthors, 1969: Satellite mapping of Pacific tropical cloudiness. *Bull. Amer. Meteor. Soc.*, **50**, 313–322.

Bluestein, H., 1977: Synoptic-scale deformation and tropical cloud bands. *J. Atmos. Sci.*, **34**, 891–900.

Booth, A. and V. Taylor, 1969: Meso-scale archive and computer products of digitized video data from ESSA satellites. *Bull. Amer. Meteor. Soc.*, **50**, 431–438.

Bracco, A., F. Kucharski, R. Kallummal, and F. Molteni, 2004: Internal variability, external forcing and climate trends in multi-decadal AGCM ensembles. *Climate Dyn.*, **23**, 659–678.

Bretherton, F. and C. Garrett, 1968: Wavetrains in inhomogeneous moving media. *Proc. Roy. Soc. Lond.*, 529–554.

Brown, J., S. Power, F. Delage, R. Colman, A. Moise, and B. Murphy, 2010: Evaluation of the South Pacific Convergence Zone in WCRP CMIP3 climate model simulations of the 20^{th} century. *J. Climate*, in press.

Carvalho, L., C. Jones, and B. Liebmann, 2002: Extreme precipitation events in southeastern South America and large-scale convective patterns in the South Atlantic Convergence Zone. *J. Climate*, **15**, 2377–2394.

Carvalho, L., C. Jones, and B. Liebmann, 2004: The South Atlantic Convergence Zone: Intensity, form, persistence, and relationships with intraseasonal to interannual activity and extreme rainfall. *J. Climate*, **17**, 88–108.

Chang, H. and P. Webster, 1990: Energy accumulation and emanation at low latitudes. Part II: Nonlinear response to strong episodic forcing. *J. Atmos. Sci.*, **47**, 2624–2644.

Chang, H. and P. Webster, 1995: Energy accumulation and emanation at low latitudes. Part III: Forward and backward accumulation. *J. Atmos. Sci.*, **52**, 2384–2403.

Chou, C. and J. Neelin, 2001: Mechanisms limiting the southward extent of the South American summer monsoon. *Geophys. Res. Lett.*, **28**, 2433–2436.

Cook, K., 2000: The South Indian Convergence Zone and interannual rainfall variability over southern Africa. *J. Climate*, **13**, 3789–3804.

Cook, K., 2001: A Southern Hemisphere wave response to ENSO with implications for southern Africa precipitation. *J. Atmos. Sci.*, **58**, 2146–2162.

Cook, K., 2009: South American climate variability and change: Remote and regional forcing processes. *Past Climate Variability in South America and Surrounding Regions*, F. Vimeux, R. Sylvestre, and M. Khodri, Eds., Springer, Vol. 14, chap. 8, 193–212.

Cunningham, C. and I. Cavalcanti, 2006: Intraseasonal modes of variability affecting the South Atlantic Convergence Zone. *Int. J. Climatol.*, **26**, 1165–1180.

Davey, M., M. Huddleston, K. Sperber, and Coauthors, 2002: STOIC: A study of coupled model climatology and variability in tropical ocean regions. *Climate Dyn.*, **18**, 403–420.

De Almeida, R., P. Nobre, R. Haarsma, and E. Campos, 2007: Negative ocean–atmosphere feedback in the South Atlantic Convergence Zone. *Geophys. Res. Lett.*, **34**, doi: 10.1029/2007GL030401.

Delworth, T., A. Broccoli, A. Rosati, and Coauthors, 2006: GFDL's CM2 global climate models- Part 1: Formulation and simulation characteristics. *J. Climate*, **19**, 643–674.

Duane, G., P. Webster, and J. Weiss, 1999: Co-occurrence of Northern and Southern Hemisphere blocks as partially synchronized chaos. *J. Atmos. Sci.*, **56**, 4183–4205.

Duchon, C., 1979: Lanczos filtering in one and two dimensions. *J. Appl. Meteor.*, **18**, 1016–1022.

Eastin, M. and D. Vincent, 1998: A 6-yr climatology of vertical mean and shear components of kinetic energy for the Australian-South Pacific jet stream. *J. Climate*, **11**, 283–291.

Farrell, B. and I. Watterson, 1985: Rossby waves in opposing currents. *J. Atmos. Sci.*, **42**, 1746–1756.

Fernandes, K., 2009: The Amazon hydrometeorology: Climatology, variability and links to changes in weather patterns. Ph.D. thesis, Georgia Institute of Technology, 91 pp.

Figueroa, S., P. Satyamurty, and P. Silva Dias, 1995: Simulations of the summer circulation over the South American region with an Eta coordinate model. *J. Atmos. Sci.*, **52**, 1573–1584.

Fitz-Roy, R., 1839: Narrative of the surveying voyages of His Majesty's Ships Adventure and Beagle between the years 1826 and 1836, describing their examination of the southern shores of South America, and the Beagle's circumnavigation of the globe. *Proceedings of the second expedition, 1831-36, under the command of Captain Robert Fitz-Roy, R.N.*, H. Colburn, Ed., London.

Folland, C., J. Renwick, and M. Salinger, 2002: Relative influences of the Interdecadal Pacific Oscillation and ENSO on the South Pacific Convergence Zone. *Geophys. Res. Lett.*, **29**, doi:10.1029/2001GL014201.

Fraedrich, K. and H. Böttger, 1978: A wavenumber-frequency analysis of the 500 mb geopotential at 50°N. *J. Atmos. Sci.*, **35**, 745–750.

Ganachaud, A., W. Kessler, S. Wijffels, and Coauthors, 2007: Southwest Pacific Ocean Circulation and Climate Experiment (SPICE)-Part I. Scientific background. Tech. rep., International CLIVAR Project Office, CLIVAR Publication Series No. 111, NOAA OAR Special Report, NOAA/OAR/PMEL, 37 pp., Seattle, WA.

Garreaud, R., 2000: Cold air incursions over subtropical South America: Mean structure and dynamics. *Mon. Wea. Rev.*, **128**, 2544–2558.

Gibson, J., P. Kallberg, S. Uppala, and Coauthors, 1997: ECMWF re-analysis. Project report series. 1. ERA description. Tech. rep., European Centre for Medium-Range Weather Forecasts, Reading (U.K.).

Gill, A., 1980: Some simple solutions for heat-induced tropical circulation. *Quart. J. Roy. Meteor. Soc.*, **106**, 447–462.

Godshall, F., 1968: Intertropical Convergence Zone and mean cloud amount in tropical Pacific Ocean. *Mon. Wea. Rev.*, **96**, 172–175.

Graham, N. and T. Barnett, 1987: Sea surface temperature, surface wind divergence, and convection over tropical oceans. *Science*, **238**, 657–659.

Grimm, A. and T. Ambrizzi, 2009: Teleconnections into South America from the tropics and extratropics on interannual and intraseasonal timescales. *Past Climate Variability in South America and Surrounding Regions*, F. Vimeux, R. Sylvestre, and M. Khodri, Eds., Springer, Vol. 14, chap. 7, 159–191.

Hartmann, D., 1994: *Global Physical Climatology*. Elsevier Academic Press, 411 pp.

Held, I. and M. Suarez, 1994: A proposal for the intercomparison of the dynamical cores of atmospheric general circulation models. *Bull. Amer. Meteor. Soc.*, **75**, 1825–1830.

Holton, J., 2004: *An introduction to dynamic meteorology*. 4th ed., Elsevier Academic Press, 535 pp.

Hoskins, B., I. Draghici, and H. Davies, 1978: A new look at the ω-equation. *Quart. J. Roy. Meteor. Soc.*, **104**, 31–38.

Hoskins, B. and K. Hodges, 2005: A new perspective on Southern Hemisphere storm tracks. *J. Climate*, **18**, 4108–4129.

Hubert, L., 1961: A subtropical convergence line of the South Pacific: A case study using meteorological satellite data. *J. Geophys. Res.*, **66**, 797–812.

Juillet-Leclerc, A., S. Thiria, P. Naveau, and Coauthors, 2006: SPCZ migration and ENSO events during the 20$^{\text{th}}$ century as revealed by climate proxies and a Fiji coral. *Geophys. Res. Lett.*, **33**, doi:10.1029/2006GL025950.

Julian, P. and R. Chervin, 1978: A study of the Southern Oscillation and the Walker Circulation. *Mon. Wea. Rev.*, **106**, 1433–1451.

Kalnay, E., M. Kanamitsu, R. Kistler, and Coauthors, 1996: The NCEP/NCAR 40-year reanalysis project. *Bull. Amer. Meteor. Soc.*, **77**, 437–470.

Kao, H. and J. Yu, 2009: Contrasting eastern-Pacific and central-Pacific types of ENSO. *J. Climate*, **22**, 615–632.

Karoly, D., 1983: Rossby wave propagation in a barotropic atmosphere. *Dyn. Atmos. Oceans*, **7**, 111–125.

Kiladis, G., H. Storch, and H. Loon, 1989: Origin of the South-Pacific Convergence Zone. *J. Climate*, **2**, 1185–1195.

Kim, H., P. Webster, and J. Curry, 2009: Impact of shifting patterns of Pacific Ocean warming on North Atlantic tropical cyclones. *Science*, **325**, doi:10.1126/science.1174062.

Kistler, R., E. Kalnay, W. Collins, and Coauthors, 2001: The NCEP-NCAR 50-year reanalysis: Monthly means CD-ROM and documentation. *Bull. Amer. Meteor. Soc.*, **82**, 247–267.

Kodama, Y., 1992: Large-scale common features of subtropical precipitation zones (the Baiu frontal zone, the SPCZ, and the SACZ) Part I: Characteristics of subtropical frontal zones. *J. Meteor. Soc. Japan*, **70**, 813–835.

Kodama, Y., 1993: Large-scale common features of subtropical convergence zones (the Baiu frontal zone, the SPCZ, and the SACZ) Part II: Conditions of the circulations for generating the STCZs. *J. Meteor. Soc. Japan*, **71**, 581–610.

Kodama, Y., 1999: Roles of the atmospheric heat sources in maintaining the subtropical convergence zones: An aqua-planet GCM study. *J. Atm. Sci.*, **56**, 4032–4049.

Kornfield, J., A. Hasler, K. Hanson, and Coauthors, 1967: Photographic cloud climatology from ESSA 3 and 5 computer produced mosaics. *Bull. Amer. Meteor. Soc.*, **48**, 878–883.

Kucharski, F., F. Molteni, and A. Bracco, 2006: Decadal interactions between the western tropical Pacific and the North Atlantic Oscillation. *Climate Dyn.*, **26**, 79–91.

Kucharski, F., A. Bracco, J. Yoo, and Coauthors, 2009: A Gill-Matsuno-type mechanism explains the tropical Atlantic influence on African and Indian monsoon rainfall. *Quart. J. Roy. Meteor. Soc.*, **135**, 569–579.

Kug, J., F. Jin, and S. An, 2009: Two types of El Niño events: Cold tongue El Niño and warm pool El Niño. *J. Climate*, **22**, 1499–1515.

Kuhnel, I., 1989: Tropical-extratropical cloudband climatology based on satellite data. *Int. J. Climatol.*, **9**, 441–463.

Larkin, N. and D. Harrison, 2005: Global seasonal temperature and precipitation anomalies during El Niño autumn and winter. *Geophys. Res. Lett.*, **32**, doi:10.1029/2005GL022860.

Latif, M., K. Sperber, J. Arblaster, and Coauthors, 2001: ENSIP: the El Niño simulation intercomparison project. *Climate Dyn.*, **18**, 255–276.

Leese, J., C. Novak, and V. Taylor, 1970: The determination of cloud pattern motions from geosynchronous satellite image data. Tech. rep., National Environmental Satellite Center, Washington, D.C.

Lenters, J. and K. Cook, 1997: On the origin of the Bolivian high and related circulation features of the South American climate. *J. Atmos. Sci.*, **54**, 656–677.

Lenters, J. and K. Cook, 1999: Summertime precipitation variability over South America: Role of the large-scale circulation. *Mon. Wea. Rev.*, **127**, 409–431.

Liebmann, B., G. Kiladis, J. Marengo, T. Ambrizzi, and J. Glick, 1999: Submonthly convective variability over South America and the South Atlantic Convergence Zone. *J. Climate*, **12**, 1877–1891.

Liebmann, B. and C. Smith, 1996: Description of a complete (interpolated) outgoing longwave radiation dataset. *Bull. Amer. Meteor. Soc.*, **77**, 1275–1277.

Lighthill, J., 1978: *Waves in Fluids*. Cambridge University Press, doi: 10.2277/0521010454.

Lin, J., 2007: The double-ITCZ problem in IPCC AR4 coupled GCMs: Ocean-atmosphere feedback analysis. *J. Climate*, **20**, 4497–4525.

Lindzen, R. and S. Nigam, 1987: On the role of sea-surface temperature-gradients in forcing low level winds and convergence in the tropics. *J. Atmos. Sci.*, **44**, 2418–2436.

Lintner, B. and J. Neelin, 2008: Eastern margin variability of the South Pacific Convergence Zone. *Geophys. Res. Lett.*, **35 (L16701)**, doi:10.1029/2008GL034298.

Matsuno, T., 1966: Quasi-geostrophic motions in the equatorial area. *J. Meteor. Soc. Japan*, **44**, 25–43.

Matthews, A., B. Hoskins, J. Slingo, and M. Blackburn, 1996: Development of convection along the SPCZ within a Madden-Julian oscillation. *Quart. J. Roy. Meteor. Soc.*, **122**, 669–688.

Matthews, A. and G. Kiladis, 1999: Tropical-extratropical interaction between high-frequency transients and the Madden-Julian oscillation. *Mon. Wea. Rev.*, **127**, 661–677.

Meehl, G., C. Covey, T. Delworth, M. Latif, B. McAvaney, J. Mitchell, R. Stouffer, and K. Taylor, 2007: The WCRP CMIP3 multi-model dataset: A new era in climate change research. *Bull. Amer. Meteor. Soc.*, **88**, 1383–1394.

Molteni, F., 2003: Atmospheric simulations using a GCM with simplified physical parametrizations. I. model climatology and variability in multi-decadal experiments. *Climate Dyn.*, **20**, 175–191.

Nicholson, S., 2003: Comment on "The South Indian Convergence Zone and interannual rainfall variability over Southern Africa" and the question of ENSO's influence on southern Africa. *J. Climate*, **16**, 555–562.

Nieto-Ferreira, R., T. Rickenbach, and E. Wright, 2010: The role of cold fronts in the onset of the South American monsoon. *Quart. J. Roy. Meteor. Soc.*, submitted.

Ninomiya, K., 2007: Similarity and difference between the South Atlantic Convergence Zone and the Baiu frontal zone simulated by an AGCM. *J. Meteor. Soc. Japan*, **85**, 277–299.

Ninomiya, K., 2008: Similarities and differences among the South Indian Ocean Convergence Zone, North American Convergence Zone, and other subtropical convergence zones simulated using an AGCM. *J. Meteor. Soc. Japan*, **86**, 141–165.

Power, S., 2010: Report on the International Scientific Research Workshop on the South Pacific Convergence Zone. *Eos, Trans. Amer. Geophys. Union*, submitted.

Renwick, J. and M. Revell, 1999: Blocking over the South Pacific and Rossby wave propagation. *Mon. Wea. Rev.*, **127**, 2233–2247.

Reynolds, R., N. Rayner, T. Smith, and Coauthors, 2002: An improved in situ and satellite SST analysis for climate. *J. Climate*, **15**, 1609–1625.

Rickenbach, T., R. Nieto-Ferreira, J. Halverson, and Coauthors, 2002: Modulation of convection in the southwestern Amazon basin by extratropical stationary fronts. *J. Geophys. Res.*, doi:10.1029/2000JD000263.

Robertson, A. and C. Mechoso, 2000: Interannual and interdecadal variability of the South Atlantic Convergence Zone. *Mon. Wea. Rev.*, **128**, 2947–2957.

Rodwell, M. and B. Hoskins, 2001: Subtropical anticyclones and summer monsoons. *J. Climate*, **14**, 3192–3211.

Rowell, D., 2001: Teleconnections between the tropical Pacific and the Sahel. *Quart. J. Roy. Meteor. Soc.*, **127**, 1683–1706.

Serra, Y., G. Kiladis, and M. Cronin, 2008: Horizontal and vertical structure of easterly waves in the Pacific ITCZ. *J. Atmos. Sci.*, **65**, 1266–1284.

Solomon, S., D. Qin, M. Manning, and Coeditors, 2007: *Climate Change 2007- The Physical Science Basis*. Cambridge University Press, 996 pp.

Streten, N., 1970: A note on the climatology of the satellite observed zone of high cloudiness in the central South Pacific. *Aust. Meteor. Mag.*, **18**, 31–38.

Streten, N., 1973: Some characteristics of satellite-observed bands of persistent cloudiness over the Southern Hemisphere. *Mon. Wea. Rev.*, **101**, 486–495.

Streten, N. and J. Zillman, 1984: Climate of the South Pacific Ocean. *World Survey of Climatology*, H. van Loon, Ed., Elsevier, The Oceans.

Takahashi, K. and D. Battisti, 2007a: Processes controlling the mean tropical Pacific precipitation pattern. Part I: The Andes and the Eastern Pacific ITCZ. *J. Climate*, **17**, 3434–3451.

Takahashi, K. and D. Battisti, 2007b: Processes controlling the mean tropical Pacific precipitation pattern. Part II: The SPCZ and the Southeast Pacific Dry Zone. *J. Climate*, **20**, 5696–5706.

Taljaard, J., 1972: Synoptic meteorology of the Southern Hemisphere. *Meteorology of the Southern Hemisphere. Meteor. Monogr.*, C. Newton, Ed., Amer. Meteor. Soc., 139–211.

Todd, M. and R. Washington, 1998: Extreme daily rainfall in southern African and Southwest Indian Ocean tropical-temperate links. *S. Afr. J. Sci.*, **94**, 64–70.

Todd, M. and R. Washington, 1999: Tropical-temperate links in southern Africa and Southwest Indian Ocean satellite-derived rainfall. *Int. J. Climatol.*, **19**, 1601–1616.

Todd, M., R. Washington, and T. James, 2003: Characteristics of summertime daily rainfall variability over South America and the South Atlantic Convergence Zone. *Meteor. Atmos. Phys.*, **83**, 89–108.

Toma, V. and P. Webster, 2009: Oscillations of the intertropical convergence zone and the genesis of easterly waves. Part I: diagnostics and theory. *Climate Dyn.*, doi: 10.1007/s00382-009-0584.

Tomas, R. and P. Webster, 1994: Horizontal and vertical structure of cross-equatorial wave propagation. *J. Atmos. Sci.*, **51**, 1417–1429.

Torrence, C. and G. Compo, 1998: A practical guide to wavelet analysis. *Bull. Amer. Meteor. Soc.*, **79**, 61–78.

Trenberth, K., 1976: Spatial and temporal variations of the Southern Oscillation. *Quart. J. Roy. Meteor. Soc.*, **102**, 639–653.

Trenberth, K., 1991: Storm tracks in the Southern Hemisphere. *J. Atmos. Sci.*, **48**, 2159–2178.

Trenberth, K., 1997: The definition of El Niño. *Bull. Amer. Meteor. Soc.*, **78**, 2771–2777.

Trenberth, K. and D. Stepaniak, 2003: Seamless poleward atmospheric energy transports and implications for the Hadley circulation. *J. Climate*, **16**, 3706–3722.

Trenberth, K., D. Stepaniak, and J. Caron, 2000: The global monsoon as seen through the divergent atmospheric circulation. *J. Climate*, **13**, 3939–3993.

van Heerden, J. and J. Taljaard, 1999: Africa and the surrounding waters. *Meteorology of the Southern Hemisphere. Meteor. Monogr.*, D. Karoly and D. Vincent, Eds., Amer. Meteor. Soc., 141–174.

van Loon, H. and R. Jenne, 1972: The zonal harmonic standing waves in the Southern Hemisphere. *J. Geophys. Res.*, **77**, 992–1003.

Vincent, D., 1994: The South Pacific convergence zone (SPCZ): A review. *Mon. Wea. Rev.*, **122**, 1949–1970.

Vincent, D., 1999: Pacific ocean. *Meteorology of the Southern Hemisphere. Meteor. Monogr.*, D. Karoly and D. Vincent, Eds., Amer. Meteor. Soc., 101–117.

Vincent, E., M. Lengaigne, C. Menkes, and Coauthors, 2009: Interannual variability of the South Pacific Convergence Zone and implications for tropical cyclone genesis. *Climate Dyn.*, doi:10.1007/s0038200907163.

Webster, P., 1972: Response of the tropical atmosphere to local, steady forcing. *Mon. Wea. Rev.*, **100**, 518–541.

Webster, P., 1982: Seasonality in the local and remote atmospheric response to sea surface temperature anomalies. *J. Atmos. Sci.*, **39**, 29–40.

Webster, P. and J. Holton, 1982: Cross-equatorial response to middle-latitude forcing in a zonally varying basic state. *J. Atmos. Sci.*, **39**, 722–733.

Webster, P. and H. Chang, 1988: Equatorial energy accumulation and emanation regions: Impacts of a zonally varying basic state. *J. Atmos. Sci.*, **45**, 803–829.

Webster, P. and S. Yang, 1989: The three-dimensional structure of perturbation kinetic energy and its relationship to the zonal wind field. *J. Climate*, **2**, 1210–1222.

Webster, P. and H. Chang, 1997: Atmospheric wave propagation in heterogeneous flow: basic flow controls on tropical-extratropical interaction and equatorial wave modification. *Dyn. Atmos. Oceans*, **27**, 91–134.

Weng, H., K. Ashok, S. Behera, S. Rao, and T. Yamagata, 2007: Impacts of recent El Niño Modoki on dry/wet conditions in the Pacific rim during boreal summer. *Climate Dyn.*, **29**, 113–129.

Wheeler, M. and G. Kiladis, 1999: Convectively coupled equatorial waves: Analysis of clouds and temperature in the wavenumber-frequency domain. *J. Atmos. Sci.*, **56**, 374–399.

Widlansky, M., 2007: Variability of the South Pacific Convergence Zone and its influence on the general atmospheric circulation. M.S. thesis, School of Earth and Atmospheric Sciences, Georgia Institute of Technology, 76 pp.

Widlansky, M., P. Webster, and C. Hoyos, 2010: On the location and orientation of the South Pacific Convergence Zone. *Climate Dyn.*, doi:10.1007/s00382-010-0871-6.

Willson, M., 1975: A wavenumber-frequency analysis of large-scale tropospheric motions in the extratropical Northern Hemisphere. *J. Atmos. Sci.*, **32**, 478–488.

Wittenberg, A., A. Rosati, N. Lau, and Coauthors, 2006: GFDL's CM2 global climate models- Part 3: Tropical Pacific climate and ENSO. *J. Climate*, **19**, 698–722.

Yoshikane, T. and F. Kimura, 2003: Formation mechanism of the simulated SPCZ and Baiu front using a regional climate model. *J. Atmos. Sci.*, **60**, 2612–2632.

Zhang, C. and P. Webster, 1989: Effects of zonal flows on equatorially trapped waves. *J. Atmos. Sci.*, **46**, 3632–3652.